

## SEARCH FOR LIGHT AND HEAVY FLAVOR EXCITED QUARKS

This chapter documents in great detail the various steps and procedures followed in the analysis of CMS data to search for any signature of excited light and heavy quark presence in  $\gamma + \text{jet}$  and  $\gamma + \text{b-jet}$  final states respectively.

### 4.1 Analysis strategy

In high energy physics, the invariant mass is a very important parameter to determine the nature of a process. It is a Lorentz invariant quantity and is defined as the system mass constructed using the Lorentz invariant energy and momentum. For a single particle, the invariant mass is equivalent to its rest mass, given by  $m^2 = E^2 - p^2$ , in natural units<sup>1</sup>. This relation is also true for a system of masses with  $E$  and  $p$  representing the total energy and momentum of the system. In a process that occurs through a resonance, the invariant mass of final state particles is equivalent to the rest mass of the resonance. The process has a larger cross-section corresponding to the energy of resonance mass.

If we plot the invariant mass distribution of final state particles for a large sample of events, the number of events corresponding to the resonance mass will be relatively larger as compared to the neighbouring masses. The resonance will

---

<sup>1</sup>In natural units,  $\hbar = c = 1$

appear as a peak over the continuous distribution, arising due to the standard model processes referred to as the background processes, with the peak-width proportional to the resonance's life time. The background due to various SM processes is subtracted either by the use of Monte Carlo simulated background samples or by the use of data driven technique where the background is evaluated by fitting the invariant mass distribution with a smooth parameterization. Any significant deviation from the smooth distribution at any point in data is considered as a signal of new physics. In case of absence of any significant deviation, the resonance signal model, simulated on the basis of the underlying theory, is used to evaluate a signal cross-section (mass), above (below) which the presence of the signal is discarded with some statistical significance.

### 4.1.1 Excited quark analysis

In this analysis, the resonance signals considered are the excited states of light  $q = u, d$  and heavy  $b$  quarks. The underlying processes are  $pp \rightarrow q^* \rightarrow \gamma + \text{jet}$  and  $pp \rightarrow b^* \rightarrow \gamma + b\text{-jet}$ . The invariant mass distribution spectra of  $\gamma + \text{jet}$  and  $\gamma + b\text{-jet}$  are the most important distributions for this study, which have been analyzed to investigate the presence or absence of excited quark signals. A detailed overview of the signals and backgrounds of this study is presented in sections below.

#### 4.1.1.1 Signals

This analysis considers the  $q^*$  and  $b^*$  signals decaying into  $\gamma + \text{jet}$  and  $\gamma + b\text{-jet}$  final states respectively, where the jet can be a light quark, a gluon or a  $b$ -quark. The Feynman diagrams representing the various physics processes contributing to this channel are presented in Fig. 1.4. Among these, the most dominant quark-gluon fusion process has been considered for this analysis. This process contributes through two Feynman diagrams in s- and t-channel as shown in Fig. 4.1.

The resonance will show its presence in the form of a bump in the s-channel and in the form of an excess of events in t-channel, over the continuum invariant mass distribution of  $\gamma + \text{jet}$ .

#### 4.1.1.2 Backgrounds

In pp collisions, the  $\gamma + \text{jet}$  channel has a rather clean and simple signature within the detector. Still, many known SM processes can mimic this final state

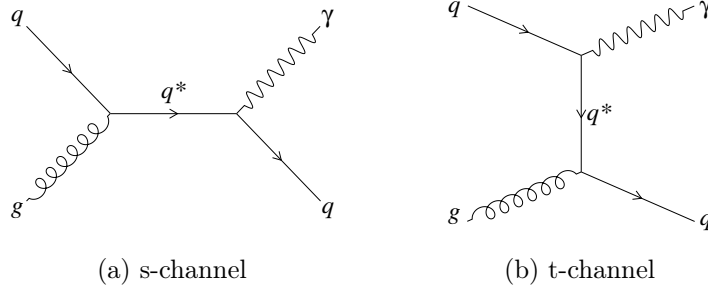


Figure 4.1: Feynman diagrams for quark-gluon fusion process in s and t channel.

and form the backgrounds of this study. These potential physics backgrounds are reported below as per their dominance:

#### 4.1.1.2.1 SM $\gamma$ + jet

The SM  $\gamma$  + jet processes where a photon and a jet are produced in the hard collision, form the most dominant and irreducible background for this study. A number of processes including quark-gluon compton scattering ( $qg \rightarrow q\gamma$ ), quark-antiquark annihilation ( $q\bar{q} \rightarrow g\gamma$ ) and gluon-gluon fusion ( $gg \rightarrow g\gamma$ ) contribute to this background. The Feynman diagrams representing these processes are shown in Fig. 4.2. The  $qg$  scattering process dominates the total SM  $\gamma$  + jet cross-section over the entire  $p_T$  range. The contribution from the  $q\bar{q}$  annihilation process is lesser, though it increases with increasing  $p_T$ . The  $gg$  fusion process, being a NLO process, contributes negligibly.

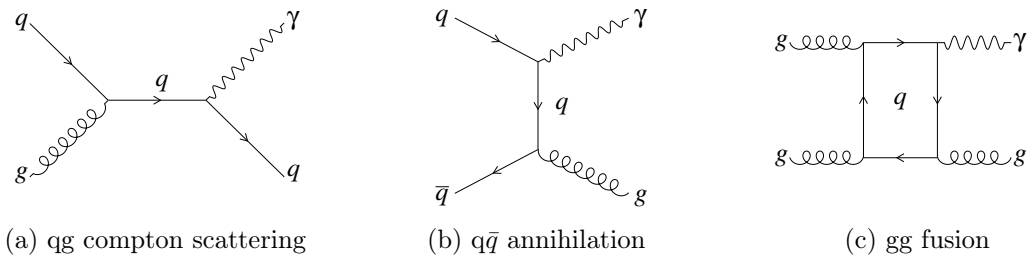


Figure 4.2: Standard model background contribution from  $\gamma$  + jet processes.

#### 4.1.1.2.2 QCD dijet

The SM dijet processes where two jets are produced in the hard scattering, can form a background to a  $\gamma$  + jet process if one of the jets fragments into a highly energetic  $\pi^0$  which then decays into a pair of overlapping photons and gets reconstructed as a single photon in the detector. A number of processes like the

ones shown in Fig. 4.3, contribute to this background. The production cross-section of these processes is around  $10^4$  times larger than the SM  $\gamma + \text{jet}$  processes. But, since the probability of a jet faking a photon is about  $10^{-4} - 10^{-3}$ , this background form the second largest background of this study. Also, the cross-section for these processes falls very swiftly ( $\sim p_T^{-4}$ ) with increasing  $p_T$ , so this background has significantly lower contribution at high  $p_T$ .

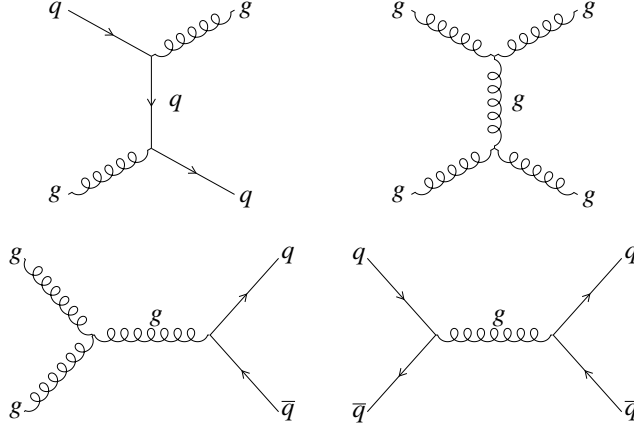


Figure 4.3: Standard model background contribution from QCD dijet processes.

This background is also supplemented by the bremsstrahlung process where a photon is radiated by one of the initial or final state quarks as shown in Fig. 4.4. This results into one photon and two jets in the final state and can mimic a  $\gamma + \text{jet}$  process if one of the jets is lost or mismeasured. However, since these photons do not emerge from primary interaction vertex and have hadronic activity in close vicinity, these can be easily removed by the photon isolation requirements.

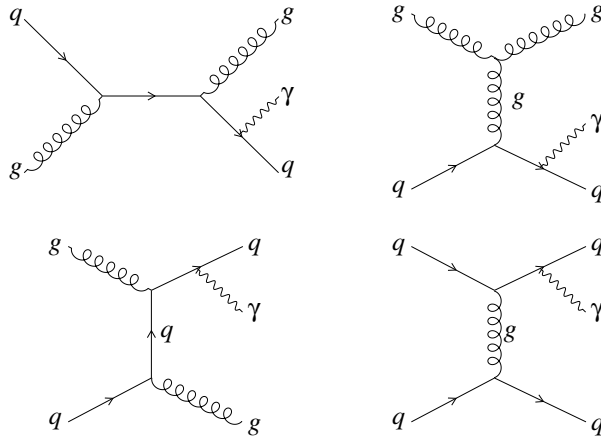


Figure 4.4: Bremsstrahlung contribution to SM QCD dijet production.

#### 4.1.1.2.3 EWK

The SM electroweak processes, like  $W/Z + \text{jet}$  production, can contribute a small fraction to the total background when the heavy electroweak boson decays leptonically and one of the leptons is either lost or goes away in the form of missing transverse energy. The Feynman diagrams corresponding to these processes are shown in Fig. 4.5

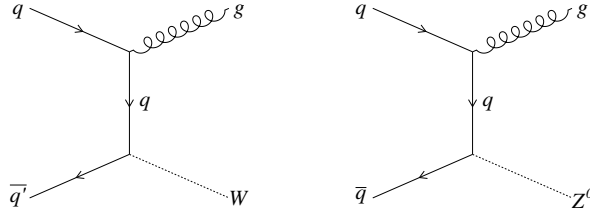


Figure 4.5: Background contributions from electroweak processes.

## 4.2 Production of Ntuples

The analysis chain starts with the production of Ntuples<sup>2</sup> of required data and MC samples. This step makes use of an analyzer, a code written mostly in C++ and python within the CMSSW environment, that extracts the information, related to different physics objects, triggers, vertices, pile-up etc., from the reconstructed or simulated datasets and store them in ROOT files in the form of Ntuples. Since the analyzer has to run over billions of events contained within a dataset, this step is almost impossible to perform using interactive computing. A technique known as grid computing [128], that considers a number of computer resources located at multiple places all over the world, is used along with CMS Remote Analysis Builder (CRAB)<sup>3</sup> [173] to achieve this task. The Ntuples consist of organized information of all the quantities required for further analysis. This study has used the Tier-3 center present at Fermilab, USA, referred to as T3\_US\_FNALLPC, for the production, storage, and analysis of data and MC Ntuples.

### 4.2.1 Samples processed

The recorded detector data and simulated MC samples used in this analysis are detailed below. The MC samples include the signal as well as the background

<sup>2</sup>Analysis specific event information extracted from the complete dataset and stored in ROOT files in the form of tree/branch structure.

<sup>3</sup>An official CMS tool that allows an end user to access the data distributed at various sites as well as automates the task of job submission.

samples. All the samples are used in mini-AOD format and have been processed using a CMSSW version 8\_0\_26\_patch1.

#### 4.2.1.1 Data

This analysis used the pp collision data collected by the CMS detector at  $\sqrt{s} = 13$  TeV in 2016, with a bunch crossing frequency of 25 ns. This data corresponds to a total integrated luminosity of  $35.9 \text{ fb}^{-1}$ . The reconstructed data in mini-AOD format, with only certified runs and luminosity sections selected using an official JSON<sup>4</sup> file, have been used. The list of data samples split in different run era ranging from B to H and the name of JSON file are presented in Table 4.1.

Data Samples	Run Range	Luminosity ( $\text{fb}^{-1}$ )
/SinglePhoton/Run2016B-03Feb2017_ver2-v2/MINIAOD	273150 – 275376	5.788
/SinglePhoton/Run2016C-03Feb2017-v1/MINIAOD	275656 – 276283	2.573
/SinglePhoton/Run2016D-03Feb2017-v1/MINIAOD	276315 – 276811	4.248
/SinglePhoton/Run2016E-03Feb2017-v1/MINIAOD	276831 – 277420	4.009
/SinglePhoton/Run2016F-03Feb2017-v1/MINIAOD	277932 – 278808	3.102
/SinglePhoton/Run2016G-03Feb2017-v1/MINIAOD	278820 – 280385	7.540
/SinglePhoton/Run2016H-03Feb2017_ver2-v1/MINIAOD	281613 – 284035	8.391
/SinglePhoton/Run2016H-03Feb2017_ver3-v1/MINIAOD	284036 – 284044	0.215
Total	273150 – 284044	35.866
<b>JSON File</b>		
Cert_271036-284044_13TeV_23Sep2016ReReco_Collisions16_JSON.txt		

Table 4.1: List of data samples along with corresponding run ranges and integrated luminosity. The JSON file used to select certified runs and luminosity sections is also listed.

#### 4.2.1.2 Signal MC

The signal MC samples for  $q^* \rightarrow \gamma + \text{jet}$  and  $b^* \rightarrow \gamma + b\text{-jet}$  are generated and simulated at the leading order (LO) using PYTHIA 8.212 event generator [162] and GEANT4 [172] detector simulator, for three different values of the coupling multiplier, viz.  $f = 1.0, 0.5$  and  $0.1$ . These resonance signals are generated at different masses in the range from 0.5 to 9.0 TeV at an interval of 1 TeV for  $q^*$  and 0.5 to 5.0 TeV at an interval of 0.5 TeV for  $b^*$ , to explore the entire mass range. The simulation is performed using the CUETP8M1 underlying event tune [174, 175], with renormalization and factorization scale set to,  $\mu = p_T$  of hard-scattered

<sup>4</sup>A JSON file is a special java format file that lists the good runs and luminosity sections collected with optimum detector conditions. The JSON files are located at the link: <https://cms-service-dqm.web.cern.ch/cms-service-dqm/CAF/certification/Collisions16/13TeV/ReReco/>

partons, and NNPDF2.3LO parton distribution function (PDF) [176]. The list of all the samples along with the number of generated events and cross-sections is presented in Table 4.2 for  $q^*$  and in Table 4.3 for  $b^*$ .

Sample Name	Events	Cross section (in pb)	Coupling
QstarToGJ_M-500_f-1p0_TuneCUETP8M1_13TeV-pythia8	299,760	3.033E+2	1.0
QstarToGJ_M-1000_f-1p0_TuneCUETP8M1_13TeV-pythia8	296,364	1.632E+1	1.0
QstarToGJ_M-2000_f-1p0_TuneCUETP8M1_13TeV-pythia8	99,499	5.213E-1	1.0
QstarToGJ_M-3000_f-1p0_TuneCUETP8M1_13TeV-pythia8	74,879	4.272E-2	1.0
QstarToGJ_M-4000_f-1p0_TuneCUETP8M1_13TeV-pythia8	73,482	4.8E-3	1.0
QstarToGJ_M-5000_f-1p0_TuneCUETP8M1_13TeV-pythia8	74,918	5.835E-4	1.0
QstarToGJ_M-6000_f-1p0_TuneCUETP8M1_13TeV-pythia8	75,000	7.076E-5	1.0
QstarToGJ_M-7000_f-1p0_TuneCUETP8M1_13TeV-pythia8	50,000	8.66E-6	1.0
QstarToGJ_M-8000_f-1p0_TuneCUETP8M1_13TeV-pythia8	49,814	1.283E-6	1.0
QstarToGJ_M-9000_f-1p0_TuneCUETP8M1_13TeV-pythia8	50,000	2.985E-7	1.0
QstarToGJ_M-500_f-0p5_TuneCUETP8M1_13TeV-pythia8	300,000	7.378E+1	0.5
QstarToGJ_M-1000_f-0p5_TuneCUETP8M1_13TeV-pythia8	99,723	4.129	0.5
QstarToGJ_M-2000_f-0p5_TuneCUETP8M1_13TeV-pythia8	100,000	1.328E-1	0.5
QstarToGJ_M-3000_f-0p5_TuneCUETP8M1_13TeV-pythia8	75,000	1.095E-2	0.5
QstarToGJ_M-4000_f-0p5_TuneCUETP8M1_13TeV-pythia8	72,816	1.212E-3	0.5
QstarToGJ_M-5000_f-0p5_TuneCUETP8M1_13TeV-pythia8	75,000	1.437E-4	0.5
QstarToGJ_M-6000_f-0p5_TuneCUETP8M1_13TeV-pythia8	74,776	1.62E-5	0.5
QstarToGJ_M-7000_f-0p5_TuneCUETP8M1_13TeV-pythia8	49,520	1.672E-6	0.5
QstarToGJ_M-8000_f-0p5_TuneCUETP8M1_13TeV-pythia8	49,427	1.647E-7	0.5
QstarToGJ_M-9000_f-0p5_TuneCUETP8M1_13TeV-pythia8	50,000	2.329E-8	0.5
QstarToGJ_M-500_f-0p1_TuneCUETP8M1_13TeV-pythia8	99,681	2.955	0.1
QstarToGJ_M-1000_f-0p1_TuneCUETP8M1_13TeV-pythia8	99,254	1.655E-1	0.1
QstarToGJ_M-2000_f-0p1_TuneCUETP8M1_13TeV-pythia8	75,000	5.315E-3	0.1
QstarToGJ_M-3000_f-0p1_TuneCUETP8M1_13TeV-pythia8	75,000	4.356E-4	0.1
QstarToGJ_M-4000_f-0p1_TuneCUETP8M1_13TeV-pythia8	72,312	4.861E-5	0.1
QstarToGJ_M-5000_f-0p1_TuneCUETP8M1_13TeV-pythia8	75,000	5.715E-6	0.1
QstarToGJ_M-6000_f-0p1_TuneCUETP8M1_13TeV-pythia8	49,942	6.241E-7	0.1
QstarToGJ_M-7000_f-0p1_TuneCUETP8M1_13TeV-pythia8	49,910	5.973E-8	0.1
QstarToGJ_M-8000_f-0p1_TuneCUETP8M1_13TeV-pythia8	49,650	4.515E-9	0.1
QstarToGJ_M-9000_f-0p1_TuneCUETP8M1_13TeV-pythia8	49,814	2.655E-10	0.1

Table 4.2: MC samples for  $q^*$  signal, simulated and reconstructed at  $\sqrt{s} = 13$  TeV.

Sample Name	Events	Cross section (in pb)	Coupling
BstarToGJ_M-500_f-1p0_TuneCUETP8M1_13TeV-pythia8	100,000	6.236	1.0
BstarToGJ_M-1000_f-1p0_TuneCUETP8M1_13TeV-pythia8	99,736	2.148E-1	1.0
BstarToGJ_M-1500_f-1p0_TuneCUETP8M1_13TeV-pythia8	73,990	2.204E-2	1.0
BstarToGJ_M-2000_f-1p0_TuneCUETP8M1_13TeV-pythia8	75,000	3.585E-3	1.0
BstarToGJ_M-2500_f-1p0_TuneCUETP8M1_13TeV-pythia8	75,000	7.488E-4	1.0
BstarToGJ_M-3000_f-1p0_TuneCUETP8M1_13TeV-pythia8	73,170	1.766E-4	1.0
BstarToGJ_M-3500_f-1p0_TuneCUETP8M1_13TeV-pythia8	50,000	4.517E-5	1.0
BstarToGJ_M-4000_f-1p0_TuneCUETP8M1_13TeV-pythia8	48,100	1.202E-5	1.0
BstarToGJ_M-4500_f-1p0_TuneCUETP8M1_13TeV-pythia8	50,000	3.289E-6	1.0
BstarToGJ_M-5000_f-1p0_TuneCUETP8M1_13TeV-pythia8	49,608	9.216E-7	1.0
BstarToGJ_M-500_f-0p5_TuneCUETP8M1_13TeV-pythia8	99,544	1.574	0.5
BstarToGJ_M-1000_f-0p5_TuneCUETP8M1_13TeV-pythia8	100,000	5.438E-2	0.5
BstarToGJ_M-1500_f-0p5_TuneCUETP8M1_13TeV-pythia8	75,000	5.666E-3	0.5
BstarToGJ_M-2000_f-0p5_TuneCUETP8M1_13TeV-pythia8	74,404	9.162E-4	0.5
BstarToGJ_M-2500_f-0p5_TuneCUETP8M1_13TeV-pythia8	74,409	1.884E-4	0.5
BstarToGJ_M-3000_f-0p5_TuneCUETP8M1_13TeV-pythia8	72,730	4.393E-5	0.5
BstarToGJ_M-3500_f-0p5_TuneCUETP8M1_13TeV-pythia8	49,150	1.112E-5	0.5
BstarToGJ_M-4000_f-0p5_TuneCUETP8M1_13TeV-pythia8	50,000	2.909E-6	0.5
BstarToGJ_M-4500_f-0p5_TuneCUETP8M1_13TeV-pythia8	50,000	7.705E-7	0.5
BstarToGJ_M-5000_f-0p5_TuneCUETP8M1_13TeV-pythia8	50,000	2.027E-7	0.5
BstarToGJ_M-500_f-0p1_TuneCUETP8M1_13TeV-pythia8	99,033	6.357E-2	0.1
BstarToGJ_M-1000_f-0p1_TuneCUETP8M1_13TeV-pythia8	99,040	2.175E-3	0.1
BstarToGJ_M-1500_f-0p1_TuneCUETP8M1_13TeV-pythia8	75,000	2.278E-4	0.1
BstarToGJ_M-2000_f-0p1_TuneCUETP8M1_13TeV-pythia8	73,936	3.674E-5	0.1
BstarToGJ_M-2500_f-0p1_TuneCUETP8M1_13TeV-pythia8	75,000	7.595E-6	0.1
BstarToGJ_M-3000_f-0p1_TuneCUETP8M1_13TeV-pythia8	74,911	1.768E-6	0.1
BstarToGJ_M-3500_f-0p1_TuneCUETP8M1_13TeV-pythia8	50,000	4.454E-7	0.1
BstarToGJ_M-4000_f-0p1_TuneCUETP8M1_13TeV-pythia8	50,000	1.155E-7	0.1
BstarToGJ_M-4500_f-0p1_TuneCUETP8M1_13TeV-pythia8	46,590	3.031E-8	0.1
BstarToGJ_M-5000_f-0p1_TuneCUETP8M1_13TeV-pythia8	49,388	7.703E-9	0.1

Table 4.3: MC samples for  $b^*$  signal, simulated and reconstructed at  $\sqrt{s} = 13$  TeV.



The signal shapes of  $q^*$  and  $b^*$  signals for different masses and different coupling multipliers, obtained by taking the probability distribution of the invariant mass of  $\gamma + \text{jet}$  and  $\gamma + b\text{-jet}$  respectively, are shown in Fig. 4.6.

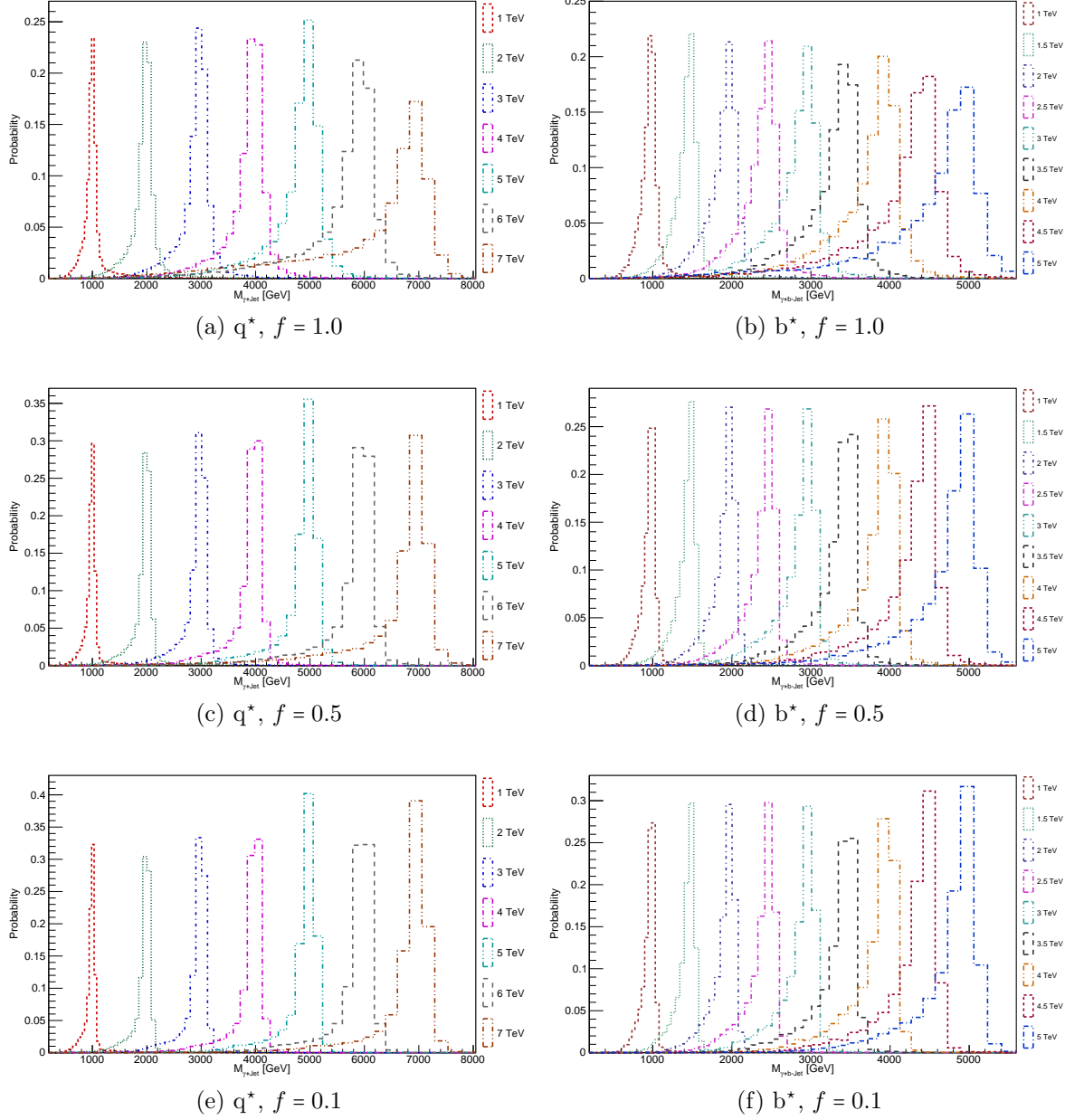


Figure 4.6: Signal shapes for  $q^*$  (left) and  $b^*$  (right) for different masses and couplings.

#### 4.2.1.3 Background MC

The list of MC samples, along with the number of generated events and process cross-section, corresponding to the three backgrounds for this study are presented in Table 4.4 below.

Sample Name	Events	Cross section (in pb)
GJets_HT-40To100_TuneCUETP8M1_13TeV-madgraphMLM-pythia8	4,467,985	20820
GJets_HT-100To200_TuneCUETP8M1_13TeV-madgraphMLM-pythia8	5,131,873	9201
GJets_HT-200To400_TuneCUETP8M1_13TeV-madgraphMLM-pythia8	10,036,487	2308
GJets_HT-400To600_TuneCUETP8M1_13TeV-madgraphMLM-pythia8	2,529,729	275.2
GJets_HT-600ToInf_TuneCUETP8M1_13TeV-madgraphMLM-pythia8	2,463,946	93.3
QCD_Pt_120to170_TuneCUETP8M1_13TeV_pythia8	6,708,572	471100
QCD_Pt_170to300_TuneCUETP8M1_13TeV_pythia8	6,958,708	117276
QCD_Pt_300to470_TuneCUETP8M1_13TeV_pythia8	4,150,588	7823
QCD_Pt_470to600_TuneCUETP8M1_13TeV_pythia8	3,959,986	648.2
QCD_Pt_600to800_TuneCUETP8M1_13TeV_pythia8	3,896,412	186.9
QCD_Pt_800to1000_TuneCUETP8M1_13TeV_pythia8	3,992,112	32.29
QCD_Pt_1000to1400_TuneCUETP8M1_13TeV_pythia8	2,999,069	9.418
QCD_Pt_1400to1800_TuneCUETP8M1_13TeV_pythia8	396,409	8.426E-1
QCD_Pt_1800to2400_TuneCUETP8M1_13TeV_pythia8	397,660	1.149E-1
QCD_Pt_2400to3200_TuneCUETP8M1_13TeV_pythia8	399,226	6.830E-3
QCD_Pt_3200toInf_TuneCUETP8M1_13TeV_pythia8	391,735	1.654E-4
DYJetsToLL_Pt-100To250_TuneCUETP8M1_13TeV-amcatnloFXFX-pythia8	2,040,596	83.12
DYJetsToLL_Pt-250To400_TuneCUETP8M1_13TeV-amcatnloFXFX-pythia8	423,976	3.047
DYJetsToLL_Pt-400To650_TuneCUETP8M1_13TeV-amcatnloFXFX-pythia8	432,056	3.921E-1
DYJetsToLL_Pt-650ToInf_TuneCUETP8M1_13TeV-amcatnloFXFX-pythia8	430,691	3.636E-2
WJetsToLNu_TuneCUETP8M1_13TeV-madgraphMLM-pythia8	29,705,748	61526.7

Table 4.4: The background MC samples used in this analysis, simulated and reconstructed at  $\sqrt{s} = 13$  TeV.

The SM  $\gamma + \text{jet}$  background has been generated using the MADGRAPH5\_amc@NLO 2.2.2 [163] event generator in different  $H_T^5$  bins, in the range of 40 – 100, 100 – 200, 200 – 400, 400 – 600 and 600 –  $\infty$  GeV with showering and hadronization carried out by the PYTHIA program. The MLM [177] matching scheme has been used to remove the double counting of the partons generated with MADGRAPH and PYTHIA.

The SM QCD dijet background has been generated using PYTHIA, with the same conditions as signal MC, in different  $p_T$  bins, in the range of 120 – 170, 170 – 300, 300 – 470, 470 – 600, 600 – 800, 800 – 1000, 1000 – 1400, 1400 – 1800, 1800 – 2400, 2400 – 3200 and 3200 –  $\infty$  GeV.

The EWK Z+jet background has been generated in different  $p_T$  bins in the range of 100 – 250, 250 – 400, 400 – 650 and 650 –  $\infty$  GeV using the AMCATNLO event generator with FFX [177] matching scheme and PYTHIA for showering and hadronization. The corresponding W+jet background is generated using the MADGRAPH event generator with MLM matching scheme and PYTHIA for showering and hadronization. All the samples use CUETP8M1 as the underlying event tune.

---

<sup>5</sup> $H_T = \sum p_T$  of all the jets in an event

## 4.3 Re-weighting of MC events

The detector data is compared with the MC samples to validate it w.r.t. the theoretical description. In order to have a fair comparison, both data and MC are kept at equal footing, by weighting the MC events corresponding to the data.

### 4.3.1 Luminosity re-weighting

The MC events are re-weighted to reflect the data luminosity. The relevant luminosity weight per event applied to MC is:

$$w_{\text{lumi}} = \frac{\sigma_{\text{process}} \times \mathcal{L}_{\text{data}}}{N_{\text{process}}} \quad (4.1)$$

where  $\sigma_{\text{process}}$  and  $N_{\text{process}}$  are the theoretical cross-section and the number of generated events for the simulated process and  $\mathcal{L}_{\text{data}}$  is the total integrated luminosity of data.

### 4.3.2 Pile-up re-weighting

In high-luminosity colliders, each bunch crossing may result into many inelastic interactions, with the number of interactions being proportional to the instantaneous luminosity of the collision. These additional interactions are attributed to as the pile-up (PU) interactions. These pile-up events can affect the reconstruction efficiency and can appear in the  $p_T$  distribution of the reconstructed objects. The presence of pile-up can affect the current analysis in two ways: additional energy from PU can be added to the reconstructed jet energy, thereby, worsening the jet energy measurement and tracks and calorimeter energy deposits from PU interactions can get added to the isolation energy sum of photons, thereby, making the isolation cuts less efficient. However, a number of techniques are developed and centrally validated in CMS to alleviate the deterioration of object reconstruction due to PU effects. To minimize the impact of PU interactions, various cuts applied for object selection and energy corrections are optimized so that in the end, the effect is almost negligible.

The simulated samples are also generated with additional pile-up to match with the actual data taking conditions. The samples used in this analysis are generated with 2015\_25ns\_Startup\_PoissonOOTPU [178] pile-up scenario. Still, the residual differences in the pile-up distributions of data and MC are corrected by means of

pile-up re-weighting. In this process, the pileup distribution for data is taken from the instantaneous luminosity per bunch crossing for each luminosity section, and the total pp inelastic cross-section of 69.2 mb, using the officially recommended procedure [178]. A Poissonian smearing is used to model the statistical fluctuations in the actual pileup events present in the data. For MC, the true number of interactions per event are considered as the pileup distribution. These pile-up distributions in data and MC are compared corresponding to the number of primary vertices and a weight factor is calculated on the event by event basis. This weight factor is then multiplied to the luminosity weight factor to get the total event weight applied to the Monte Carlo events. To give an account of the effect, a data-MC comparison of the number of vertices in an event has been shown in Fig. 4.7, before and after applying the pile-up re-weighting.

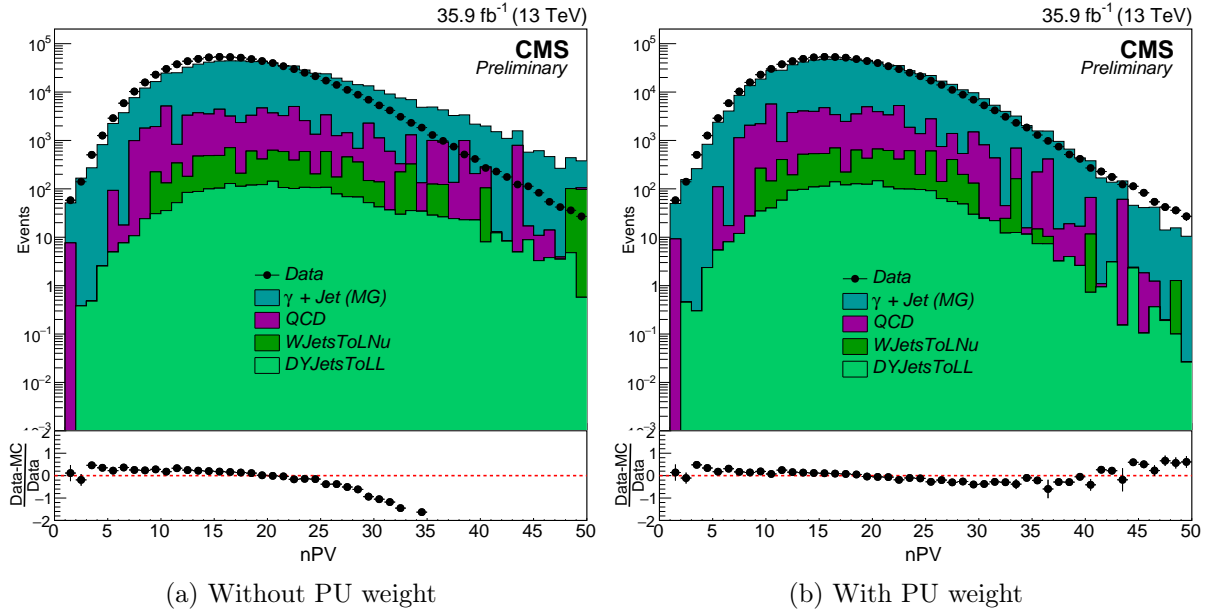


Figure 4.7: Data-MC comparison of the number of vertices in an event, showing the effect of pile-up re-weighting.

## 4.4 Event selection

In this analysis, we are searching for the possible signatures of excited quarks decaying into a photon and a jet final state. So the experimental technique of event selection starts with the measurement of the inclusive process,  $pp \rightarrow \gamma + \text{jet} + X$  where we require at least one hard photon and one hard jet in the event,  $X$  refers to the additional photons or jets or anything else that can be present in

the event. The events containing these additional particles are not vetoed as it would unnecessarily restrict our signal to a narrow topology. The event statistics for the search of excited b-quark is formed by requiring the selected jet to be a b-jet. Based on the type of the jet, three different event categories are made:

- **Inclusive category:** Events containing photons and jets where jets can be the light jets or the b-jets. This forms the event statistics for  $q^*$  search.
- **Exclusive 1 b-tag category:** Events containing photons and b-jets, forming the event statistics for  $b^*$  search.
- **Exclusive 0 b-tag category:** Events containing photons and non b-jets. This category is also used in  $b^*$  search in order to overcome any loss of statistical power due to migration of events from one category to another.

The selection criteria used in this analysis is described in detail in the sections below:

#### 4.4.1 Trigger selection

The trigger system of the CMS experiment is designed to select interesting physics events of good quality. As mentioned in Section 2.2.2, it consists of two levels: the L1 trigger and the HLT trigger. The data sample used in this analysis is required to pass the L1\_SingleEG40 trigger, which selects the events that have at least one  $e/\gamma$  candidate with  $E_T > 40$  GeV and HLT\_Photon165\_HE10 trigger, which is a single photon trigger requiring the events to have at least one photon candidate with  $p_T > 165$  GeV and H/E fraction  $< 10\%$ . The HLT path is required to be un-prescaled for the entire data taking period, so that all events passing the trigger are stored for further analysis.

The offline trigger efficiency of HLT trigger, also referred to as the trigger turn-on, has been studied as a function of the leading photon  $p_T$  in order to observe any inefficiencies. The trigger turn-on measured w.r.t. the same object dataset is referred to as the relative trigger efficiency while the trigger turn-on measured w.r.t. an orthogonal dataset is referred to as the absolute trigger efficiency, as the relative trigger efficiency can not reveal the presence of any systematic detector effect. The idea is to identify unbiased photon candidates in data and measure the frequency of photons activating the trigger decision. The trigger efficiency in this analysis has been evaluated w.r.t. the lower  $p_T$  prescaled photon, jet and muon

reference triggers, as listed in Table 4.5. This efficiency is measured by selecting the events passing the lower  $p_T$  threshold triggers and computing the rate at which these events also pass the main analysis trigger. The trigger turn-on curve for all the three reference triggers is presented in Fig. 4.8.

Analysis trigger	Photon ref. triggers	Jet ref. triggers	Muon ref. triggers
HLT_Photon165_HE10	HLT_Photon75	HLT_PFJet60	HLT_Mu50
	HLT_Photon90	HLT_PFJet80	
	HLT_Photon120	HLT_PFJet140	

Table 4.5: Different triggers used in the trigger efficiency study.

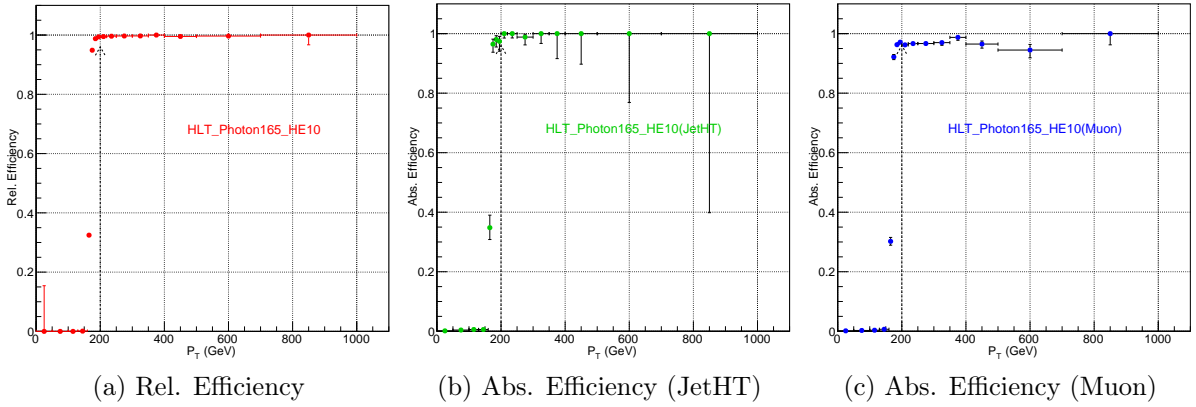


Figure 4.8: Relative and absolute trigger efficiencies for the single photon trigger, HLT\_Photon165\_HE10.

It can be seen that the trigger become fully efficient and reaches the plateau region at around 200 GeV, for photon and jet reference triggers. However, the turn-on w.r.t. the muon reference trigger is found to be around 95% efficient with a sizable uncertainty which is taken into account as a systematic uncertainty.

#### 4.4.2 MET filters

While monitoring the quality of detector data during offline processing, a number of noisy events were reported, which are removed by applying a set of officially recommended noise cleaning filters, listed below:

- **CSC tight beam halo filter:** rejects muons from beam halo.
- **HBHE noise filter with isolated noise rejection:** rejects noisy events in HCAL.

- **HCAL laser filter:** removes events that contains HCAL calibration laser firing within the collision bunch-crossing.
- **ECAL dead cell trigger primitive filter:** rejects events containing large missing energy coming from masked crystals.
- **Bad EE supercrystal filter:** removes events that contains two EE crystals with anomalously high energies.

#### 4.4.3 Primary vertex selection

A typical pp collision event may contain more than one reconstructed primary vertex coming from in-time and out-of-time bunch crossings, pile-up events etc. But, the events that have at least one primary vertex coming from in-time collision are kept for further study. These events are selected by requiring the vertex to be within 24 cm of the nominal collision point along the z-direction and within 2 cm in the radial direction. The vertex should have at least 4 associated tracks, along with the largest value of  $\sum p_T^2$  of all the tracks and have a proper 3d vertex fit with the tracks.

#### 4.4.4 Analysis object selection: Photon

In each event passing the primary vertex selection, we search for a well identified and isolated photon candidate by using the criteria explained in Section 3.1.3.2. The cut-off value used for each variable is listed below:

- $\sigma_{i\eta i\eta} < 0.01022$ .
- Single tower H/E < 0.0396.
- Conversion safe electron veto = true.
- PF charged hadron isolation < 0.441.
- PF neutral hadron isolation <  $2.725 + 0.0148 \times p_T^\gamma + 0.000017 \times (p_T^\gamma)^2$ .
- PF photon isolation <  $2.571 + 0.0047 \times p_T^\gamma$ .

The photon isolation cone is susceptible to a diffuse background of soft particles coming from the underlying events or pile-up events. So the isolation variables

are corrected for the presence of these additional interactions using the following relation:

$$\text{Iso}^{\text{corrected}} = \max.(\text{Iso}^{\text{original}} - \rho_{\text{event}} \times A_{\text{eff}}, 0.0) \quad (4.2)$$

where,  $\rho_{\text{event}}$  is known as the energy density computed using the FastJet package [179] and is defined as the median energy density per unit area corresponding to the particles associated with the pile-up vertices. This quantity gives a measure of the pile-up activity in the event. The variable,  $A_{\text{eff}}$  is the ratio of the slopes obtained from linear fitting of  $\rho - N_{\text{vtx}}$  and Isolation- $N_{\text{vtx}}$ . The values of  $A_{\text{eff}}$  for three isolations, in different  $\eta$  regions covering barrel and endcaps, are shown in Table 4.6.

$\eta$ -bin	EA charged hadrons	EA neutral hadrons	EA photons
$ \eta  < 1.0$	0.0360	0.0597	0.1210
$1.0 <  \eta  < 1.479$	0.0377	0.0807	0.1107
$1.479 <  \eta  < 2.0$	0.0306	0.0629	0.0699
$2.0 <  \eta  < 2.2$	0.0283	0.0197	0.1056
$2.2 <  \eta  < 2.3$	0.0254	0.0184	0.1457
$2.3 <  \eta  < 2.4$	0.0217	0.0284	0.1719
$ \eta  > 2.4$	0.0167	0.0591	0.1998

Table 4.6: Effective area for different photon isolations.

In order to avoid non-collision backgrounds coming from the anomalous calorimetric signals resulting due to the direct ionization of Avalanche Photo-diodes (APDs) by a highly ionizing particle such as a proton and depositing all the energy within a single ECAL crystal (known as “spikes”), a minimal requirement on the rectangular ratios and shower shape profiles, as mentioned below, are also placed:

- $R_9 < 1.0$ .
- $\sigma_{i\eta i\eta} > 0.001$ .
- $\sigma_{i\phi i\phi} > 0.001$ .

This selection results into a collection of photons in each event, out of which, the highest  $p_T$  photon (known as leading photon) is selected and is required to be greater than 200 GeV, the  $p_T$  value at which the trigger turn-on curve becomes 100% efficient. The selected photon is also required to be in the central barrel region of the detector, that is,  $|\eta| < 1.4442$ . This requirement is placed since the  $q^*$



or  $b^*$  resonances (if exists), produced via hard scattering, would decay mostly into back-to-back  $\gamma$  and jet and are expected to be detected in the central region of the detector. A comparison of Data vs. MC for different photon variables, after the final selection, is presented in Fig. 4.9.

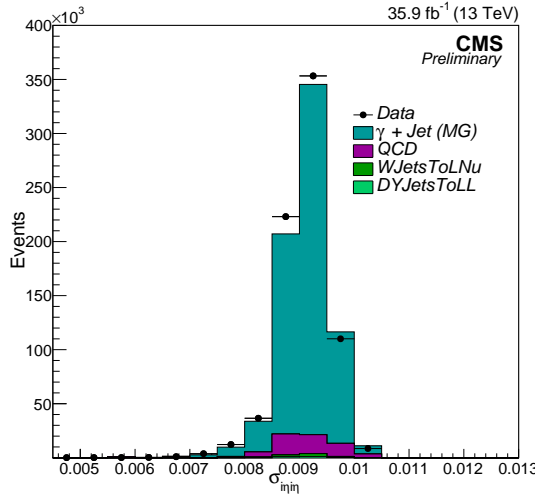
#### 4.4.4.1 Overlap removal between $\gamma$ + jet and QCD dijet background

The QCD sample used in this analysis has been generated using PYTHIA with the process: HardQCD::all = ON, that is, at the generator level, all the processes like  $gg \rightarrow gg$ ,  $gg \rightarrow q\bar{q}$ ,  $qg \rightarrow qg$ ,  $qq \rightarrow qq$ ,  $q\bar{q} \rightarrow gg$ ,  $q\bar{q} \rightarrow q\bar{q}$  are allowed and are associated with initial and final state parton showers. Since quarks tend to hadronize as soon as they are produced, the particles in parton showers appear to come from the primary vertex. Thus, the photons present in these parton showers form the source of prompt photons in the QCD sample and can mimic a  $\gamma$  + jet event.

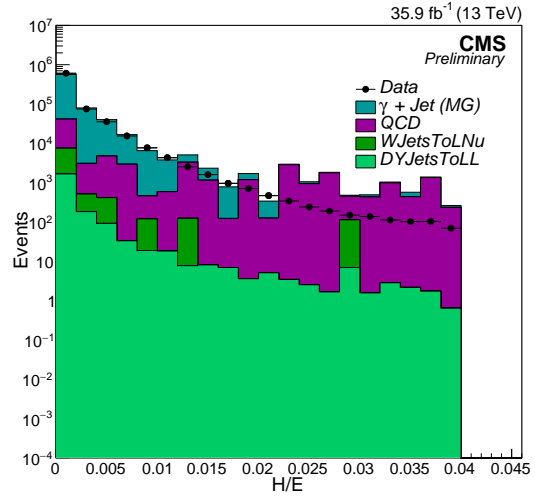
However, in QCD, since the prompt photons come from the parton showers, they have a small  $\Delta R$  separation from other gen particles. The same is visible in Fig. 4.10a which shows the  $\Delta R$  distribution between genPhotons and genPartons in the QCD sample. On the other hand, in  $\gamma$  + jet sample, the prompt photons come from the hard process and hence are largely separated from other particles as can be seen in Fig. 4.10b.

The events containing these prompt photons in QCD sample are removed in order to avoid double counting of events between  $\gamma$  + jet and QCD dijet samples. The procedure followed to remove the overlap is summarized as follows:

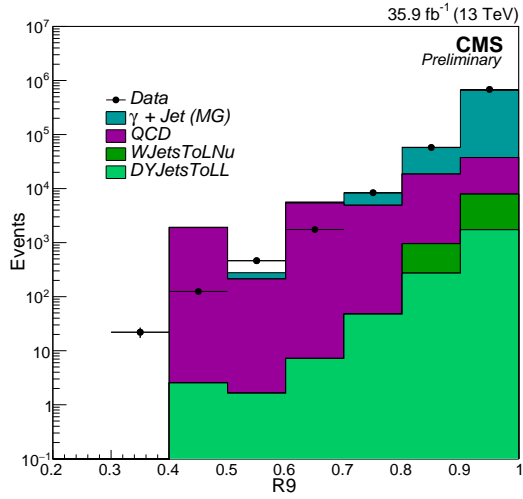
- In a QCD event, a gen photon corresponding to the selected reco photon is searched by requiring, gen particle ID = 22,  $\Delta R(\text{Gen}, \text{Reco}) < 0.1$  and  $\frac{\Delta p_T}{p_T}(\text{Gen}, \text{Reco}) < 0.1$ . Once the gen photon is found, its prompt status is checked using its gen level properties. If it is prompt, the event is removed from the event collection, otherwise not.
- Since  $\gamma$  + jet MC sample has a gen level cut of  $\Delta R(\gamma, \text{Parton}) > 0.05$ , so the events with only  $\Delta R(\gamma, \text{Parton}) > 0.05$  are removed from the QCD sample.
- The events with  $\Delta R(\gamma, \text{Parton}) < 0.05$  (if any) are, then, removed from the  $\gamma$  + jet MC sample.



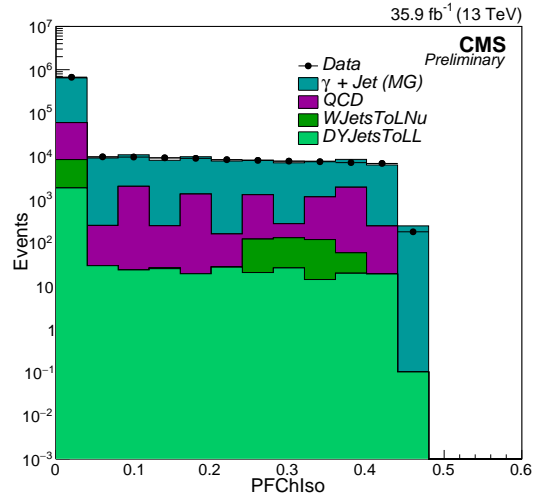
(a)  $\sigma_{i\eta i\eta}$



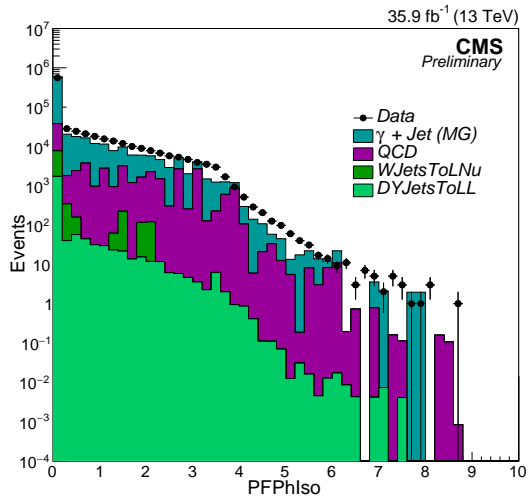
(b) Single Tower H/E



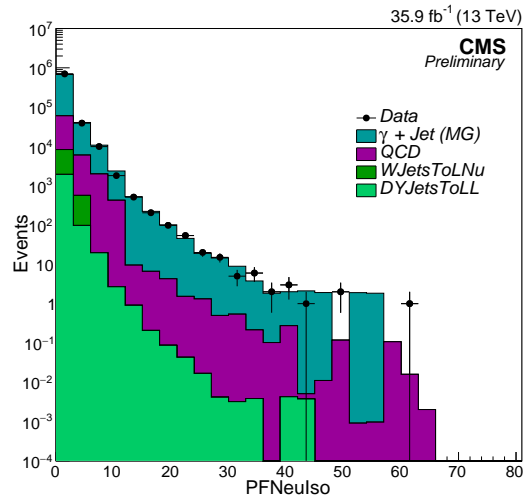
(c) R9



(d) PF Charged Hadron Isolation



(e) PF Photon Isolation



(f) PF Neutral Hadron Isolation

Figure 4.9: Data-MC comparison of photon identification and isolation variables after final selection.

The Fig. 4.10c shows the stitching of the two samples in  $\Delta R$  after overlap removal. It can be seen that the stitching behaves nicely at the  $\Delta R$  cut.

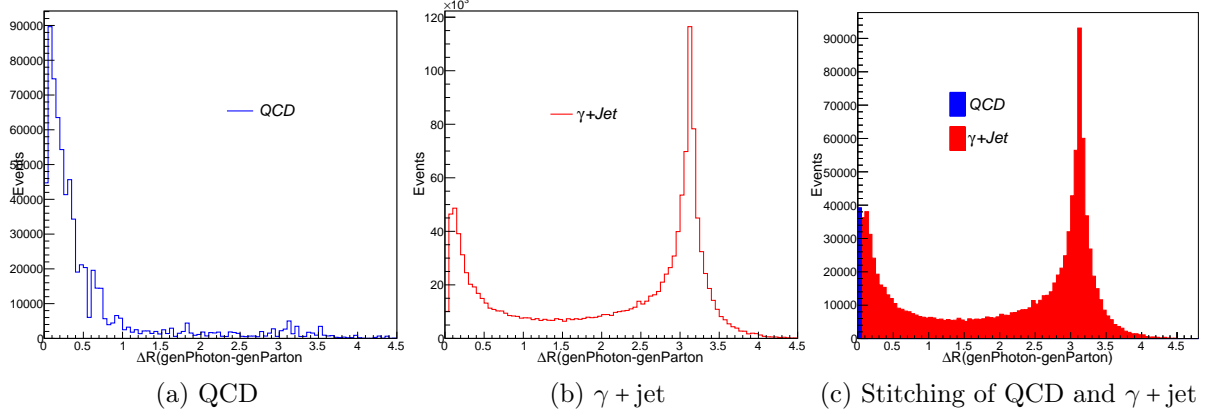


Figure 4.10:  $\Delta R$  distribution between prompt gen photon matched to selected reco photon and other gen particles: (a) QCD before overlap removal, (b)  $\gamma + \text{jet}$  before overlap removal, (c) Stitching of QCD and  $\gamma + \text{jet}$  after overlap removal.

#### 4.4.5 Analysis object selection: Jet

Events containing a good photon candidate are further inspected for the presence of an AK4 jet using the identification criteria mentioned in Section 3.1.4.4. The cut-off values used for different variables is listed below. The jets qualifying this selection are required to be away from the selected photon by  $\Delta R > 0.5$ , to ensure that they are different objects and not the fragments of the same particle.

- Charged hadron fraction  $> 0$ .
- Neutral hadron fraction  $< 0.90$ .
- Charged EM fraction  $< 0.99$ .
- Neutral EM fraction  $< 0.90$ .
- Number of constituents  $> 1$ .
- Charged multiplicity  $> 0$ .

Out of the selected jet collection, the jet with highest  $p_T$  is considered and is required to have a  $p_T > 170 \text{ GeV}$  and  $|\eta| < 2.4$ . A nearly symmetric cut on the  $p_T$  of photon and jet is considered since the photons and jets in the signal samples are distributed symmetrically in  $p_T$  as can be seen for  $q^*$  samples in Fig. 4.11.

In order to overcome the non-linear response of the detector, L1, L2, L3 and L2L3 corrections as mentioned in Section 3.1.4.2 are applied. A comparison of Data and MC for different jet variables after final selection is shown in Fig. 4.12.

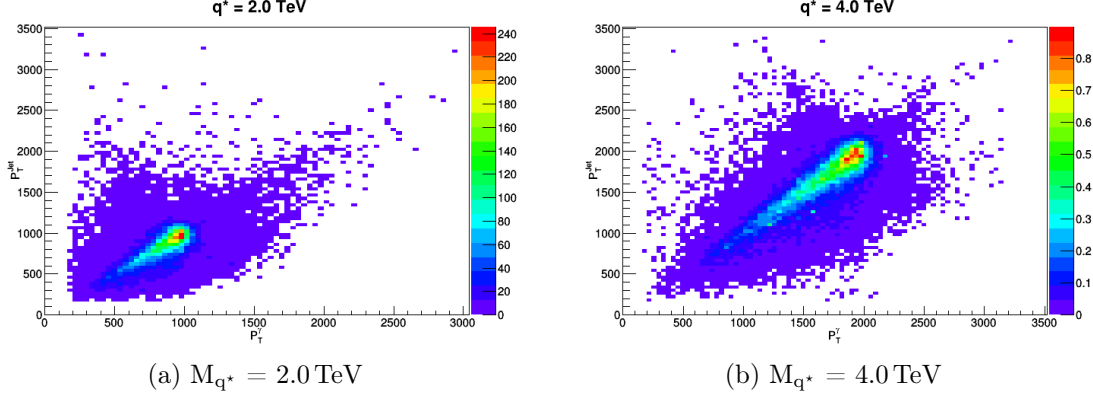


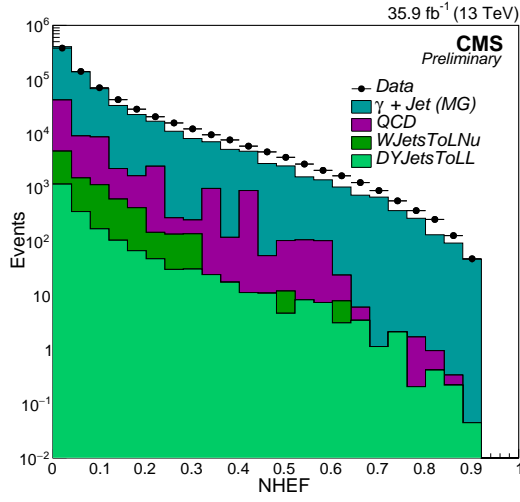
Figure 4.11:  $p_T^\gamma$  vs.  $p_T^{\text{jet}}$  in 2-dimensional representation for  $q^*$  signals.

#### 4.4.6 Analysis object selection: b-Jet

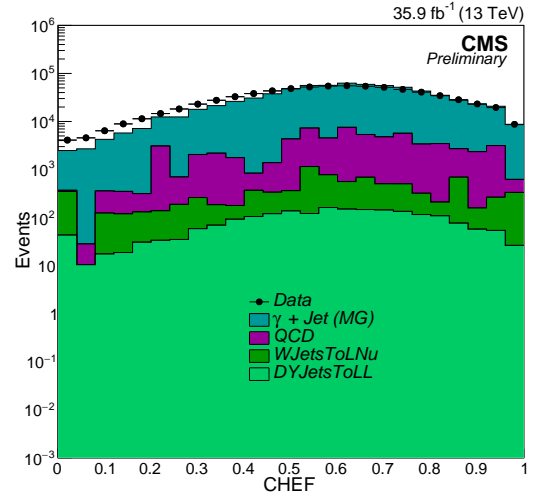
The selected jet in each event is examined for its b-tagging status using the “CSVv2” (explained in Section 3.1.4.3) discriminator. A cut-off value of 0.5426, corresponding to the loose working point, has been used and all the jets with b-tag discriminator value greater than the cut-off value are considered as b-jets.

In general, the b-jet identification efficiency and  $c$ /light-jet misidentification probability of a tagger is not the same in data and MC. These observed differences are taken into account by means of the b-tag scale factors (SF) defined as,  $\text{SF} = \frac{\epsilon_{\text{data}}}{\epsilon_{\text{MC}}}$ , where  $\epsilon_{\text{data}}$  and  $\epsilon_{\text{MC}}$  are the b-tagging efficiencies of CSVv2 discriminator in data and MC simulation, respectively. These SFs, in CMS, are determined using the dedicated techniques, described in [157, 158]. The SFs are dependent on jet flavor, jet  $p_T$  and jet  $\eta$ . The official recommendations for computing these scale factors and errors on them are provided in [180]. The SFs are available for the  $p_T$  range of 20–1000 GeV and  $|\eta| < 2.4$ . For values above the  $p_T$  limit, the recommendations are to use the SF values at the limits with double the uncertainty while for values above the  $\eta$  limits, the SF values are taken equal to zero.

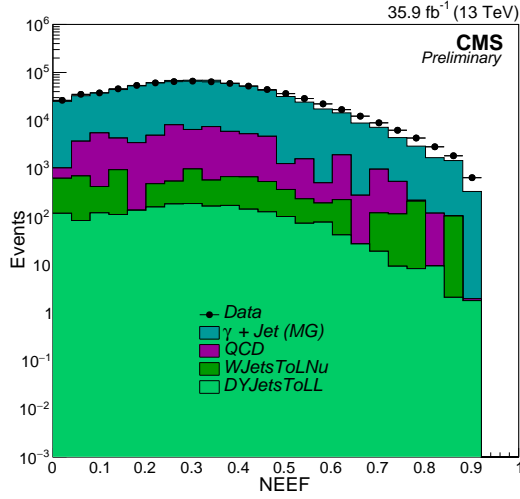
Errors on b-tag scale factors arise from various systematic uncertainties, like the jet energy scale uncertainty, the sample purity which is the contamination of jets with a flavor complementary to the one for which the scale factor is being measured, the uncertainty on the scale factor for  $c$ -jets and the uncertainty due to



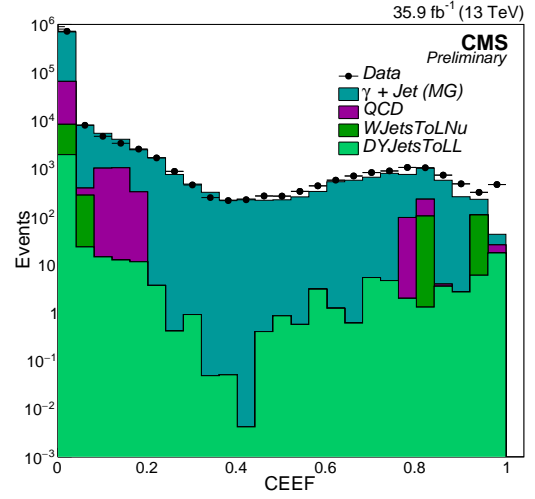
(a) Neutral Hadron Energy Fraction



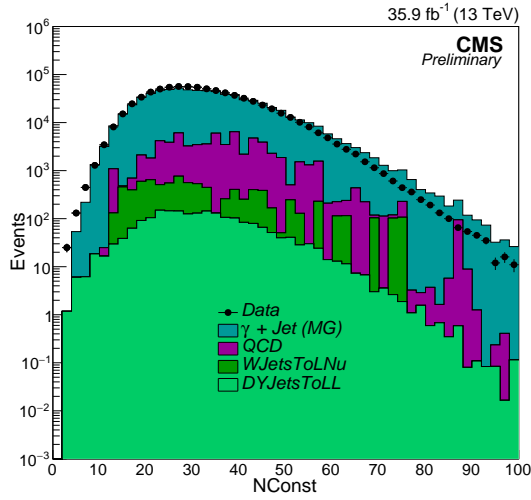
(b) Charged Hadron Energy Fraction



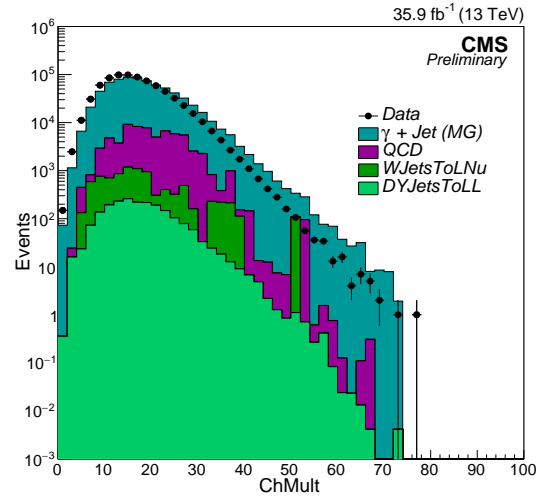
(c) Neutral EM Energy Fraction



(d) Charged EM Energy Fraction



(e) Number of Constituents



(f) Charged Multiplicity

Figure 4.12: Data-MC comparison of jet particle flow identification variables after final selection.

finite number of events in the simulation which results into statistical fluctuations etc. These errors are evaluated as the differences in the scale factors for central and up/down systematic type as mentioned in [180] and are used as a source of systematic uncertainty due to the b-tagging.

In principle, the SF value provides the fraction of actual b-jets among the jets passing the discriminator cut. Based on this terminology, two b-tag categories are formed:

- 1 b-tag category = Jets passing the discriminator  $\times$  SF.
- 0 b-tag category = Jets passing the discriminator  $\times$  (1 - SF) + Jets failing the discriminator.

So the 1 b-tag category essentially gives the fraction of b-jets and the 0 b-tag category gives the fraction of non b-jets, called as the 1 and 0 b-tag efficiencies of discriminator. A Data-MC comparison of the CSVv2 discriminator before and after applying the b-tagging is shown in Fig. 4.13. The 0 b-tag category may contain the jets passing the discriminator, with a weight (1 - SF), as is seen in Fig. 4.13b.

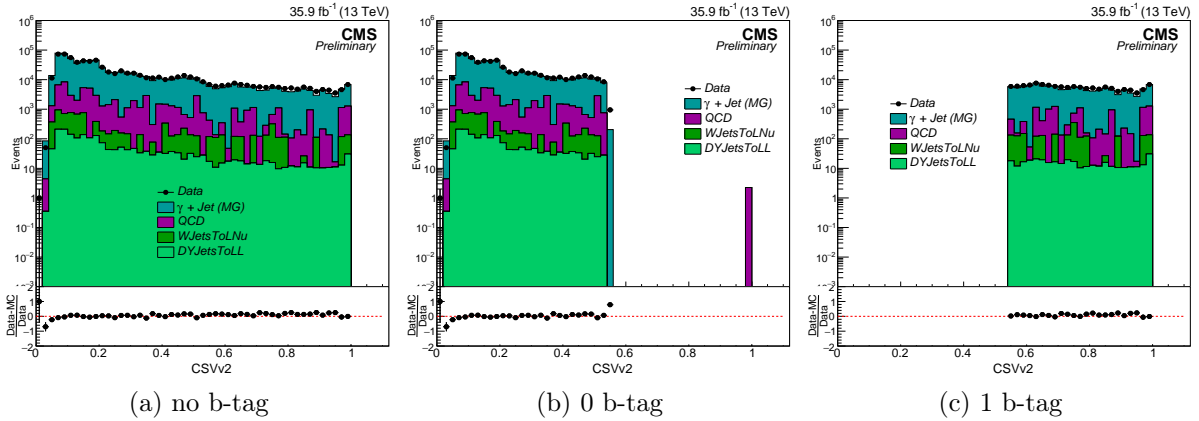


Figure 4.13: Data-MC comparison of CSVv2 discriminator distribution before and after applying the b-tagging.

#### 4.4.7 Kinematical restrictions between $\gamma$ and jet/b-jet

The  $\gamma$  + jet final state from excited quark decays would be produced through a s-channel process and has an isotropic distribution of final state particles. On the other hand, the  $\gamma$  + jet final state from background processes would take place through a t-channel process and result into high density of particles in

forward and backward directions. Hence, to reduce these background contributions while maintaining high acceptance for the signal,  $|\Delta\eta(\gamma, \text{jet/b-jet})| < 1.5$  has been applied. Also, in order to avoid the turn-on region due to various kinematical selections, as shown in Fig. 4.14, a cut on the invariant mass of  $\gamma + \text{jet/b-jet}$ ,  $M_{\gamma+\text{jet}} = \sqrt{(E^\gamma + E^{\text{jet}})^2 - (\vec{p}^\gamma + \vec{p}^{\text{jet}})^2}$ , has been applied and is required to be greater than 700 GeV.

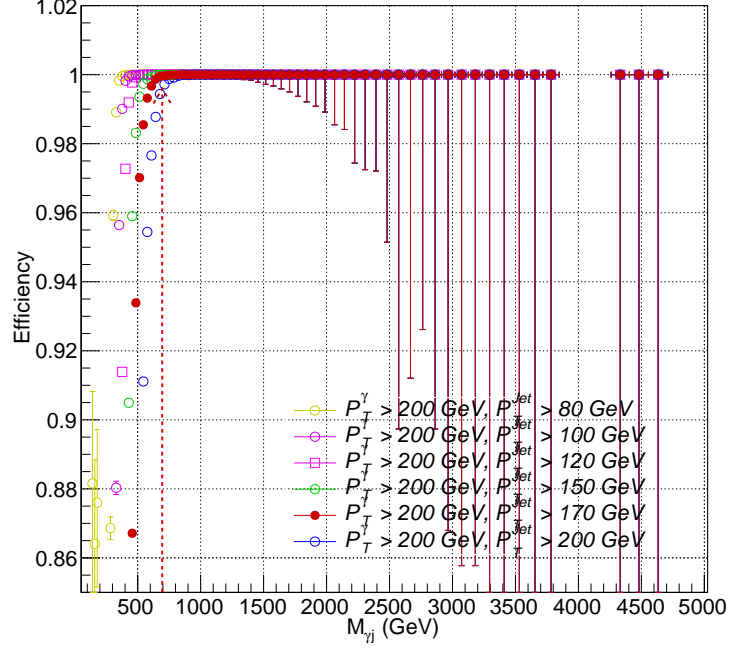


Figure 4.14: Turn-on due to various kinematical selections, plotted for different jet  $p_T$  cuts.

The theoretical predictions for  $\gamma + \text{jet}$  and dijet backgrounds are generated at the LO level using PYTHIA and MADGRAPH, so in order to include the NLO effects, the MC events are scaled with a K-factor of 1.3 [182, 183], along with the luminosity and pile-up scale factors. The cut flow table for signal, backgrounds and data, after application of all selection cuts and scale factors, is presented in Table 4.7. The SM  $\gamma + \text{jet}$  contributes about 95% of the total background while the contribution from QCD dijet background is around 4% and from electroweak background is around 1%.

The signal efficiencies for  $q^*$  and  $b^*$  signals at different mass points for  $f = 1.0$  are presented in Table 4.8 and Table 4.9 respectively. The variation of  $q^*$  and  $b^*$  selection efficiencies as a function of mass is presented in Fig. 4.15.

Cuts	q* 2 TeV	SM $\gamma$ + jet Bkg	QCD dijet Bkg	EWK Bkg	Total Bkg	Data
Total	18389.6	1.50357E+09	2.66074E+10	2.87352E+09	3.09845E+10	1.1584E+08
HLT	18389.6	1.50357E+09	2.66074E+10	2.87352E+09	3.09845E+10	3.93895E+07
MET filters	18389.6	1.50357E+09	2.66074E+10	2.87352E+09	3.09845E+10	3.74467E+07
Photon ID	12868.4	6.38738E+08	6.70708E+07	7.31732E+07	7.78982E+08	4.20307E+06
$p_T^\gamma > 200$ GeV & $ \eta^\gamma  < 1.4442$	11552.4	1.06063E+06	481691	9231.4	1.55155E+06	1.26456E+06
QCD overlap removal	11552.4	1.06007E+06	91298.3	9231.4	1.1606E+06	1.26456E+06
Jet ID	11548.1	1.05854E+06	91244.5	8953.46	1.15874E+06	1.26033E+06
$p_T^{\text{jet}} > 170$ GeV	11496.6	814187	74359.6	6393.9	894940	930191
$ \eta^{\text{jet}}  < 2.4$	11193	782291	62086.8	6179.82	850558	905346
$ \Delta\eta  < 1.5$	8270.48	652420	37343.4	5201.72	694965	748663
$M_{\gamma+\text{jet}} > 700$ GeV	8237.03	122831	4950.45	1379.37	129160	126770

Table 4.7: Selection cut flow table for signal, different backgrounds and data.

Cuts	1 TeV	2 TeV	3 TeV	4 TeV	5 TeV	6 TeV	7 TeV
Total	100	100	100	100	100	100	100
Photon ID	69.4811	69.3168	69.696	70.0057	70.2649	69.0685	67.0689
$p_T^\gamma > 200$ GeV & $ \eta^\gamma  < 1.4442$	54.6384	62.2149	63.6378	64.1612	64.5831	63.3158	61.0851
Jet ID	54.5833	62.1878	63.6138	64.149	64.5657	63.3051	61.0571
$p_T^{\text{jet}} > 170$ GeV	53.1439	61.9043	63.5149	64.0551	64.4989	63.2264	60.977
$ \eta^{\text{jet}}  < 2.4$	50.0591	60.2276	62.7361	63.6412	64.2839	63.061	60.7929
$ \Delta\eta  < 1.5$	39.2106	44.5	45.5168	45.5196	45.7801	44.6649	43.2637
$M_{\gamma+\text{jet}} > 700$ GeV	37.4718	44.317	45.4661	45.472	45.7347	44.6102	43.2077

Table 4.8: Selection efficiency (%) table for the  $q^*$  signal samples in the mass range 1.0–7.0 TeV with SM Coupling  $f = 1.0$ .

Cuts	1 TeV	1.5 TeV	2 TeV	2.5 TeV	3 TeV	3.5 TeV	4 TeV
Total	100	100	100	100	100	100	100
Photon ID	69.8006	69.6057	69.8508	70.3567	70.4957	71.1226	70.9883
$p_T^\gamma > 200$ GeV & $ \eta^\gamma  < 1.4442$	54.6467	58.3353	60.0603	61.3592	62.1837	62.5457	63.0047
Jet ID	54.6361	58.3307	60.0561	61.3549	62.1784	62.5411	62.9972
$p_T^{\text{jet}} > 170$ GeV	53.1637	57.8604	59.8709	61.2866	62.1325	62.4845	62.9699
$ \eta^{\text{jet}}  < 2.4$	52.5537	57.3699	59.4802	61.0701	61.952	62.4065	62.9059
CSVv2	35.5183	35.6018	34.2311	30.9516	28.901	28.1197	27.3777
$ \Delta\eta  < 1.5$	28.4642	26.5476	25.3583	22.5024	20.4847	19.8818	19.5085
$M_{\gamma+\text{jet}} > 700$ GeV	27.3834	26.4028	25.3119	22.4633	20.4636	19.8627	19.4598

Table 4.9: Selection efficiency (%) table for the  $b^*$  signal samples in the mass range 1.0–4.0 TeV with SM Coupling  $f = 1.0$ .



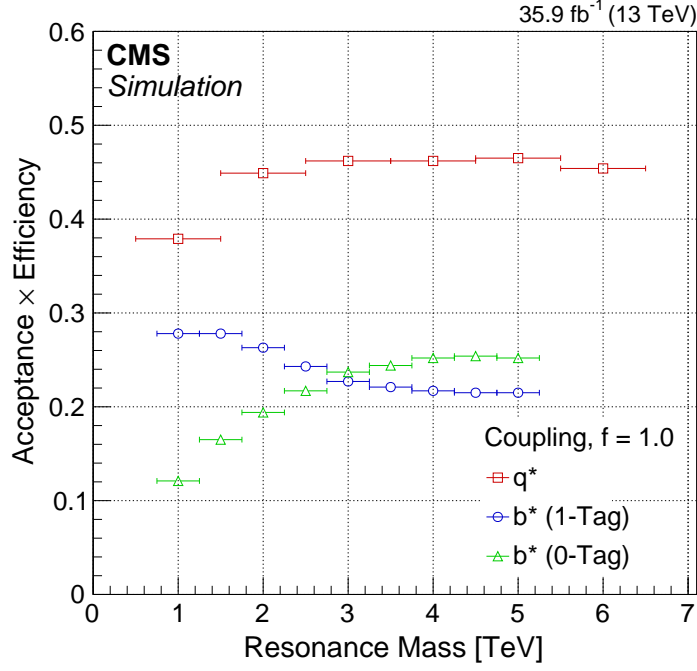


Figure 4.15: The product of acceptance and efficiency as a function of  $q^*$  and  $b^*$  mass for SM coupling,  $f = 1.0$ , obtained using MC simulation.

A comparison between Data and MC for different kinematical variables for photons and jets, after final selection, corresponding to the three categories viz. no b-tag, 1 b-tag and 0 b-tag, are presented in Fig. 4.16, Fig. 4.17 and Fig. 4.18 respectively. These distributions are found to be in reasonable agreement with the theoretical predictions. The  $p_T$  distribution for data falls steeply with the increasing  $p_T$  and agrees well with MC within the uncertainties. Likewise, the  $\eta$  distribution is in good agreement with the shape anticipated by MC.

The distributions of photons and jets in  $\Delta\eta$ ,  $\Delta\phi$  and  $\Delta R$  are also presented in Fig. 4.19. The number of photons, jets and b-jets per event are shown in Fig. 4.20. The Data-MC comparison of the invariant mass distributions of  $\gamma + \text{jet}$  and  $\gamma + \text{b-jet}$  in three categories is displayed in Fig. 4.21.

The various kinematical distributions depicted here confirm that the kinematics of analysis objects in detector data comply with the theoretical expectations. However, the theoretical MC simulations, in this analysis, are used just to check the behaviour of the data. The actual backgrounds for the processes under study, have been computed using a data driven technique by fitting the invariant mass distribution spectra with a smooth parameterization.

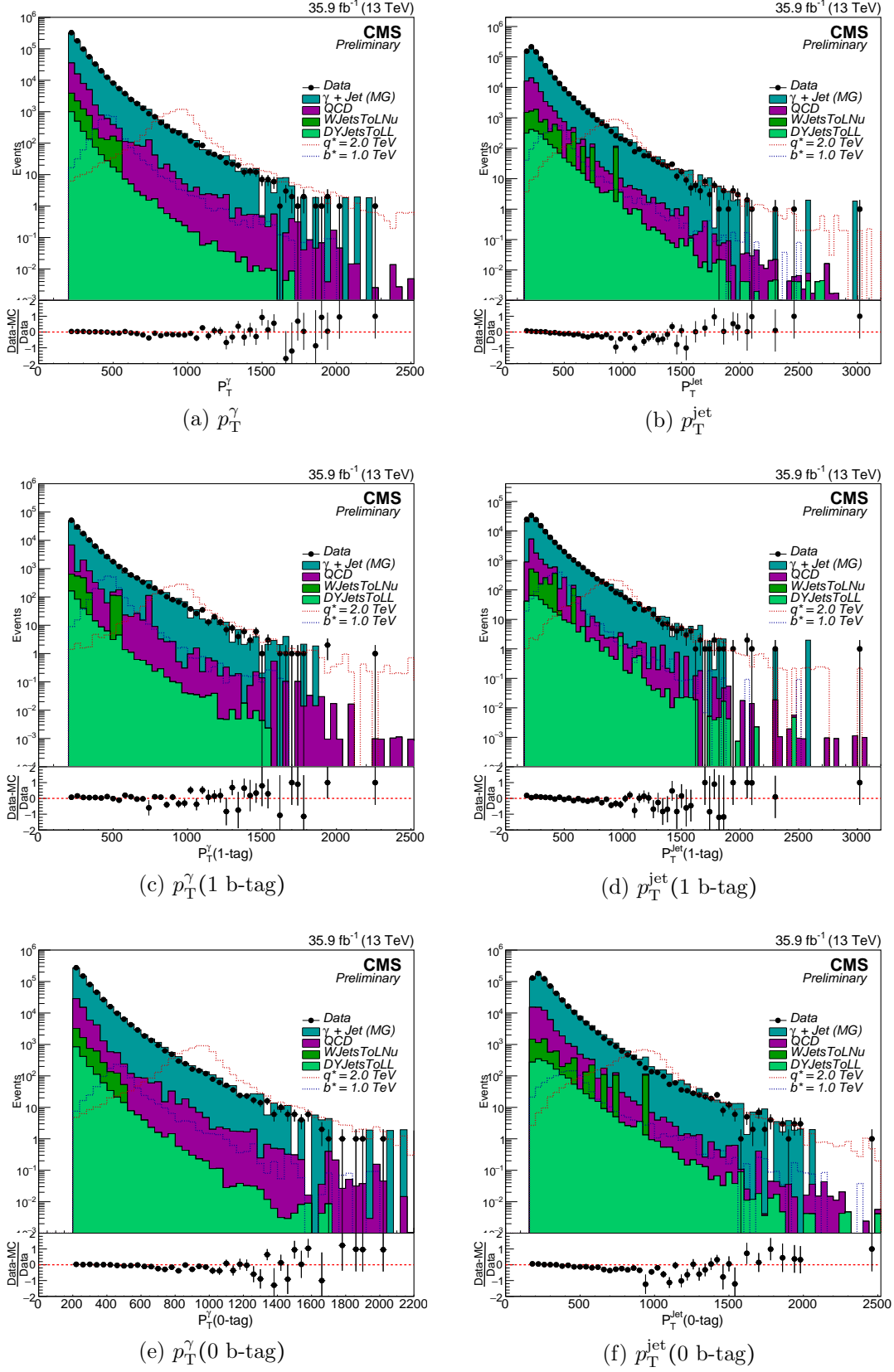


Figure 4.16: Data-MC comparison of  $p_T$  distribution of photons and jets for three categories: no b-tag, 1 b-tag and 0 b-tag.

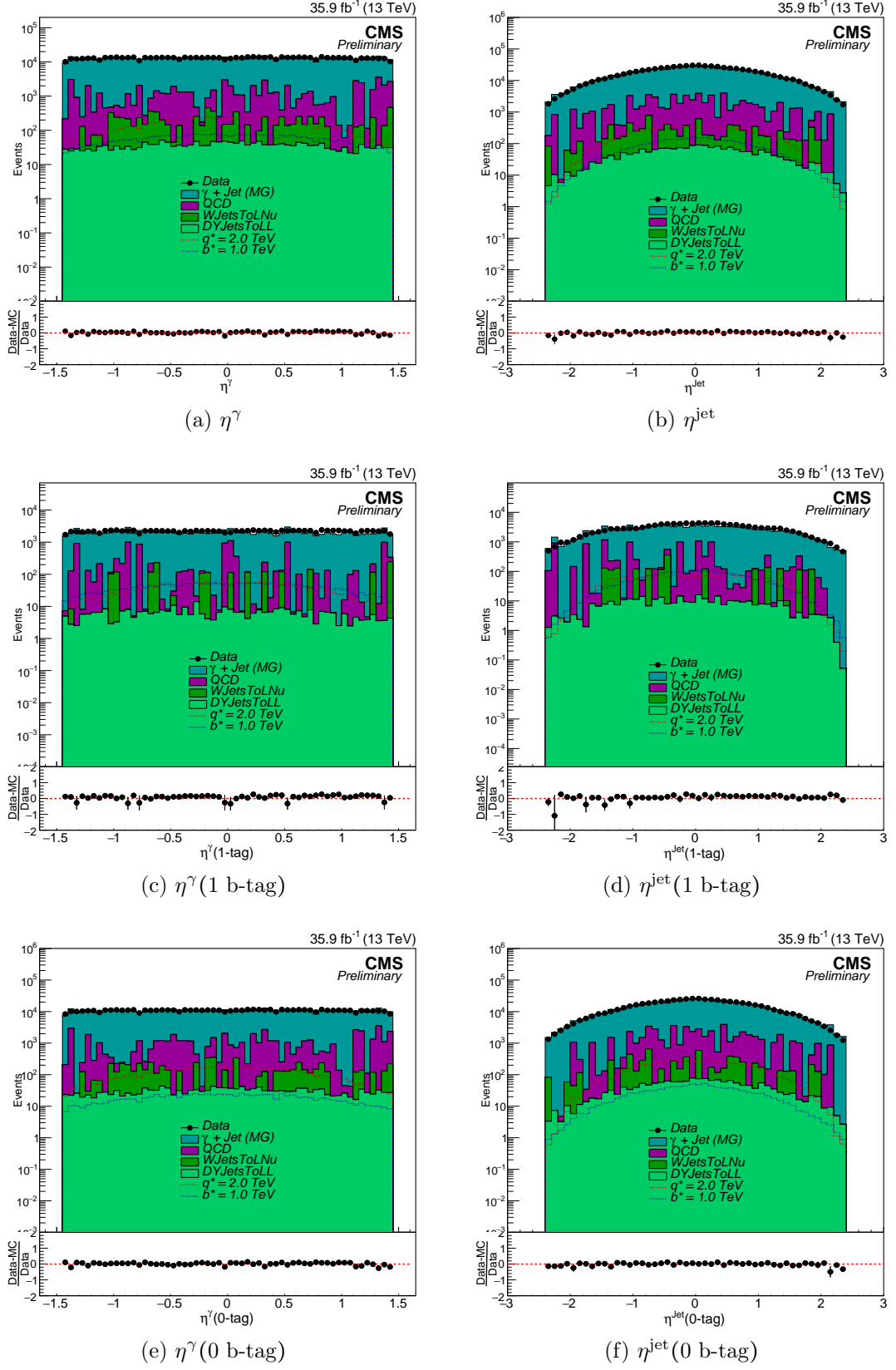


Figure 4.17: Data-MC comparison of  $\eta$  distribution of photons and jets for three categories: no b-tag, 1 b-tag and 0 b-tag.

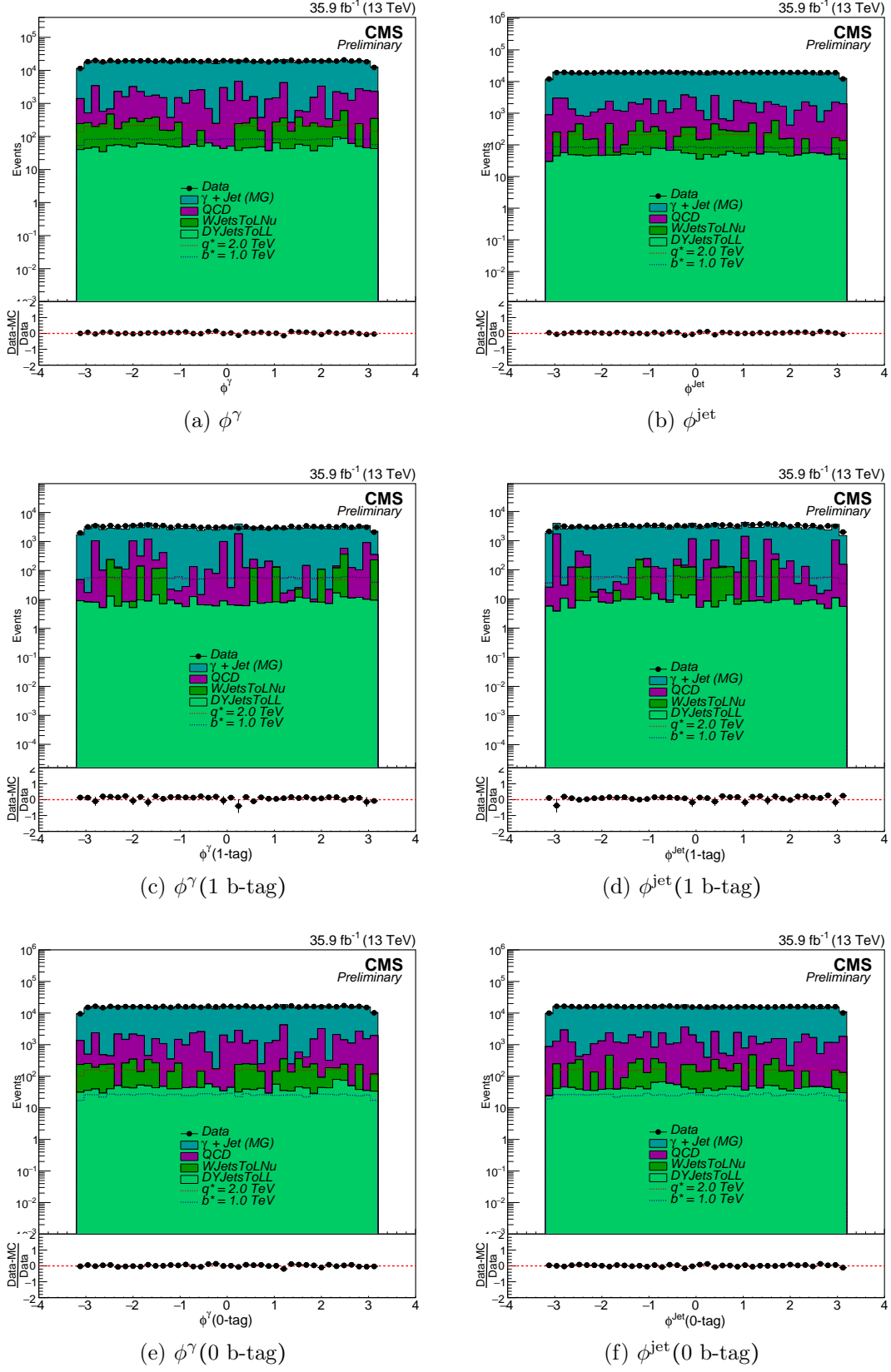


Figure 4.18: Data-MC comparison of  $\phi$  distribution of photons and jets for three categories: no b-tag, 1 b-tag and 0 b-tag.

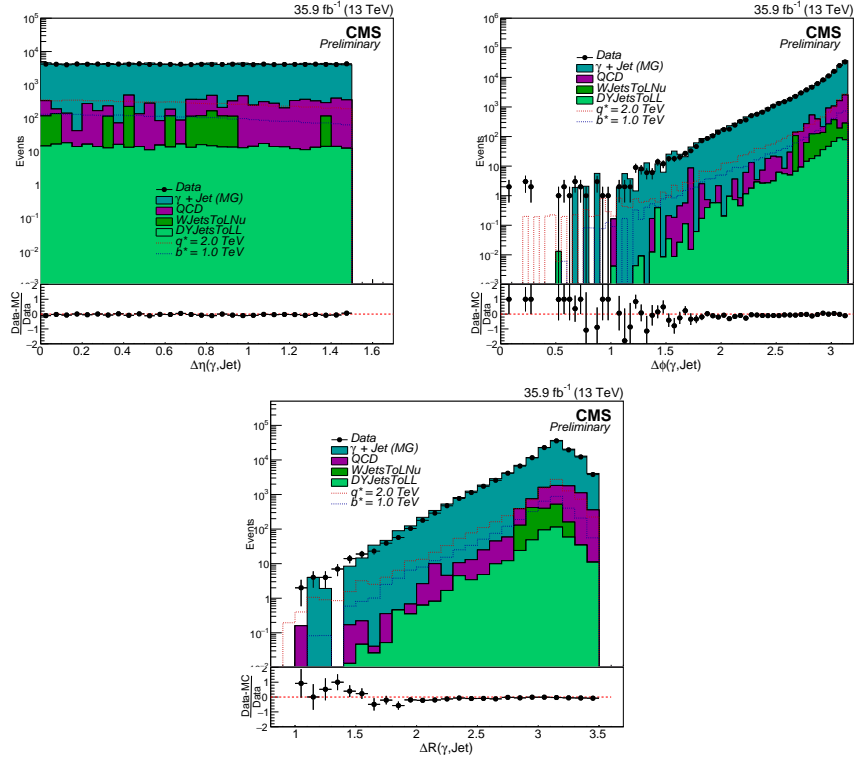


Figure 4.19: Distributions of photons and jets in  $\Delta\eta$  (above left),  $\Delta\phi$  (above right), and  $\Delta R$  (below).

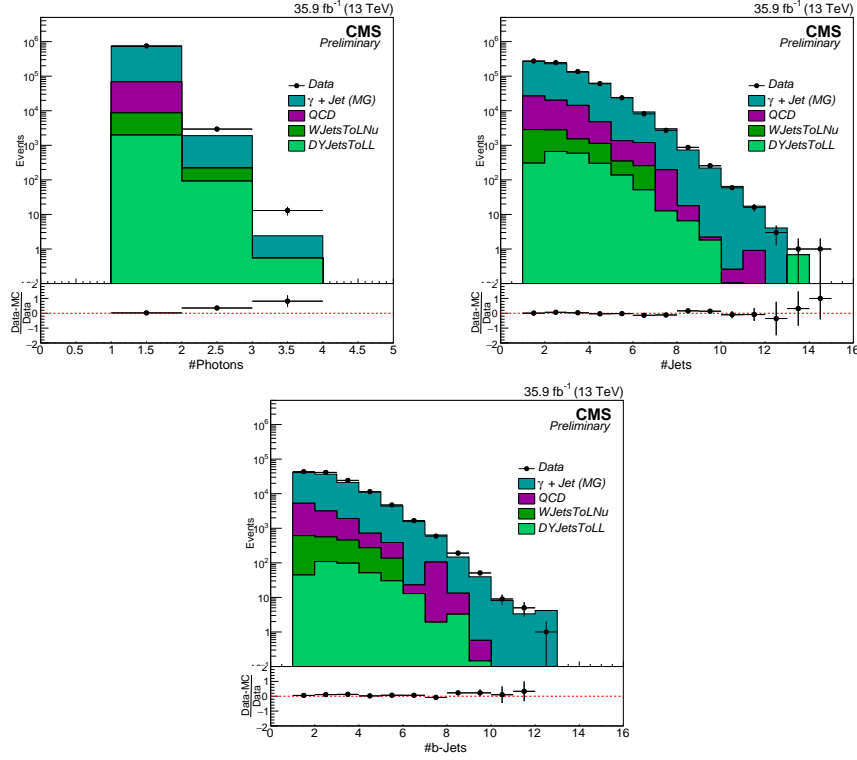


Figure 4.20: Number of photons (above left), jets (above right), and b-jets (below) per event in Data-MC.

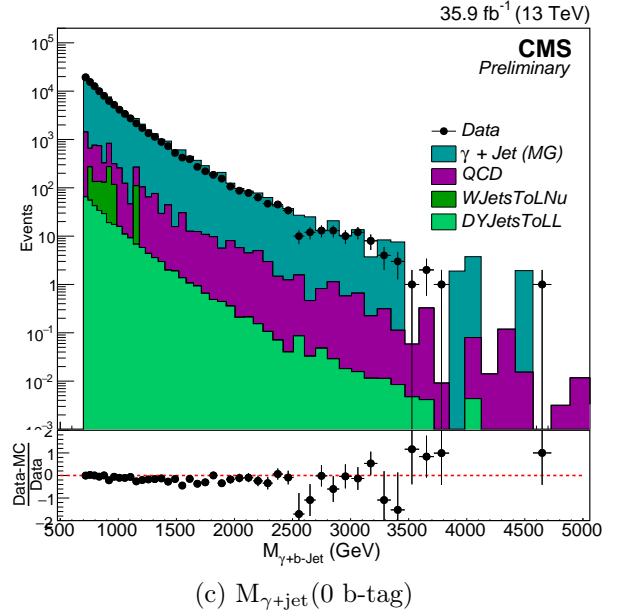
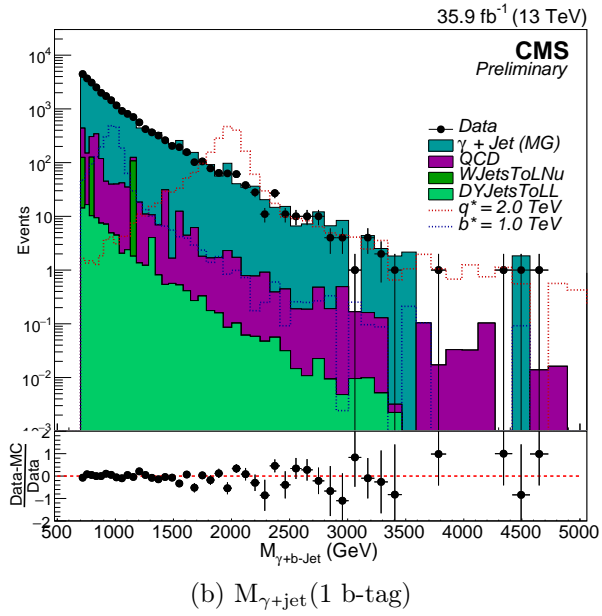
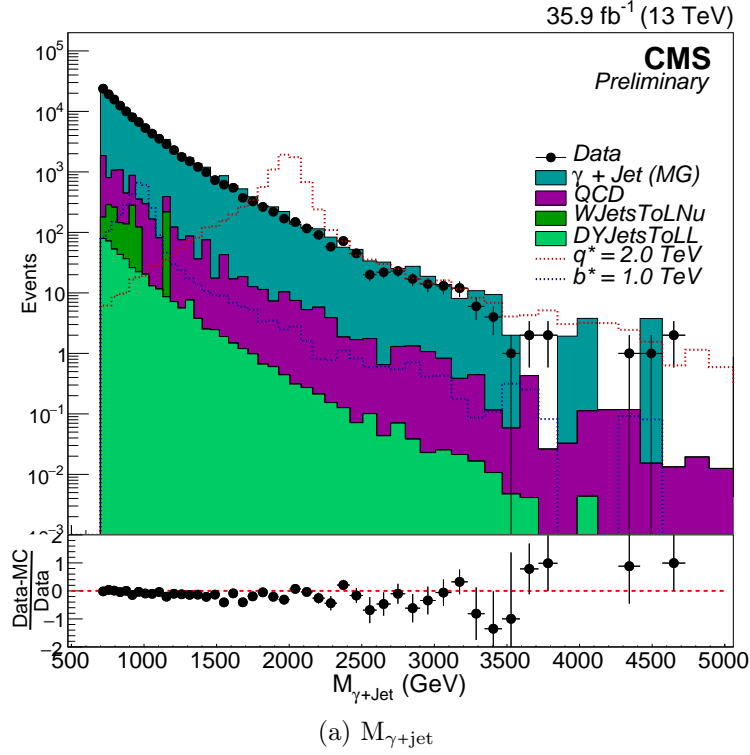
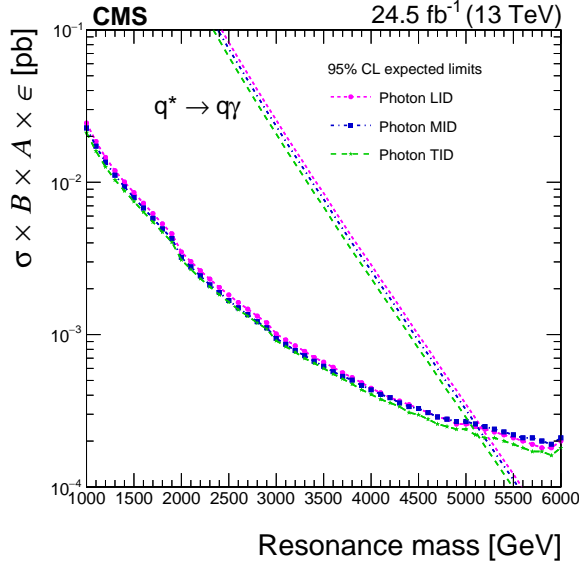


Figure 4.21: Data-MC comparison of invariant mass distribution of  $\gamma + \text{jet}$  in three categories: no b-tag, 1 b-tag and 0 b-tag.

#### 4.4.8 Optimization of event selection

The event selection considered in this analysis has been optimized for best expected mass limits on  $q^*$  and  $b^*$  resonances (the procedure to obtain expected limits is explained in the upcoming Section 4.10). The expected background obtained from the Poisson fluctuation of total background MC has been used in evaluating limits. The standard selection used for optimization study is “loose” photon ID, “tight” jet ID,  $\Delta\eta < 1.8$ ,  $\Delta\phi > 1.5$  and “medium” CSVv2 cut.

For different photon ID working points (WP), the expected limits at 95% CL are presented in Fig. 4.22 and Table 4.10. The optimization study tells that the “loose” WP is the most efficient one. However, it has been found that the trigger efficiency w.r.t muon reference trigger improves on going from loose to medium WP, therefore, “medium” WP for photon ID has been chosen.



Photon ID	Exp. mass limit (TeV)
loose	5.17
medium	5.11
tight	5.13

Table 4.10: Photon ID cut optimization corresponding to different mass expected limits.

Figure 4.22: Expected 95% CL upper limits on  $\sigma \times BR \times A \times \epsilon$  versus  $q^*$  mass for different photon ID cuts corresponding to SM coupling  $f = 1.0$ .

The optimization studies for different  $\Delta\eta$  cuts is presented in Fig. 4.23 and Table 4.11 and a  $\Delta\eta(\gamma, \text{jet})$  cut of 1.5 is found to be the most efficient. One more advantage of a  $\Delta\eta(\gamma, \text{jet})$  cut is that it helps in achieving mass turn-on at a lower mass point (as shown in Fig. 4.14) compared to no  $\Delta\eta$  cut.

The corresponding optimization results for various  $\Delta\phi$  cuts are presented in

Fig. 4.24 and Table 4.12 while for various CSVv2 cuts, it is presented in Fig. 4.25 and Table 4.13. A selection without any  $\Delta\phi$  cut and a “loose” CSVv2 cut is found optimum.

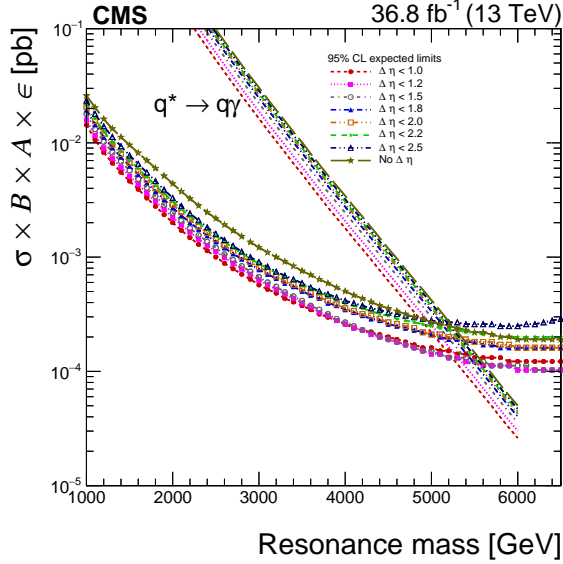


Figure 4.23: Expected 95% CL upper limits on  $\sigma \times \text{BR} \times A \times \epsilon$  versus  $q^*$  mass for different  $\Delta\eta$  cuts corresponding to SM coupling  $f = 1.0$ .

$\Delta\eta$ cuts	Exp. mass limit (TeV)
$\Delta\eta < 1.0$	5.17
$\Delta\eta < 1.2$	5.31
$\Delta\eta < 1.5$	5.39
$\Delta\eta < 1.8$	5.27
$\Delta\eta < 2.0$	5.28
$\Delta\eta < 2.2$	5.24
$\Delta\eta < 2.5$	5.19
No $\Delta\eta$	5.26

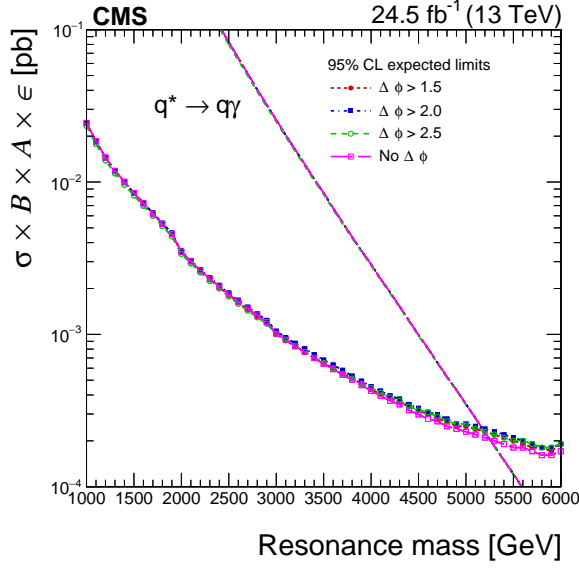
Table 4.11:  $\Delta\eta$  cut optimization corresponding to different mass expected limits.

## 4.5 Highest invariant mass events in data

The event with highest invariant mass is observed in data at  $M_{\gamma+\text{jet}} = 4616.69 \text{ GeV}$ . The event display for this event has been made using the cmsShow [184] package in different detector orientations and is presented in Fig. 4.26. The photon candidate in this event is found to have a  $p_T = 1253 \text{ GeV}$  and  $\eta = -0.857733$  while the jet candidate has a  $p_T = 3022.47 \text{ GeV}$  and  $\eta = 0.395303$ . The jet candidate is tagged as a b-jet, therefore, this event form the highest  $q^*$  as well as the highest  $b^*$  invariant mass event. This event was recorded by the CMS detector on 29<sup>th</sup> August, 2016 in the run number 279716.

The event with 2<sup>nd</sup> highest invariant mass is observed at  $M_{\gamma+\text{jet}} = 4595.43 \text{ GeV}$  with the photon candidate having  $p_T = 1872.51 \text{ GeV}$ ,  $\eta = 0.927873$  and the jet candidate having  $p_T = 1945.66 \text{ GeV}$ ,  $\eta = -0.299033$ . Since the jet is not tagged as a b-jet, so this event form the part of  $q^*$  statistics only. The event display for this event is presented in Fig. 4.27.

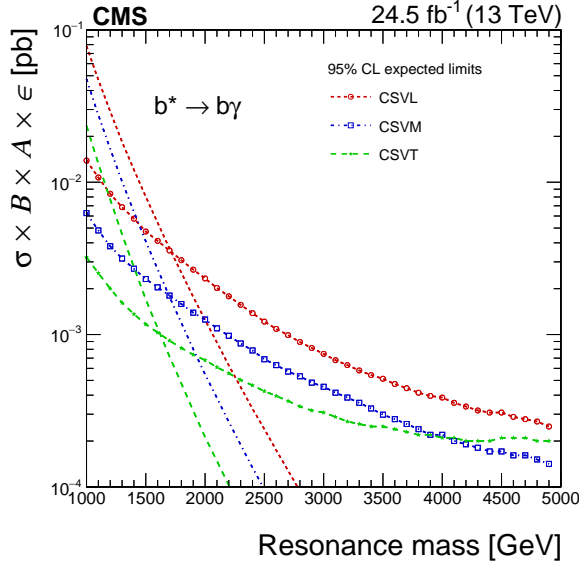




$\Delta\phi$ cuts	Exp. mass limit (TeV)
$\Delta\phi > 1.5$	5.19
$\Delta\phi > 2.0$	5.17
$\Delta\phi > 2.5$	5.18
No $\Delta\phi$	5.24

Table 4.12:  $\Delta\phi$  cut optimization corresponding to different mass expected limits.

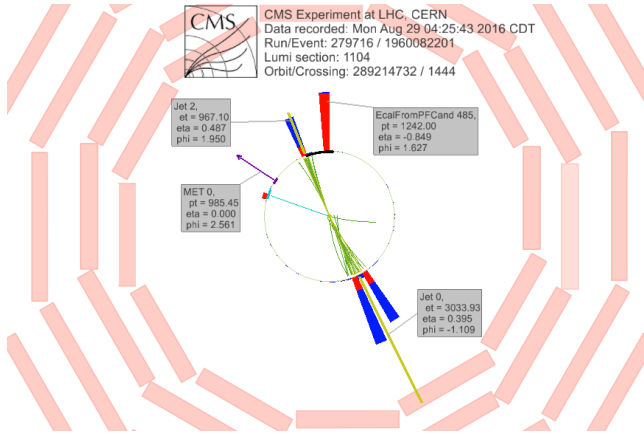
Figure 4.24: Expected 95% CL upper limits on  $\sigma \times \text{BR} \times A \times \epsilon$  versus  $q^*$  mass for different  $\Delta\phi$  cuts corresponding to SM coupling  $f = 1.0$ .



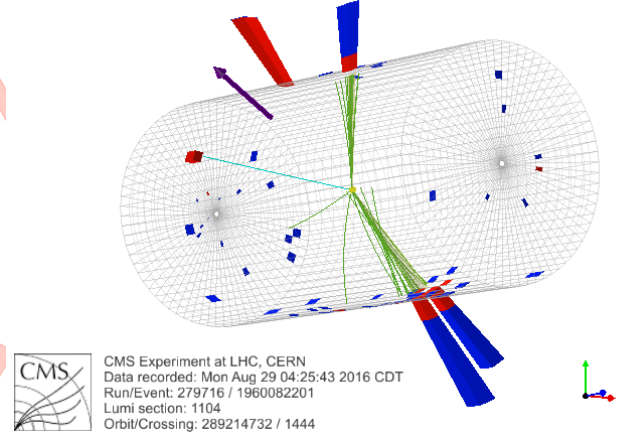
CSVv2	Exp. mass limit (TeV)
loose	1.73
medium	1.70
tight	1.50

Table 4.13: CSVv2 cut optimization corresponding to different mass expected limits.

Figure 4.25: Expected 95% CL upper limits on  $\sigma \times \text{BR} \times A \times \epsilon$  versus  $q^*$  mass for different CSVv2 cuts corresponding to SM coupling  $f = 1.0$ .

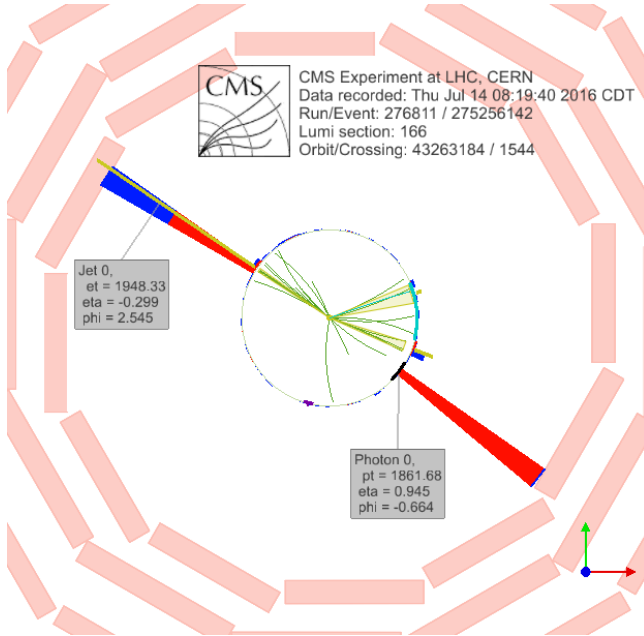


(a)  $\rho$ - $\phi$  plane

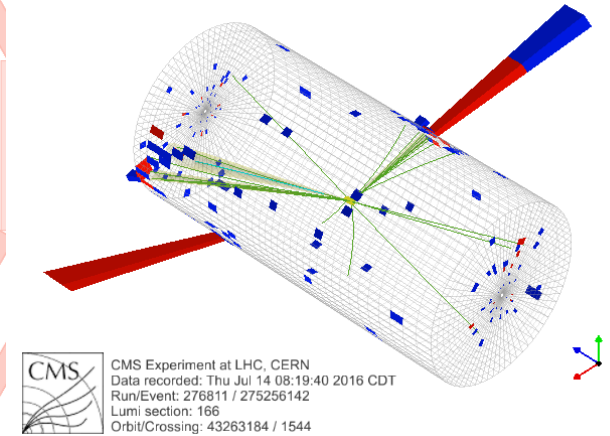


(b) 3-dimensional plane

Figure 4.26: Event display for the highest invariant mass event at  $M_{\gamma+jet} = 4616.69 \text{ GeV}$ . This event has the jet tagged as a b-jet, thereby, forming a highest  $q^*$  as well as highest  $b^*$  event.



(a)  $\rho$ - $\phi$  plane



(b) 3-dimensional plane

Figure 4.27: Event display for the 2<sup>nd</sup> highest invariant mass event at  $M_{\gamma+jet} = 4595.43 \text{ GeV}$ .

## 4.6 Signal spectrum

The  $\gamma$  + jet/b-jet invariant mass distribution spectrum falls steeply with increasing mass. The  $q^*$  and  $b^*$  signals, if exist, will appear as narrow resonances over the continuous spectrum. In order to observe these narrow resonances, the bin widths of invariant mass distributions should match with the mass resolutions of the  $q^*$  and  $b^*$  resonances. Since the resonance width and hence the mass resolution is directly proportional to the resonance mass, it increases with increase of resonance mass. So the invariant mass spectra are required to have a variable binning with increasing bin widths.

To obtain variable binning, the signal shape at different masses are fitted with three different functions, viz. Gaussian, Breit-Wigner and Crystal-Ball (CB), as shown in Fig. 4.28 for some of  $q^*$  mass points. This is required to retrieve the mass resolutions. The Crystal-Ball function is found to best describe the shapes and its functional form is given by,

$$CB(x; \alpha, n, \mu, \sigma) = N_{CB} \cdot \begin{cases} \exp\left(-\frac{(x-\mu)^2}{2\sigma^2}\right), & \text{for } \frac{x-\mu}{\sigma} > -\alpha \\ \left(\frac{n}{|\alpha|}\right)^n \cdot \exp\left(-\frac{|\alpha|^2}{2}\right) \cdot \left(\frac{n}{|\alpha|} - |\alpha| - \frac{x-\mu}{\sigma}\right)^{-n}, & \text{for } \frac{x-\mu}{\sigma} \leq -\alpha, \end{cases} \quad (4.3)$$

where  $N_{CB}$  is the normalization factor,  $\sigma$  is the width,  $\mu$  is the mean and  $\alpha, n$  are the parameters determining the functional fitting. The resonance widths and means obtained from CB fitting are then used in a functional form,

$$\frac{\sigma}{\text{Mean}} = A + \frac{B}{M_{\text{Res}}} \quad (4.4)$$

where  $\frac{\sigma}{\text{Mean}}$  is known as the mass resolution with  $\sigma$ , the resonance width and Mean, the resonance mean obtained upon fitting and  $M_{\text{Res}}$  is the resonance mass. This functional form is plotted between  $\frac{\sigma}{\text{Mean}}$  and  $M_{\text{Res}}$  for different masses and fitted to obtain the values of parameters A and B as shown in Fig. 4.29. These parameters are then used to obtain variable mass binning for  $q^*$  and  $b^*$  invariant mass distributions and is presented below:

```
nMassBin[120] = { 1, 3, 6, 10, 16, 23, 31, 40, 50, 61, 73, 86, 100, 115, 132, 150, 169,
                  189, 210, 232, 252, 273, 295, 318, 341, 365, 390, 416, 443, 471, 500,
                  530, 561, 593, 626, 660, 700, 731, 768, 806, 846, 887, 929, 972, 1017,
                  1063, 1110, 1159, 1209, 1261, 1315, 1370, 1427, 1486, 1547, 1609, 1673,
                  1739, 1807, 1877, 1950, 2025, 2102, 2182, 2264, 2349, 2436, 2526, 2619,
                  2714, 2812, 2913, 3018, 3126, 3237, 3352, 3470, 3592, 3718, 3847, 3980,
```

4117, 4259, 4405, 4556, 4711, 4871, 5036, 5206, 5381, 5562, 5748, 5940,  
6138, 6342, 6552, 6769, 6993, 7223, 7461, 7706, 7959, 8219, 8487, 8764,  
9049, 9343, 9646, 9958, 10280, 10612, 10954, 11307, 11671, 12046, 12432,  
12830, 13241, 13664, 14000};

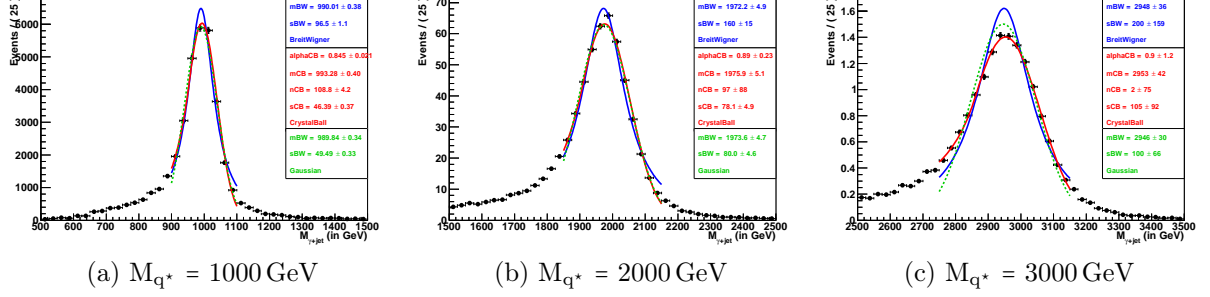


Figure 4.28: Fitting the core of invariant mass of  $q^*$  signal at different masses for  $f = 1.0$ , using Breit-Wigner (Blue), Crystal-Ball (Red), and Gaussian (Green) functions to obtain the resonance width of the signal.

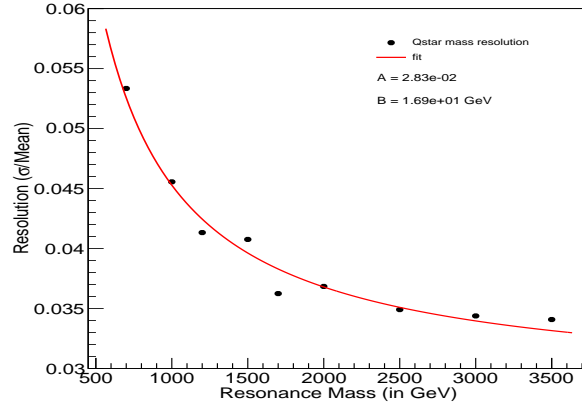


Figure 4.29: Polynomial fitting of mass resolution vs. resonance mass to obtain variable binning parameters.

## 4.7 Signal interpolation

While searching for new particles, with unknown masses, it is essential to scan the entire possible mass range. Due to limitation of resources, only a limited number of signal masses over a large range are generated. For  $q^*$  ( $b^*$ ) resonances, only 10 mass points per coupling multiplier are generated in the mass range from 0.5–9.0 TeV (0.5–5.0 TeV). The signal shapes at intermediate masses are obtained by using an interpolation technique [185] which utilizes the information from neighbouring generated masses.

In order to interpolate a signal shape at an intermediate mass  $M$  between two generated masses  $M_A$  and  $M_B$  using this technique, a probability distribution in a parameter  $X$  is constructed which is defined as  $\text{Prob.}(X) = \frac{M_{\gamma+\text{jet}}}{M_{\text{Res}}}$ , where  $M_{\text{Res}}$  is the resonance mass and  $M_{\gamma+\text{jet}}$  is the invariant mass distribution at the resonance mass. This distribution for masses  $M_A$  and  $M_B$  are obtained and used to get the  $\text{Prob.}(X)$  distribution for mass  $M$  using the relation,

$$\text{Prob}_M(X) = \text{Prob}_{M_A}(X) + [\text{Prob}_{M_B}(X) - \text{Prob}_{M_A}(X)] \cdot \frac{M - M_A}{M_B - M_A} \quad (4.5)$$

The  $X$ -distribution is then converted back to  $\gamma + \text{jet}$  mass distribution using the `ROOT::Math::Interpolator [134]` class to get the resonance shape at the interpolated resonance mass. The generated and interpolated signal shapes for different  $q^*$  mass points are plotted alternatively for comparison in the Fig. 4.30.

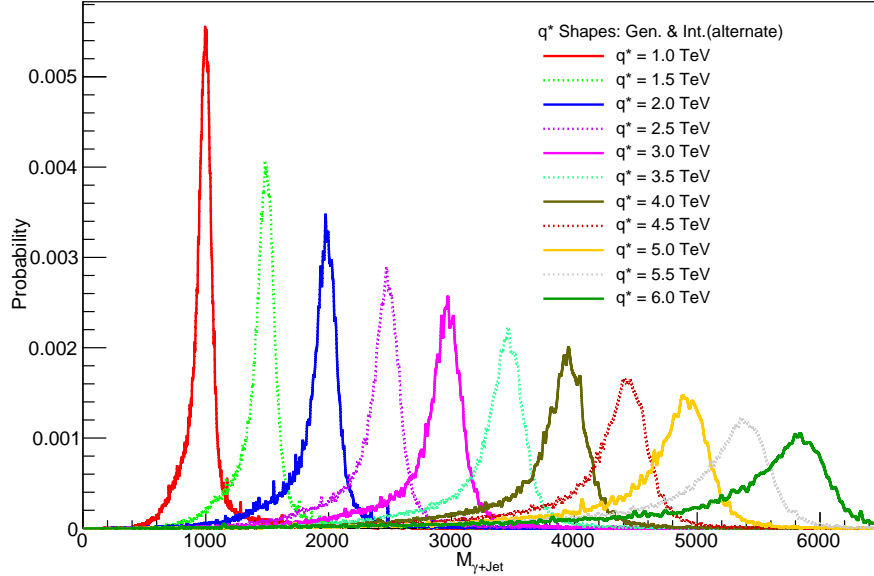


Figure 4.30: Alternate generated (solid line) and interpolated (dotted line) shapes for different  $q^*$  mass points.

The interpolation procedure has been authenticated by performing a closure test in which already generated shapes from PYTHIA are interpolated again using the immediate neighbours and a comparison is made as shown in Fig. 4.31 for three different  $q^*$  mass points. The interpolated shapes are found to be in good agreement with the generated ones. Only a small difference is observed on going towards higher masses, which is considered as a systematic uncertainty.

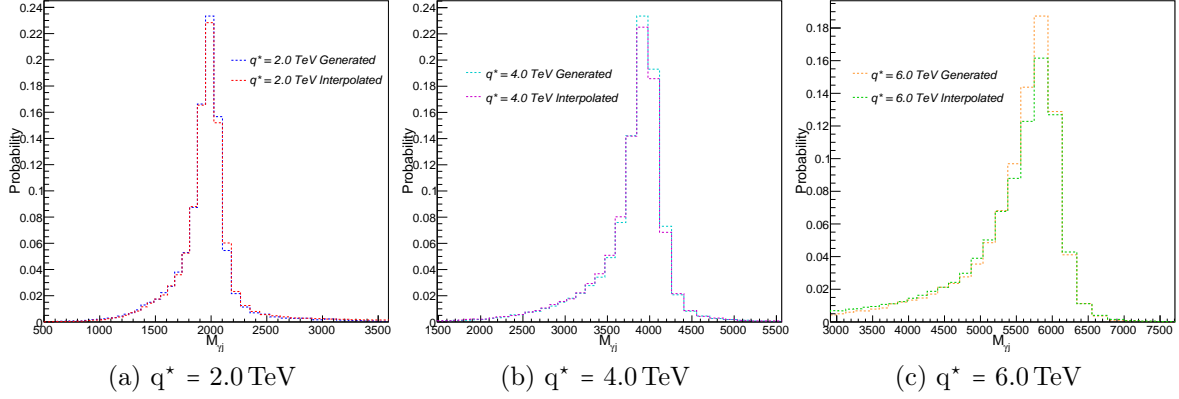


Figure 4.31: Comparison of generated and interpolated shapes at different  $q^*$  mass points.

## 4.8 Parametric background

The invariant mass distributions of  $\gamma$ +jet and  $\gamma$ +b-jet are well described by MC simulation. The binning of invariant mass distribution is chosen to have a bin width almost equal to the expected  $q^*$  and  $b^*$  mass resolutions, that varies from about 4.5% at 1 TeV to 3.3% at 6 TeV. However, in order to model the background of this study, a data driven method using a smooth parameterization has been considered. The usage of a fit function is advantageous over MC simulation in background modelling as MC simulation has many theoretical (like PDFs, renormalization scale etc.) and experimental (like jet energy scale, energy resolutions etc.) uncertainties associated with it. The methodology of smooth parameterization is considered because the background due to  $\gamma$  + jet processes is smooth and monotonically falling and can be extracted by fitting the distribution with a smooth polynomial function.

Several functional forms inspired from previous similar searches [186–191] have been considered, which are listed below:

$$1. F_1 = \frac{P_0(1-x)^{P_1}}{x^{P_2+P_3} \ln x}$$

$$2. F_2 = \frac{P_0(1+x)^{P_1}}{x^{P_2+P_3} \ln x}$$

$$3. F_3 = \frac{P_0}{(P_1+P_2 \cdot x+x^2)^{P_3}}$$

$$4. F_4 = \frac{P_0}{(P_1+x)^{P_2}}$$

$$5. F_5 = P_0 \cdot \exp(1 + P_1 \cdot x + P_2 x^2 + P_3 x^3)$$

where  $x = m/\sqrt{s}$ ,  $m$  being the  $\gamma$  + jet invariant mass and  $\sqrt{s}$  being the center of mass energy,  $P_0$ ,  $P_1$ ,  $P_2$  and  $P_3$  are the fit parameters.

#### 4.8.1 Fisher test

The order of the various functions for  $q^*$  and  $b^*$  scenarios has been chosen on the basis of the Fisher-test. This test is used to determine whether for two fit models, 1 and 2, where model 1 with  $p_1$  parameters is “nested” within model 2 with  $p_2$  parameters ( $p_2 > p_1$ ), the model 1 provide *significantly* better fit to data compared to model 2.

A F-test is any statistical test which has the test statistic distributed according to the F-distribution under the null hypothesis. We use the saturated model goodness-of-fit test statistics [192, 193]:

$$-2 \log \lambda = 2 \sum_j^{n_{\text{bins}}} = (b_j - x_j + x_j \log(x_j/b_j)) \quad (4.6)$$

where  $x_j$  is the number of data events in the  $j^{\text{th}}$  bin and  $b_j$  is the prediction in the  $j^{\text{th}}$  bin. This test statistic asymptotically follows a  $\chi^2$ -distribution with  $(n_{\text{bins}} - p_i)$  degrees of freedom,  $p_i$  being the number of parameters for model  $i$ . This statistic forms an appropriate metric for the goodness-of-fit of maximum likelihood fits using a Poissonian likelihood. Based on this, a F-statistics has been constructed as

$$F = \frac{-2 \log(\lambda_1/\lambda_2)/(p_2 - p_1)}{-2 \log \lambda_2/(n_{\text{bins}} - p_2)}, \quad (4.7)$$

where  $n_{\text{bins}}$  is the number of bins and  $-2 \log \lambda_i$  is the “saturated model” goodness-of-fit test statistic for model  $i$ .

The null hypothesis states that the model 2 does not provide a significantly better fit compared to model 1 and under this hypothesis,  $F$  will have a F-distribution with  $(p_2 - p_1, p_2 - n)$  degrees of freedom. The null hypothesis will be rejected if the  $F$  computed from data is greater than the critical value of F-distribution for the false rejection probability of  $\alpha = 0.05$ .

To perform this test, the pseudo invariant mass distribution from background MC has been considered and fitted using the same function with  $p_1$  and  $p_2$  parameters, where  $p_2 > p_1$ , to obtain the best-fit parameters. Based on the fitting, the  $\chi^2$  test statistics (eq. 4.6) for each set of parameters is constructed and a

$F$ -value is determined using the definition above. Now assuming that the null hypothesis is true, that is function with  $p_2$  parameters does not provide a better fit compared to function with  $p_1$  parameters, toys are generated using fit results corresponding to the function with  $p_1$  parameters. A  $F$ -value is computed for each toy and a F-distribution is constructed. If the  $F$ -value obtained from initial best fit parameters is found to be greater than the  $F$ -value corresponding to a p-value of 0.05, null hypothesis is rejected, otherwise accepted.

We have sequentially tested each order of different functions ( $F1 - F5$ ) and obtained the best orders (as listed above) for which a  $F$ -value corresponding to a p-value  $> 0.05$  is obtained. The F-distributions for function  $F1$  corresponding to 3 and 4 parameters has been presented in Fig. 4.32 for  $q^*$  and in Fig. 4.33 for  $b^*$ . A p-value  $> 0.05$  is obtained for  $F1$  with 4 parameters in each case.

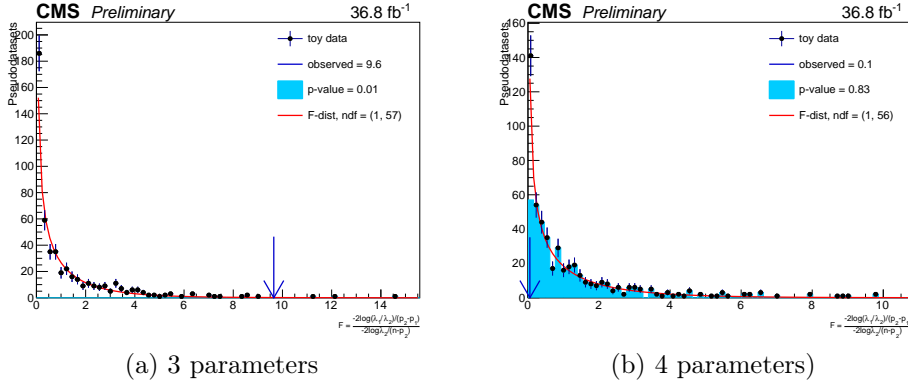


Figure 4.32: The F-test distributions for fitting of function  $F1$  with  $q^*$  invariant mass, for 3 and 4 parameters, showing that  $F1$  with 4 parameters provide a better fit compared to 3 parameters.

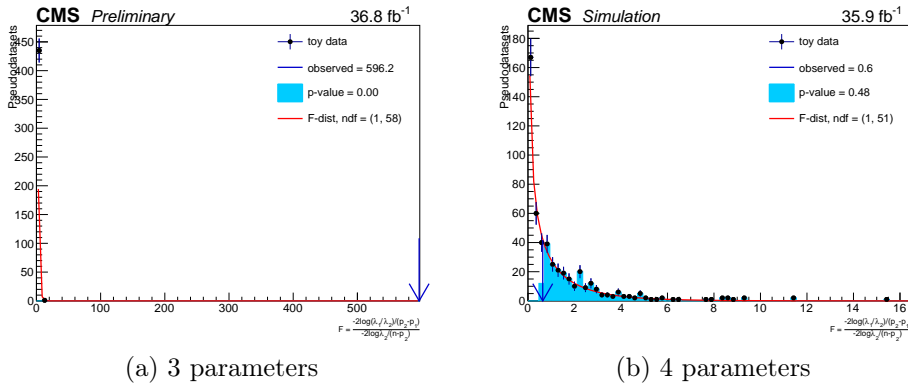


Figure 4.33: The F-test distributions for fitting of function  $F1$  with  $b^*$  invariant mass, for 3 and 4 parameters, showing that  $F1$  with 4 parameters provide a better fit compared to 3 parameters.



### 4.8.2 Goodness-of-fit

In order to test the goodness-of-fit (GOF) of different functional forms  $F1 - F5$  with data, we have used the modified  $\chi^2$  test statistics,

$$\chi^2 = \sum_{i=1}^{n_b} \left( \frac{x_i - b_i}{\sigma_{x_i}} \right)^2, \quad (4.8)$$

where the “uncertainty”  $\sigma_{x_i}$  is the 68% CL region of a Poisson distribution and is defined as follows, setting  $\alpha = 1 - 0.687$ ,

$$\sigma_{x_i} = \begin{cases} D_c^{-1}(\alpha/2, x_i + 1), & \text{if } b_i > x_i \\ D^{-1}(\alpha/2, x_i), & \text{if } b_i < x_i \end{cases} \quad (4.9)$$

where  $D^{-1}(\alpha/2, x_i)$  is the quantile function of gamma distribution, which is also the inverse of the cumulative distribution function of the lower tail of the gamma distribution,

$$D(\alpha/2, x_i) = \int_{-\infty}^{\alpha/2} \frac{1}{\Gamma(x_i)} z^{x_i-1} e^{-z} dz, \quad (4.10)$$

and,  $D_c^{-1}(\alpha/2, x_i + 1)$  is the inverse of the cumulative distribution function of the upper tail of the gamma distribution,

$$D_c(\alpha/2, x_i + 1) = \int_{\alpha/2}^{+\infty} \frac{1}{\Gamma(x_i + 1)} z^{x_i} e^{-z} dz. \quad (4.11)$$

We generated around 1000 pseudo datasets using the best-fit model parameters on data, refit each pseudo dataset with the maximum likelihood fit and save the test statistic value. The distribution of the test statistics from these pseudo datasets as well as the value observed in data for different functions  $F1 - F5$  is presented in Fig. 4.34 for  $q^*$  and in Fig. 4.35 for  $b^*$ . The  $\chi^2/\text{ndf}$  values for different functions is also reported.

Since almost all the functions provide reasonable fit to data, one of the functions,  $F1$  has been chosen as the background parameterization for this study, written as

$$\frac{d\sigma}{dm} = \frac{P_0(1 - m/\sqrt{s})^{P_1}}{(m/\sqrt{s})^{P_2+P_3 \ln(m/\sqrt{s})}}. \quad (4.12)$$

This parameterization is motivated by the LO QCD. The term  $x^{P_2}$  (or  $m^{P_2}$ ) in the denominator refers to the mass dependence of the QCD matrix element while

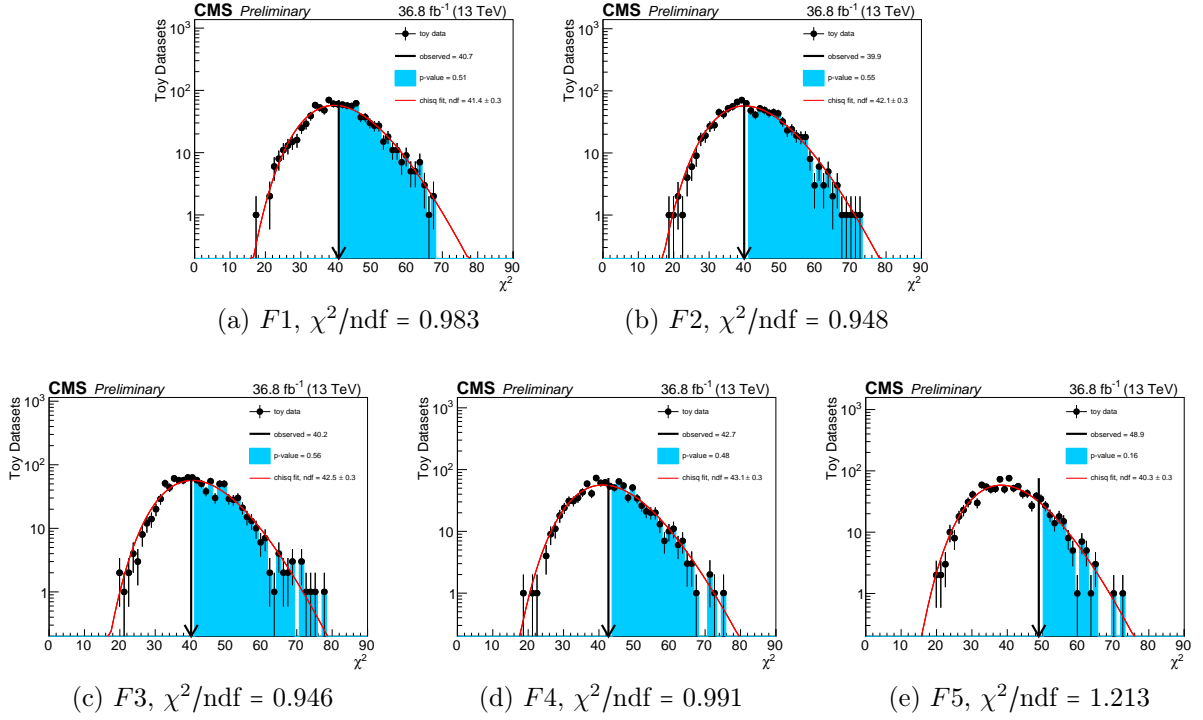


Figure 4.34: Toy distributions for the goodness-of-fit study for  $q^*$ .

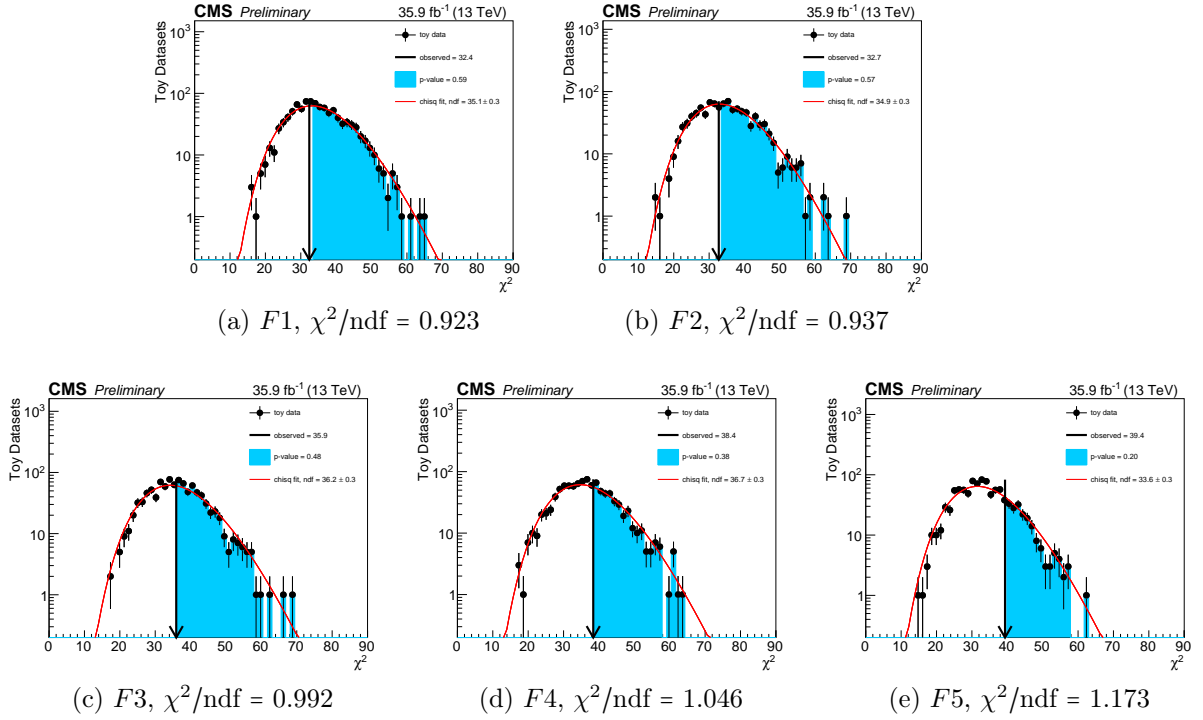


Figure 4.35: Toy distributions for the goodness-of-fit study for  $b^*$ .

the term  $(1 - x)^{P_1}$  in the numerator refers to the mass dependence of the parton distributions, the term  $P_3$  models the data at higher invariant masses.

We have performed an extended, background-only, binned, maximum-likelihood fit to the data by using the following likelihood,

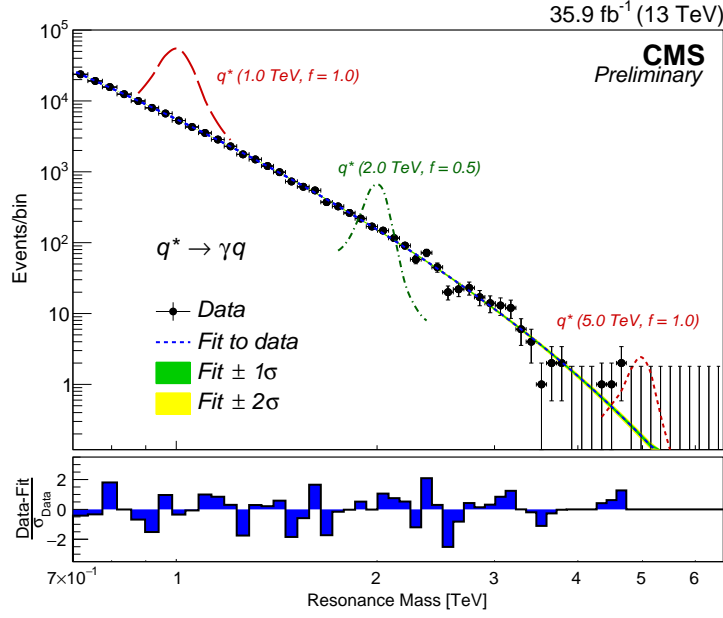
$$\mathcal{L}(\text{data}|\theta) = \prod_{i=1}^{n_b} \text{Poisson}(x_i|b_i(\theta)) = \prod_{i=1}^{n_b} \frac{b_i(\theta)^{x_i} e^{-b_i(\theta)}}{x_i!} \quad (4.13)$$

where  $n_b$  corresponds to the number of bins,  $\theta$  is the vector of nuisance parameters  $(P_0, P_1, P_2, P_3)$  (or, equivalently  $(N_b, P_1, P_2, P_3)$ ),  $x_i$  is the data yield in the  $i^{\text{th}}$  bin, and  $b_i$  is the integral of the fit function in  $i^{\text{th}}$  bin multiplied by the expected events  $N_b$ . The result of the background only fit to the data for  $q^*$  and  $b^*$  in three categories is presented in Fig. 4.36.

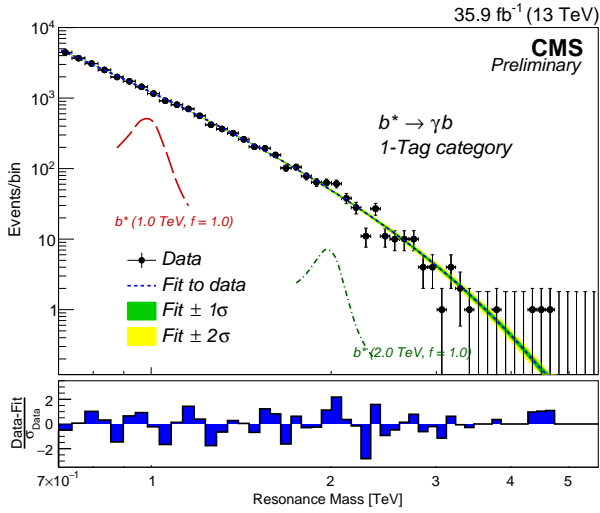
### 4.8.3 Bias due to the choice of background fit function

The background fit function defined in Eq. 4.12 has been considered to model the  $\gamma + \text{jet}$  and  $\gamma + \text{b-jet}$  invariant mass distributions. However, the uncertainties associated with the choice of a particular fit function can impact the final result. Therefore, a bias study has been performed to quantify the amount of potential bias that can be present given a certain choice of functional form. In this study, the function  $F1$  is taken as the default function while the functions  $F2 - F5$  are taken as the alternate functions. The procedure implemented to study the bias is described as follows:

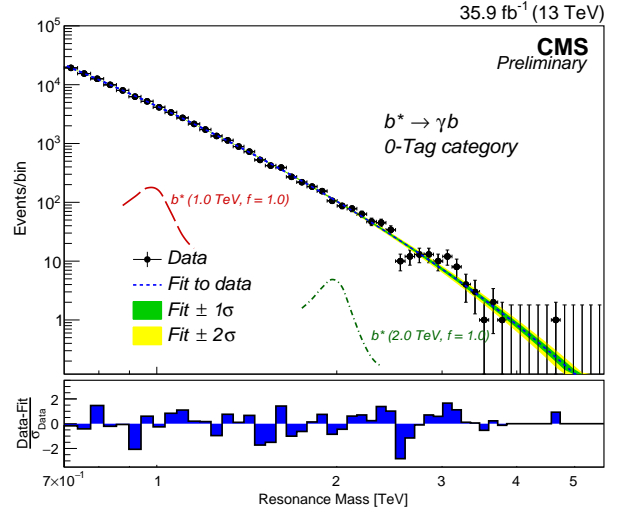
- An underlying distribution  $h(m_{\gamma+\text{jet}})$  in the  $\gamma + \text{jet}$  (and  $\gamma + \text{b-jet}$ ) invariant mass distribution is obtained using the total MC background.
- S+B fit to  $h(m_{\gamma+\text{jet}})$  with an input signal of mass  $m$  and signal strength  $\mu = 1$  is performed using the test functions  $F2 - F5$  to get the best fit parameters.
- These best fit parameters are then used to generate  $N$  number of toys corresponding to each function.
- The toys associated with each test function are then fitted with the default background function  $F1$  and strength of the signal is predicted for each toy using maximum likelihood approach, resulting into a distribution  $\hat{f}_i(m_{\gamma+\text{jet}})$ ,  $i = 2, 3, 4, 5$ , of  $\mu_i$
- The signal strength  $\hat{\mu}_i$  predicted by  $\hat{f}_i(m_{\gamma+\text{jet}})$  is compared with input signal



(a)  $M_{\gamma+\text{jet}}$



(b)  $M_{\gamma+\text{jet}}$  (1 b-tag)



(c)  $M_{\gamma+\text{jet}}$  (0 b-tag)

Figure 4.36: Invariant mass distribution spectrum of  $\gamma$ +jet fitted with 4-parameter polynomial fit function for three categories: (a) no b-tag (b) 1 b-tag and (c) 0 b-tag.

strength  $\mu = 1$  in several mass windows  $m_j$  and a pull test statistics is constructed as:

$$p_i^j = \frac{\hat{\mu}_i^j - \mu}{\sigma_{\mu_i^j}} \quad (4.14)$$

- This pull distribution obtained for functions  $F2 - F5$  for different masses are fitted with Gaussian to obtain the predicted value of  $\mu$ .
- For the ideal case, the pull distribution should be a normal distribution with mean close to zero and rms close to 1. The deviation from zero is the measure of the bias introduced on choosing default function to describe the data when the true distributions are described by  $F2$  to  $F5$ .

A background parameterization is considered to be acceptable if for different mass regions  $m_j$ , the following relation holds:

$$b^j = |\text{median}(p_i^j)| < 0.5, \quad (4.15)$$

where  $p_i^j$  is the Gaussian mean for  $i^{\text{th}}$  toy and  $j^{\text{th}}$  mass point. The bias is considered as negligible if for each mass point, the median of all the toys is found to be within 0.5. Fig. 4.37 shows that the above relation holds for all the four test functions corresponding to  $q^*$  and  $b^*$  scenarios. The observed maximum bias is found to be less than or close to 50%.

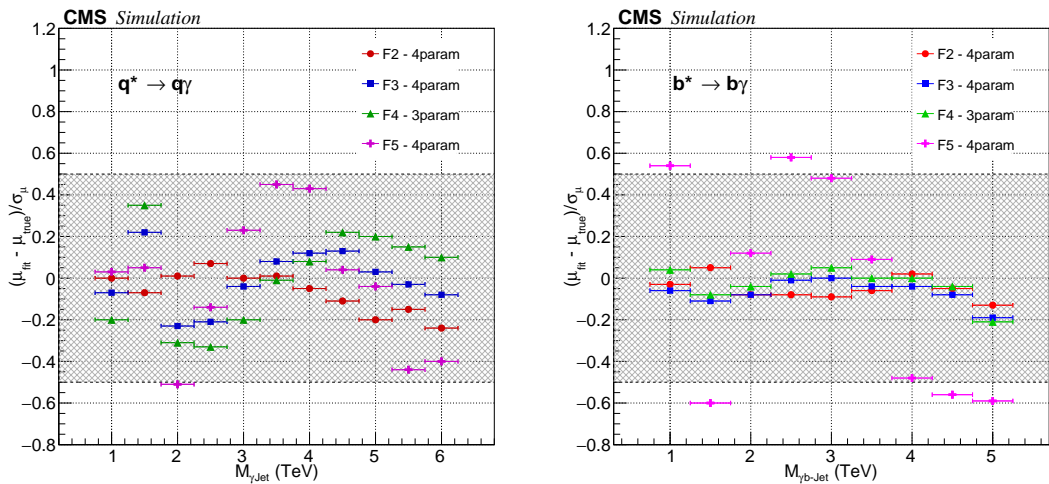


Figure 4.37: Pulls distribution as a function of  $q^*$  (left) and  $b^*$  (right) mass corresponding to the four test functions.

The pull distributions for  $q^*$  and  $b^*$  modelling are thus found to be consistent with a normal distribution with medians deviating by no more than 0.5 from zero and widths consistent with unity. If added in quadrature with the statistical uncertainty, the contribution of bias uncertainty is found to be only 10% of the total. Therefore, it has been concluded that the systematic uncertainty associated with the choice of background fit function is negligible and the statistical uncertainty of the fit is the only uncertainty that need to be considered.

## 4.9 Systematic Uncertainties

A number of systematic uncertainties due to the various sources, like, object identification, energy scales, luminosity measurements etc., are associated with this analysis. This section summarizes the most significant of these, as listed below:

- Luminosity
- Pile-up uncertainty
- HLT trigger inefficiency
- Photon and jet energy scale
- Photon and jet energy resolution
- Photon Id inefficiency
- b-tag scale factor
- Signal shape interpolation
- Background shape

The background shape uncertainty is considered for the background, the rest are considered for signal shapes only.

### 4.9.1 Luminosity

The uncertainty on the total integrated luminosity is provided centrally by CMS and is taken to be 2.5%.

### 4.9.2 Pile-up Uncertainty

The uncertainty associated with the modelling of pile-up is estimated by performing a variation of  $\pm 5\%$  in the number of interactions while using a central

value of total inelastic cross-section to be 69 mb. Effect of pileup uncertainty on  $A \times \epsilon$  of signal samples is found to  $\sim 1 - 2\%$ .

### 4.9.3 HLT trigger inefficiency

The trigger turn-on w.r.t the muon reference trigger is found to be around 95% efficient and hence an uncertainty of 5% has been assigned to this effect.

### 4.9.4 Photon and jet energy scale

The measured energy of the particle differs from its true energy due to the non-uniformity and non-linear response of the calorimeters. This difference is corrected in the photon and jet energy scale (PES & JES) at the reconstruction level. The uncertainties associated with these corrections form the source of systematic uncertainty for this analysis. The photon [117] and jet [194] energy scale uncertainties are extracted on an event by event basis and their effects are transmitted to the invariant mass distribution of the signal, to compute the amount of systematic effect. The effect of JES and PES uncertainties on the signal mass can be seen in Fig. 4.38. The effect of JES uncertainty comes out to be around 1% while that of PES is around 0.6%.

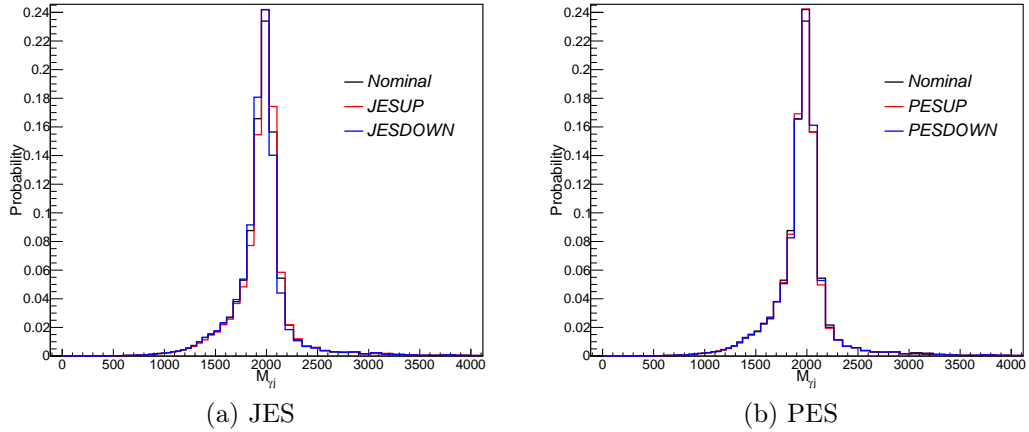


Figure 4.38: Effect of jet and photon energy correction uncertainties on the invariant mass of  $q^*$  signal.

### 4.9.5 Photon and jet energy resolution

The photon and jet energy measurements have some associated resolution which is different in data and MC and hence, can impact the energy/mass resolution

of the expected signal in data, resulting into the shrinking or stretching of the signal shape which can further impact the search. So, the resolution effect need to be taken into account in the form of a systematic uncertainty. This effect as photon [117] and jet [194] energy resolution (JER & PER) is computed and propagated to the signal invariant mass. The effect of JER and PER on signal shape is shown in Fig. 4.39 and the magnitude of both these effects is found to be around 0.2–0.4%.

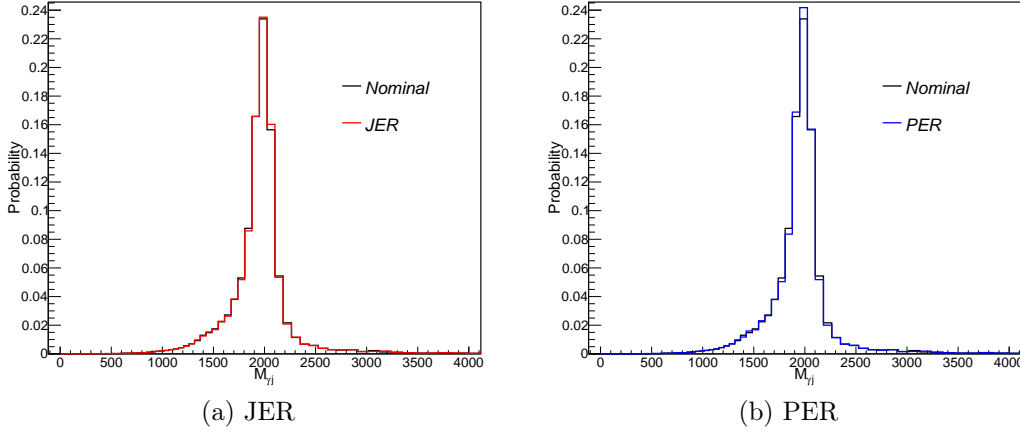


Figure 4.39: Effect of jet and photon energy resolution on the invariant mass of  $q^*$  signal.

#### 4.9.6 Photon ID inefficiency

A systematic of 2% due to photon id inefficiency has been considered in this analysis.

#### 4.9.7 b-Tag scale factor

The efficiency of b-tag discriminator is not the same in data and MC and to overcome this difference, b-tag scale factors are provided centrally in CMS. These scale factors have some associated errors which are propagated as a systematic uncertainty on the signal shape and normalization. The effect of these errors on the invariant mass spectrum of  $b^*$  signal can be seen in Fig. 4.40. The b-tag scale factors are varied up and down by the scale factor errors and the invariant mass with up and down variation are constructed, to get an estimate of the systematic effect. This effect is found to be around 2% on signal normalization and around 1% on signal shape.



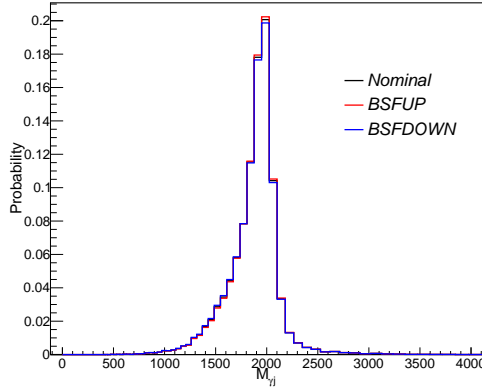


Figure 4.40: Effect of b-tag scale factor errors on the invariant mass of  $b^*$  signal.

### 4.9.8 Signal shape interpolation

The uncertainty due to the interpolation of signal shapes for intermediate masses is accounted to be around 0.5 – 1.0%.

### 4.9.9 Background Shape Uncertainty

The background shape uncertainty arises due to the difference in the shapes of data and background fit function and is evaluated in the form of uncertainty on the parameters of the analytical fit function. These parameters are considered as the nuisance parameters with uniform priors. A frequentist approach has been considered in which the systematic uncertainties related to these nuisance parameters are taken into account by maximizing the likelihood. A signal-plus-background fit to the data is initially performed to identify a reasonable starting point for the parameter values and to get an estimate of errors associated with them.

The Table 4.14 summarizes the effect of various systematic uncertainties on the signal yield.

## 4.10 Limit computation

A widely used and recommended procedure to establish discovery or exclusion in the particle physics is based on a frequentist significance test which uses a likelihood ratio as the test statistic. In CMS, this test is performed using a widely recommended and centrally adopted approach, referred to as “Higgs COMBINE Tool” [?]. In this approach, along with the parameters of interest such as the

Source	Effect on signal yield(%)
Integrated luminosity	2.5
Jet energy scale	$\sim 1$
Jet energy resolution	0.2–0.4
Photon energy scale	$\sim 0.6$
Photon energy resolution	0.2–0.4
Pileup	1–2
Photon ID efficiency	$\sim 2$
Trigger efficiency	$\sim 5$
Signal interpolation	0.5–1
PDF choice	1.5–3
b tag SF (only b*)	$\sim 1$
b tag SF normalization (only b*)	$\sim 2$

Table 4.14: Summary of the dominant sources of systematic uncertainties and their effect on the signal yield.

cross-section of the signal process, the models for signal and backgrounds also contain the nuisance parameters whose values are not considered as known a priori but either determined by fitting the data or computed by some other means. In the absence of any significant deviations in the data compared to the standard model backgrounds, the upper limit on the cross-section or lower limit on the signal mass are set.

In order to set limits, a multi-bin counting experiment likelihood which is a product of Poisson distributions corresponding to different bins, have been used:

$$\mathcal{L}(\text{data}|\mu, \theta) = \prod_{i=1}^{n_b} \text{Poisson}(x_i | s_i(\mu, \theta) + b_i(\theta)) \cdot \text{Constraint}(\theta | \bar{\theta}, \delta\theta), \quad (4.16)$$

where  $\mu$  is the resonance signal strength (also known as the parameter of interest),  $\theta$  is the vector of nuisance parameters,  $x_i$  is the data yield in the  $i^{\text{th}}$  bin,  $s_i(\mu, \theta)$  is the corresponding signal yield,  $b_i(\theta)$  is the corresponding background yield and the product runs over  $n_b$ , the number of bins. Different constraint terms are used for different type of nuisance parameters as summarized in the Table 4.15.

Using this likelihood, a test statistic as the profile likelihood ratio following the LHC Confidence Levels (CLs) procedure [195], is defined as follows:

$$\tilde{q}_\mu = -2 \log \frac{\mathcal{L}(\text{data}|\mu, \hat{\theta}_\mu)}{\mathcal{L}(\text{data}|\hat{\mu}, \hat{\theta})}, \quad 0 \leq \hat{\mu} \leq \mu, \quad (4.17)$$

where  $\hat{\theta}_\mu$  is the conditional maximum likelihood estimator of  $\theta$ , assuming that the

Systematic uncertainty	Constraint
Jet energy scale	Gaussian
Photon energy scale	Gaussian
Jet energy resolution	Gaussian
Photon energy resolution	Gaussian
b-Tag scale factors	Gaussian
Luminosity	LogNormal
Trigger	LogNormal
P <sub>0</sub>	Uniform
P <sub>1</sub>	Uniform
P <sub>2</sub>	Uniform
P <sub>3</sub>	Uniform

Table 4.15: Constraint terms associated with different systematic uncertainty nuisance parameters.

signal strength parameter  $\mu$  and the data yield  $x_i$ 's refer to the actual experimental observation or pseudo-data. The pair of parameter estimators  $\hat{\mu}$  and  $\hat{\theta}$  correspond to the global maximum of the likelihood. The lower constraint  $0 \leq \hat{\mu}$  requires the signal rate to be positive while the upper constraint  $\hat{\mu} \leq \mu$  is imposed by hand to guarantee a one-sided confidence interval.

In the frequentist paradigm, the systematic uncertainties associated with the nuisance parameters  $\theta$  are taken into account through likelihood maximization, also known as profiling. In order to derive the observed 95% confidence level upper limit on the signal strength parameter using the modified frequentist CLs method [196, 197] in the asymptotic approximation [198], we consider a value of  $\mu$  which satisfies

$$\text{CL}_s \equiv \frac{\text{CL}_{s+b}}{\text{CL}_b} = \frac{1 - \Phi(\sqrt{\tilde{q}_\mu})}{\Phi(\sqrt{\tilde{q}_{\mu,A}} - \sqrt{\tilde{q}_\mu})} = \alpha, \quad (4.18)$$

where  $\alpha = 0.05$  and  $\tilde{q}_{\mu,A}$  is the test statistic evaluated on the Asimov dataset [199] which corresponds exactly to the expected background and the nominal nuisance parameters obtained by setting all fluctuations to zero. The function  $\Phi(x)$  is the cumulative distribution function of the standard normal distribution.

A similar expression is used to derive the median expected 95% CL upper limit,

$$\Phi(\sqrt{\tilde{q}_{\mu,A}}) = 1 - 0.5\alpha, \quad (4.19)$$

and the  $N\sigma$  uncertainty band around the expected limit is obtained as,

$$\Phi(\sqrt{\tilde{q}_{\mu,A}}) = 1 - \alpha\Phi(N) + N. \quad (4.20)$$

On the contrary, in case of discovery, one tests  $\mu = 0$  and measures the “local significance” by the use of a modified test statistic,

$$q_0 = -2 \log \frac{\mathcal{L}(\text{data}|0, \hat{\theta}_0)}{\mathcal{L}(\text{data}|\hat{\mu}, \hat{\theta})}, \quad \hat{\mu} \geq 0. \quad (4.21)$$

In this case, the observed significance is simply given by  $Z = \sqrt{q_0}$ .

## 4.11 Results

The results are computed using the “Higgs COMBINE frequentist approach” with systematic uncertainties treated as nuisance parameters. The input signal is used in the form of shapes taken from MC simulation while the background is taken from the parametric fit using a fit function. The results are not computed for masses below 1 TeV since in this range, the uncertainties are associated with signal efficiency owing to the invariant mass selection,  $M_{\gamma+\text{jet}} > 700 \text{ GeV}$ .

### 4.11.1 Significance of local excesses in data

The significance of local excesses have been measured in data using the following significance estimator:

$$\text{Sig.} = \sqrt{-2 \ln \left( \frac{\mathcal{L}_b}{\mathcal{L}_{s+b}} \right)}, \quad (4.22)$$

where  $\mathcal{L}_b$  and  $\mathcal{L}_{s+b}$  respectively are the maximum likelihoods corresponding to the best background-only and signal+background fits to the data.

The significance values are determined only for the upward fluctuations considering positive signal strengths. The systematic uncertainties are included while evaluating the significance. The result of the significance scan for  $q^*$  signal for three coupling multipliers,  $f = 1.0, 0.5$  and  $0.1$  as a function of the resonance mass for  $\gamma + \text{jet}$  resonance hypothesis is presented in Fig. 4.41 while the corresponding results for  $b^*$  signal for all the three couplings are presented in Fig. 4.42.

The largest fluctuation observed in data has a significance of  $2.6\sigma$  for  $b^*$  signal

hypothesis for  $f = 0.5$ , very small compared to the  $5\sigma$  requirement of discovery.

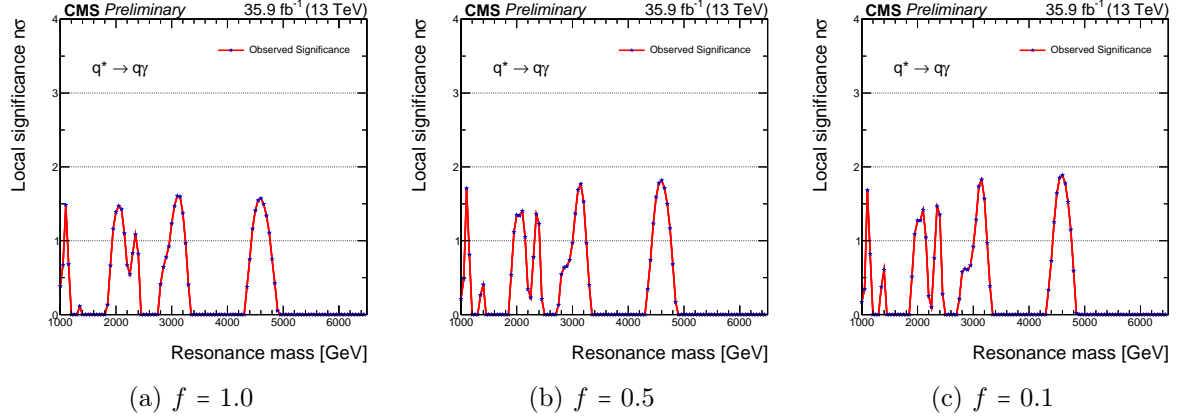


Figure 4.41: The observed significance in data for  $q^*$  signal corresponding to the coupling multipliers (a)  $f = 1.0$ , (b)  $f = 0.5$ , and (c)  $f = 0.1$  as a function of the resonance mass for  $\gamma + \text{jet}$  resonance.

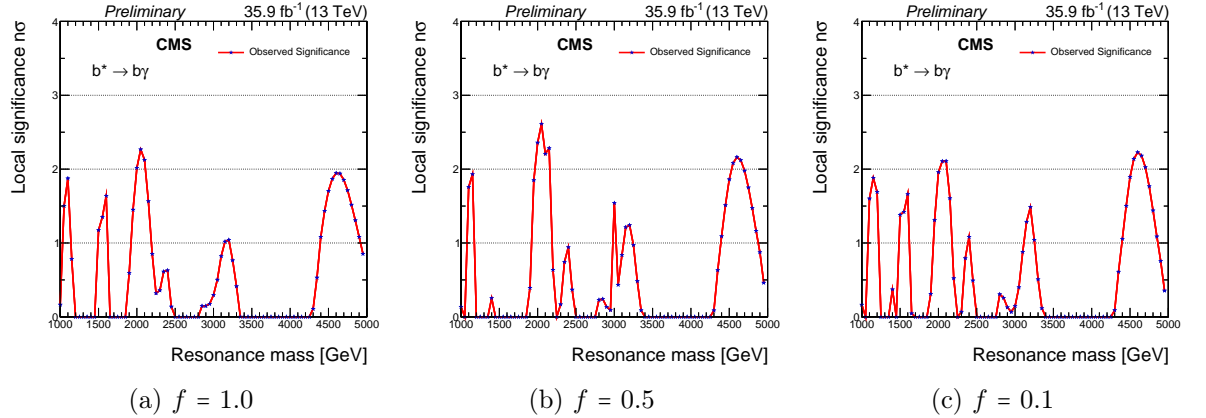


Figure 4.42: The observed significance in data for  $b^*$  signal corresponding to the coupling multipliers (a)  $f = 1.0$ , (b)  $f = 0.5$ , and (c)  $f = 0.1$  as a function of the resonance mass for  $\gamma + \text{b-jet}$  resonance.

#### 4.11.2 Exclusion limits

Since no significant excess has been observed in the mass region studied, a 95% CL upper limit on the production cross-sections and lower limit on the masses of  $q^*$  and  $b^*$  decaying to  $q\gamma$  and  $b\gamma$  respectively, has been set. The limits are calculated by evaluating the likelihood independently at successive values of resonance mass in the range from 1-6 TeV for  $q^*$  and 1-5 TeV for  $b^*$ , in steps of 50 GeV. The limits for  $b^*$  are evaluated by combining the likelihoods for 1 b-tag and 0 b-tag categories together.

The observed and expected 95% CL upper limits on the product of  $\sigma \times B \times A \times \epsilon$  and  $\sigma \times B$  for  $q^*$  and  $b^*$  resonances has been presented in Fig. 4.43 and Fig. 4.44, respectively, for all the three coupling multipliers. Here,  $\sigma$  corresponds to the production cross-section and  $B$  corresponds to the branching fraction of  $q^* \rightarrow q\gamma$  and  $b^* \rightarrow b\gamma$  processes. The product  $A \times \epsilon$  refers to the acceptance times efficiency of the  $q^*$  and  $b^*$  signals as presented in Fig. 4.15 and it varies in the range from 38% to 45% for  $q^*$  and 28% to 22% for  $b^*$  in the full mass range explored. The limits on  $\sigma \times B \times A \times \epsilon$  take into account the detector effects in the form of  $A \times \epsilon$  and thus, are referred to as detector dependent limits. On the other hand, the limits on  $\sigma \times B$  refers to the detector independent limits. Since the variation of  $A \times \epsilon$  over the explored mass range is not very large, the detector dependent and independent limits come out to be almost the same. The observed limits for both  $q^*$  and  $b^*$  resonances are found to be consistent with the expected limits in the absence of signal.

The observed cross-section upper limits are compared to the LO theoretical predictions, for the three coupling multipliers, in order to estimate the lower mass limits on the  $q^*$  and  $b^*$  resonances. The observed lower bounds obtained are 5.5 and 1.8 TeV for  $q^*$  and  $b^*$  respectively, for  $f = 1.0$ . The corresponding expected mass limits are 5.4 and 1.8 TeV. The observed (expected) limits for  $f = 0.5$  and  $f = 0.1$  for the  $q^*$  resonances have been evaluated to be 4.4 TeV (4.3 TeV) and 2.0 TeV (1.9 TeV) respectively, while the observed (expected) limit for  $f = 0.5$  for  $b^*$  resonances comes out to be 1.4 TeV (1.3 TeV). No exclusion has been observed for  $b^*$  for  $f = 0.1$ .

It has been observed that  $\sigma \times B$  (or  $\sigma \times B \times A \times \epsilon$ ) has very little dependence on  $f$ , of the order of 10-20%, so the comparison of  $\sigma \times B$  limits corresponding to  $f = 1.0$  with the theoretical predictions of lower couplings, yield approximately the same mass limit as can be seen in Fig. 4.45 for  $q^*$  and in Fig. 4.46 for  $b^*$ . The variation of the excluded mass as a function of the coupling strength, as presented in Fig. 4.47, can be obtained by evaluating the mass exclusions for intermediate couplings through the interpolation of signal efficiencies of the three signal MC samples corresponding to  $f = 1.0, 0.5$  and  $0.1$ . This result can also be interpreted in terms of  $M_{\text{Res}}/\Lambda$ , that is, if we left the assumption  $\Lambda = M_{\text{Res}}$ , the production cross-section of excited quarks is proportional to  $f$  as well as  $M_{\text{Res}}/\Lambda$ .

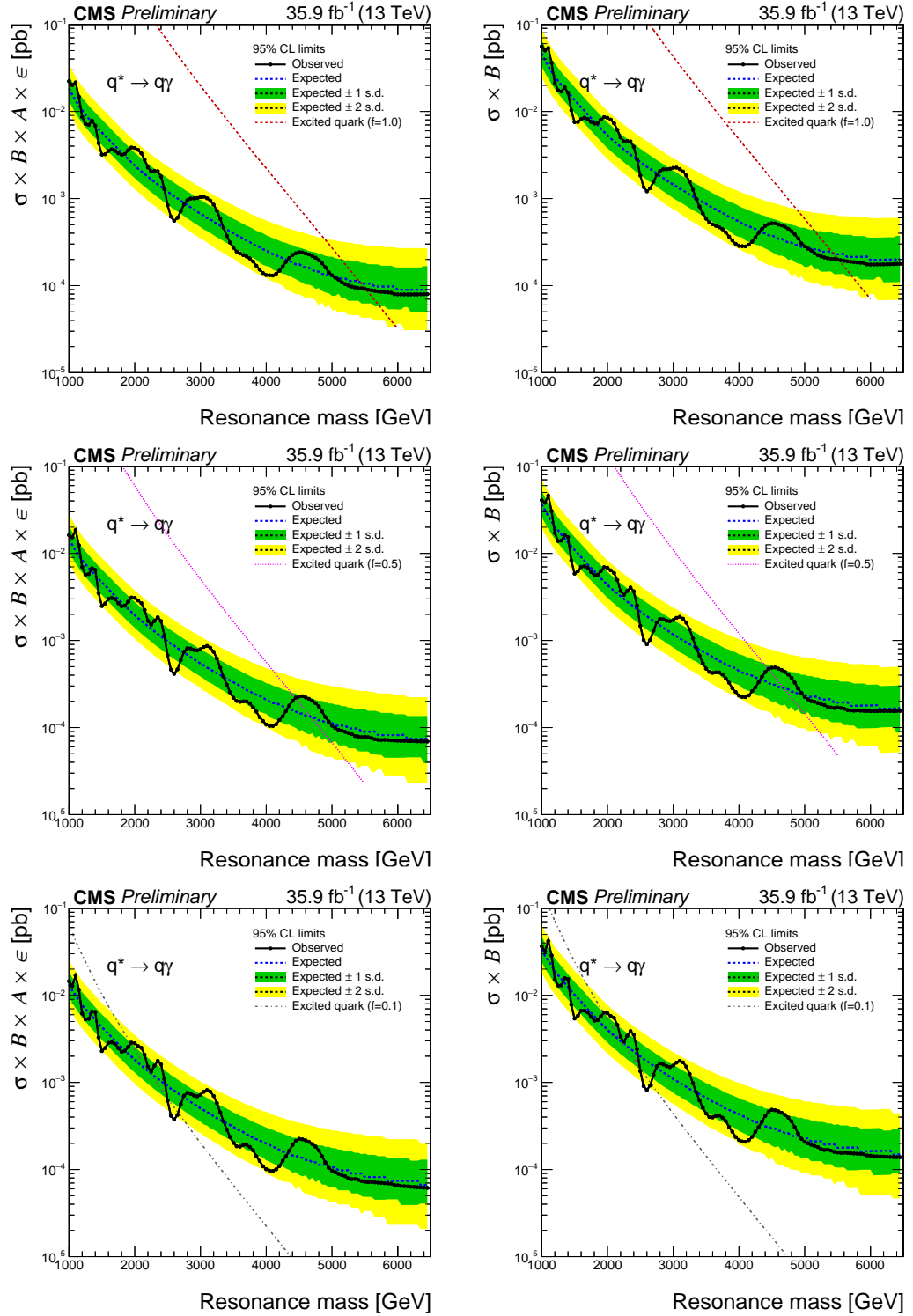


Figure 4.43: The observed and expected 95% CL upper limits on  $\sigma \times B \times A \times \epsilon$  (left column) and  $\sigma \times B$  (right column) as a function of the mass of  $q^*$  resonance, for the coupling multipliers  $f = 1.0$  (upper row),  $f = 0.5$  (middle row), and  $f = 0.1$  (lower row). The limits are also compared with the theoretical predictions for excited quark production. The inner (green) and outer (yellow) bands indicate the regions containing the 68% and 95% of the expected limits.

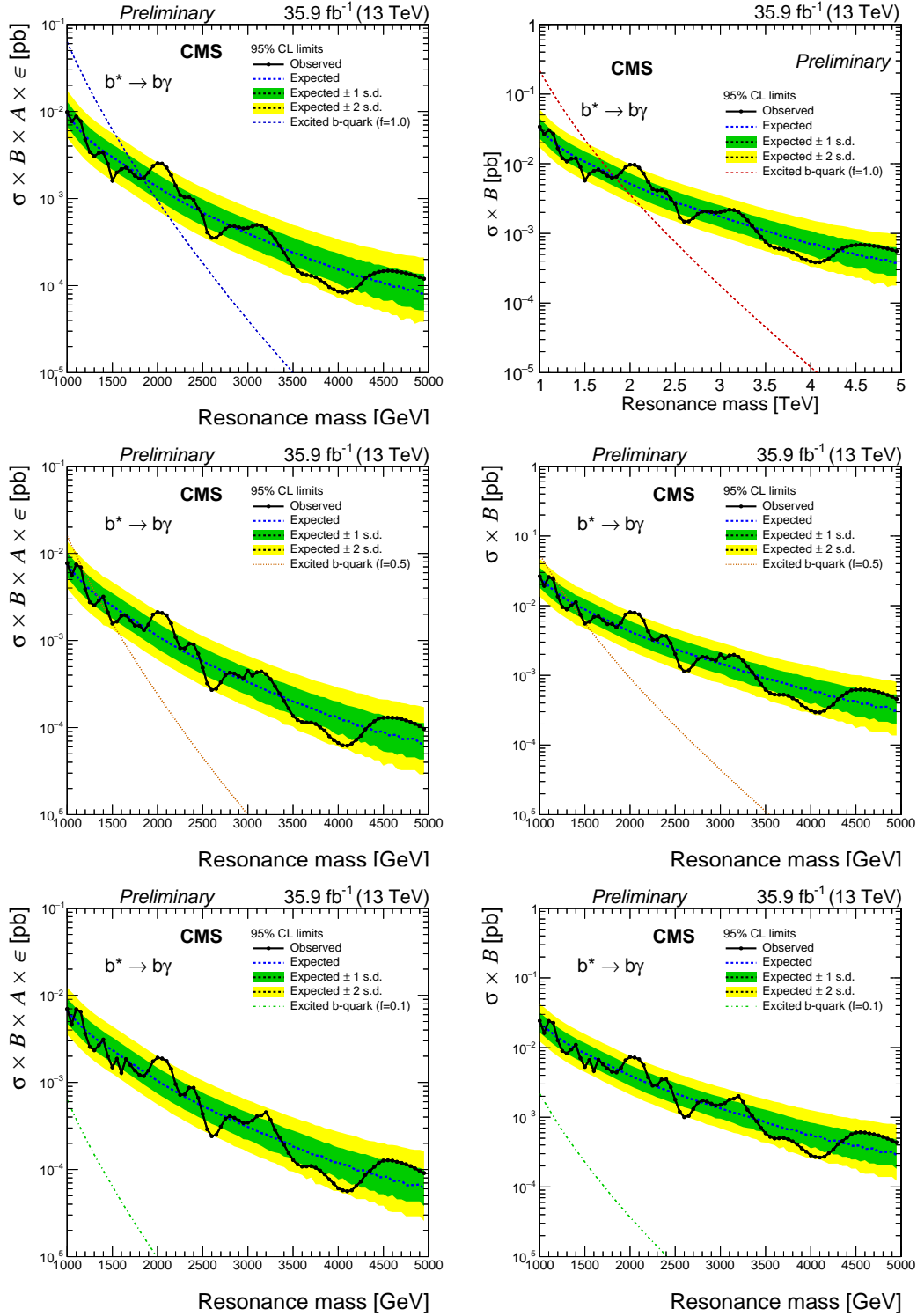


Figure 4.44: The observed and expected 95% CL upper limits on  $\sigma \times B \times A \times \epsilon$  (left column) and  $\sigma \times B$  (right column) as a function of the mass of  $b^*$  resonance, for the coupling multipliers  $f = 1.0$  (upper row),  $f = 0.5$  (middle row), and  $f = 0.1$  (lower row). The limits are also compared with the theoretical predictions for excited b-quark production. The inner (green) and outer (yellow) bands indicate the regions containing the 68% and 95% of the expected limits.



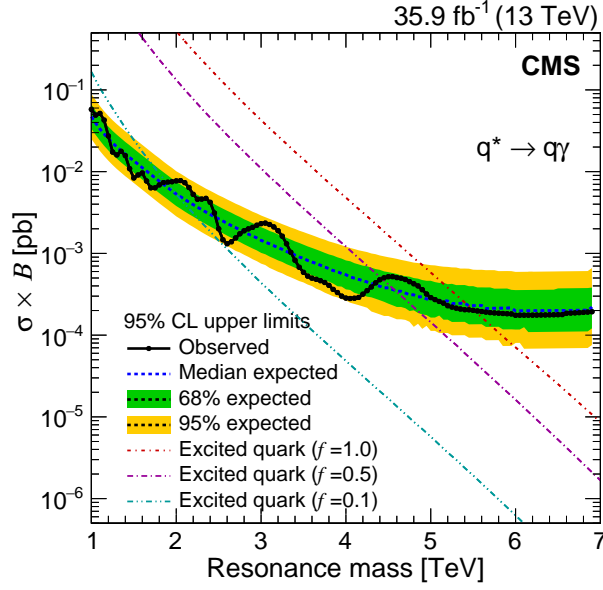


Figure 4.45: The observed and expected 95% CL upper limits on  $\sigma \times B$  as a function of the mass of the excited quark, for  $f = 1.0$ . The limits are also compared with theoretical predictions for excited quark production for the three couplings. The inner (green) band and the outer (yellow) band indicate the regions containing 68% and 95%, respectively, of the expected limits.

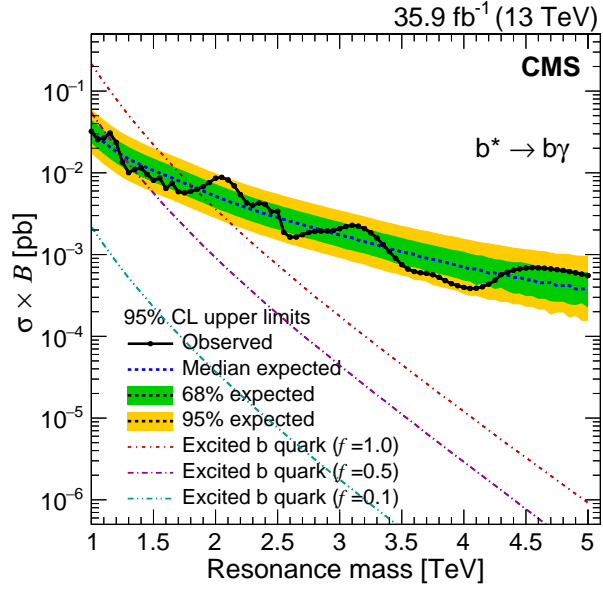


Figure 4.46: The observed and expected 95% CL upper limits on  $\sigma \times B$  as a function of the mass of the excited b-quark, for  $f = 1.0$ . The limits are also compared with theoretical predictions for excited b-quark production for the three couplings. The inner (green) band and the outer (yellow) band indicate the regions containing 68% and 95%, respectively, of the expected limits.

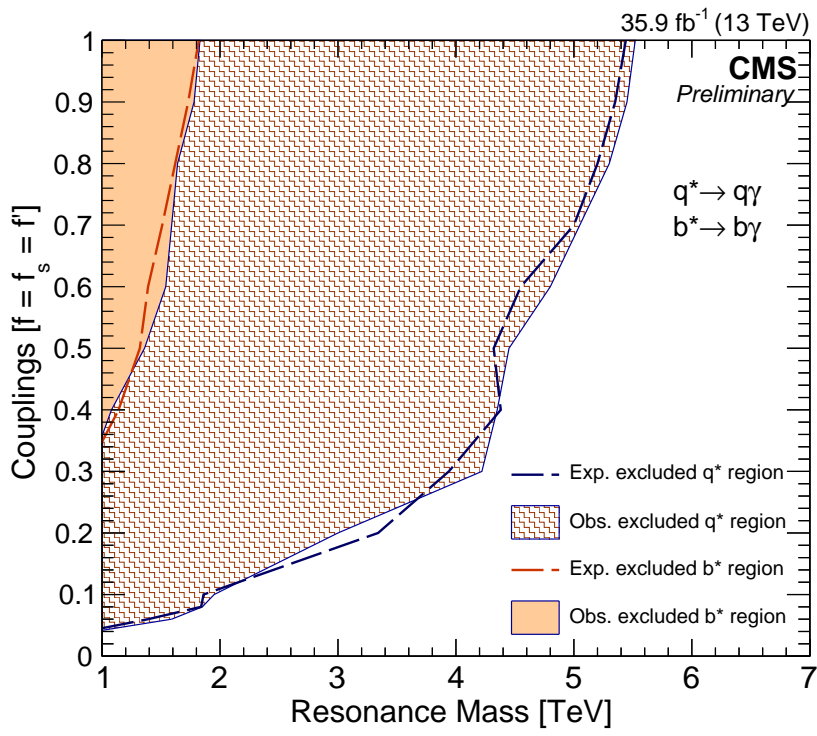


Figure 4.47: The observed and expected regions excluded at 95% CL for  $q^*$  and  $b^*$  production and decay, as a function of  $M_{q^*}$ ,  $M_{b^*}$  and  $f$ .



## BIBLIOGRAPHY

- [1] S. L. Glashow, “Partial Symmetries of Weak Interactions”, *Nucl. Phys.* **22** (1961) 579–588, doi:10.1016/0029-5582(61)90469-2.
- [2] A. Salam and J. C. Ward, “Electromagnetic and weak interactions”, *Phys. Lett.* **13** (1964) 168–171, doi:10.1016/0031-9163(64)90711-5.
- [3] S. Weinberg, “A Model of Leptons”, *Phys. Rev. Lett.* **19** (1967) 1264–1266, doi:10.1103/PhysRevLett.19.1264.
- [4] D. J. Gross and F. Wilczek, “Ultraviolet Behavior of Nonabelian Gauge Theories”, *Phys. Rev. Lett.* **30** (1973) 1343–1346, doi:10.1103/PhysRevLett.30.1343.
- [5] H. D. Politzer, “Reliable Perturbative Results for Strong Interactions?”, *Phys. Rev. Lett.* **30** (1973) 1346–1349, doi:10.1103/PhysRevLett.30.1346.
- [6] J. Dalton, “On the absorption of gases by water and other liquids”, *Memoirs of the Literary and Philosophical Society of Manchester* **1** (1805) 271–287, doi:10.1080/14786440608563325.
- [7] A. W. Thackray, “The Origin of Dalton’s Chemical Atomic Theory: Daltonian Doubts Resolved”, *Isis* **57** (1966) 35–55, doi:10.1086/350077.
- [8] J. J. Thomson, “Cathode Rays”, *Philosophical Magazine* **44** (1897) 293.
- [9] J. J. Thomson, “On the Structure of the Atom: an Investigation of the Stability and Periods of Oscillation of a number of Corpuscles arranged at equal intervals around the Circumference of a Circle, with Application of the Results to the Theory of Atomic Structure”, *Philosophical Magazine* **7** (1904) 237–265, doi:10.1080/14786440409463107.

- [10] E. Rutherford, “The scattering of alpha and beta particles by matter and the structure of the atom”, *Phil. Mag.* **21** (1911) 669–688, doi:10.1080/14786440508637080.
- [11] E. Rutherford, “The structure of the atom”, *Nature* **92** (1913) 423.
- [12] J. Chadwick, “Possible Existence of a Neutron”, *Nature* **129** (1932) 312.
- [13] A. Einstein, “On a heuristic viewpoint concerning the production and transformation of light”, *Annalen Phys.* **17** (1905) 132–148.
- [14] A. H. Compton, “A Quantum Theory of the Scattering of X-rays by Light Elements”, *Phys. Rev.* **21** (1923) 483–502, doi:10.1103/PhysRev.21.483.
- [15] A. Einstein, “On the electrodynamics of moving bodies”, *Annalen Phys.* **17** (1905) 891–921, doi:10.1002/andp.200590006.
- [16] P. A. M. Dirac, “The Quantum Theory of the Emission and Absorption of Radiation”, *Proc. R. Soc. Lond. A114* **243** (1927) 710.
- [17] C. D. Anderson, “The Positive Electron”, *Phys. Rev.* **43** (1933) 491–494, doi:10.1103/PhysRev.43.491.
- [18] R. P. Feynman, “Space-time approach to nonrelativistic quantum mechanics”, *Rev. Mod. Phys.* **20** (1948) 367–387, doi:10.1103/RevModPhys.20.367.
- [19] R. P. Feynman, “A Relativistic cutoff for classical electrodynamics”, *Phys. Rev.* **74** (1948) 939–946, doi:10.1103/PhysRev.74.939.
- [20] R. P. Feynman, “The Theory of positrons”, *Phys. Rev.* **76** (1949) 749–759, doi:10.1103/PhysRev.76.749.
- [21] J. S. Schwinger, “On Quantum electrodynamics and the magnetic moment of the electron”, *Phys. Rev.* **73** (1948) 416–417, doi:10.1103/PhysRev.73.416.
- [22] J. S. Schwinger, “Quantum electrodynamics. I A covariant formulation”, *Phys. Rev.* **74** (1948) 1439, doi:10.1103/PhysRev.74.1439.
- [23] S.-I. Tomonaga and J. R. Oppenheimer, “On Infinite Field Reactions in Quantum Field Theory”, *Phys. Rev.* **74** (1948) 224–225, doi:10.1103/PhysRev.74.224.

- [24] H. Yukawa, “On the Interaction of Elementary Particles I”, *Proc. Phys. Math. Soc. Jap.* **17** (1935) 48–57, doi:10.1143/PTPS.1.1. [Prog. Theor. Phys. Suppl.1,1(1935)].
- [25] S. H. Neddermeyer and C. D. Anderson, “Note on the Nature of Cosmic Ray Particles”, *Phys. Rev.* **51** (1937) 884–886, doi:10.1103/PhysRev.51.884.
- [26] C. M. G. Lattes, G. P. S. Occhialini, and C. F. Powell, “Observations on the Tracks of Slow Mesons in Photographic Emulsions. 1”, *Nature* **160** (1947) 453–456, doi:10.1038/160453a0.
- [27] C. L. Cowan and Reines, “Detection of the free neutrino: A Confirmation”, *Science* **124** (1956) 103, doi:10.1126/science.124.3212.103.
- [28] E. Fermi, “Fermi’s Theory of Beta Decay”, *Z. Phy.* **88** (1934) 161.
- [29] G. D. Rochester and C. C. Butler, “Evidence for the Existence of New Unstable Elementary Particles”, *Nature* **160** (1947) 855–857, doi:10.1038/160855a0.
- [30] V. D. Hopper and S. Biswas, “Evidence Concerning the Existence of the New Unstable Elementary Neutral Particle”, *Phys. Rev.* **80** (Dec, 1950) 1099, doi:10.1103/PhysRev.80.1099.
- [31] A. Bonetti, R. L. Setti, M. Panetti, and G. Tomasini, “On the existence of unstable charged particles of hyperprotonic mass”, *Il Nuovo Cimento* **10** (1953) 1736–1743, doi:10.1007/BF02781667.
- [32] C. M. York, R. B. Leighton, and E. K. Bjornerud, “Direct Experimental Evidence for the Existence of a Heavy Positive  $V$  Particle”, *Phys. Rev.* **90** (1953) 167–168, doi:10.1103/PhysRev.90.167.
- [33] E. Cowan, “A  $V$ -Decay Event with a Heavy Negative Secondary, and Identification of the Secondary  $V$ -Decay Event in a Cascade”, *Physical Review* **94** (1954) 161.
- [34] V. E. Barnes et al., “Observation of a Hyperon with Strangeness -3”, *Phys. Rev. Lett.* **12** (1964) 204–206, doi:10.1103/PhysRevLett.12.204.
- [35] M. Gell-Mann, “A Schematic Model of Baryons and Mesons”, *Phys. Lett.* **8** (1964) 214–215, doi:10.1016/S0031-9163(64)92001-3.

- [36] G. Zweig, “An  $SU_3$  model for strong interaction symmetry and its breaking; Version 2”,. Version 1 is CERN preprint 8182/TH.401, Jan. 17, 1964.
- [37] Y. L. Dokshitzer, “Calculation of the structure functions for deep inelastic scattering and  $e^+e^-$  annihilation by perturbation theory in quantum chromodynamics”, *Zh. Eksp. Teor. Fiz* **73** (1977) 1216.
- [38] H. Fritzsch, M. Gell-Mann, and H. Leutwyler, “Advantages of the Color Octet Gluon Picture”, *Phys. Lett.* **47B** (1973) 365, doi:10.1016/0370-2693(73)90625-4.
- [39] TASSO Collaboration, “High energy trends in  $e^+e^-$  physics”, *Invited talk at Geneva Conference* (1979).
- [40] J. D. Bjorken and S. L. Glashow, “Elementary Particles and  $SU(4)$ ”, *Phys. Lett.* **11** (1964) 255–257, doi:10.1016/0031-9163(64)90433-0.
- [41] S. L. Glashow, J. Iliopoulos, and L. Maiani, “Weak Interactions with Lepton-Hadron Symmetry”, *Phys. Rev.* **D2** (1970) 1285–1292, doi:10.1103/PhysRevD.2.1285.
- [42] E598 Collaboration, “Experimental Observation of a Heavy Particle J”, *Phys. Rev. Lett.* **33** (1974) 1404–1406, doi:10.1103/PhysRevLett.33.1404.
- [43] SLAC-SP-017 Collaboration, “Discovery of a Narrow Resonance in  $e^+e^-$  Annihilation”, *Phys. Rev. Lett.* **33** (1974) 1406–1408, doi:10.1103/PhysRevLett.33.1406. [Adv. Exp. Phys.5,141(1976)].
- [44] M. L. Perl et al., “Evidence for Anomalous Lepton Production in  $e^+e^-$  Annihilation”, *Phys. Rev. Lett.* **35** (1975) 1489–1492, doi:10.1103/PhysRevLett.35.1489.
- [45] S. W. Herb et al., “Observation of a Dimuon Resonance at 9.5-GeV in 400-GeV Proton-Nucleus Collisions”, *Phys. Rev. Lett.* **39** (1977) 252–255, doi:10.1103/PhysRevLett.39.252.
- [46] CDF Collaboration, “Observation of top quark production in  $\bar{p}p$  collisions”, *Phys. Rev. Lett.* **74** (1995) 2626–2631, doi:10.1103/PhysRevLett.74.2626, arXiv:hep-ex/9503002.

- [47] D0 Collaboration, “Observation of the top quark”, *Phys. Rev. Lett.* **74** (1995) 2632–2637, doi:10.1103/PhysRevLett.74.2632, arXiv:hep-ex/9503003.
- [48] T. D. Lee and C.-N. Yang, “Question of Parity Conservation in Weak Interactions”, *Phys. Rev.* **104** (1956) 254–258, doi:10.1103/PhysRev.104.254.
- [49] C. S. Wu et al., “Experimental Test of Parity Conservation in Beta Decay”, *Phys. Rev.* **105** (1957) 1413–1414, doi:10.1103/PhysRev.105.1413.
- [50] C.-N. Yang and R. L. Mills, “Conservation of Isotopic Spin and Isotopic Gauge Invariance”, *Phys. Rev.* **96** (1954) 191–195, doi:10.1103/PhysRev.96.191.
- [51] P. W. Higgs, “Broken symmetries, massless particles and gauge fields”, *Phys. Lett.* **12** (1964) 132–133, doi:10.1016/0031-9163(64)91136-9.
- [52] P. W. Higgs, “Broken Symmetries and the Masses of Gauge Bosons”, *Phys. Rev. Lett.* **13** (1964) 508–509, doi:10.1103/PhysRevLett.13.508.
- [53] P. W. Higgs, “Spontaneous Symmetry Breakdown without Massless Bosons”, *Phys. Rev.* **145** (1966) 1156–1163, doi:10.1103/PhysRev.145.1156.
- [54] F. Englert and R. Brout, “Broken Symmetry and the Mass of Gauge Vector Mesons”, *Phys. Rev. Lett.* **13** (1964) 321–323, doi:10.1103/PhysRevLett.13.321.
- [55] G. S. Guralnik, C. R. Hagen, and T. W. B. Kibble, “Global Conservation Laws and Massless Particles”, *Phys. Rev. Lett.* **13** (1964) 585–587, doi:10.1103/PhysRevLett.13.585.
- [56] Gargamelle Neutrino Collaboration, “Observation of Neutrino Like Interactions Without Muon Or Electron in the Gargamelle Neutrino Experiment”, *Phys. Lett.* **B46** (1973) 138–140, doi:10.1016/0370-2693(73)90499-1.
- [57] UA1 Collaboration, “Experimental Observation of Isolated Large Transverse Energy Electrons with Associated Missing Energy at  $\sqrt{s} = 540$  GeV”, *Phys. Lett.* **B122** (1983) 103–116, doi:10.1016/0370-2693(83)91177-2.



- [58] UA2 Collaboration, “Observation of Single Isolated Electrons of High Transverse Momentum in Events with Missing Transverse Energy at the CERN  $p\bar{p}$  Collider”, *Phys. Lett.* **B122** (1983) 476–485, doi:10.1016/0370-2693(83)91605-2.
- [59] UA1 Collaboration, “Experimental Observation of Lepton Pairs of Invariant Mass Around 95-GeV/c<sup>2</sup> at the CERN SPS Collider”, *Phys. Lett.* **B126** (1983) 398–410, doi:10.1016/0370-2693(83)90188-0.
- [60] UA1 Collaboration, “Further Evidence for Charged Intermediate Vector Bosons at the SPS Collider”, *Phys. Lett.* **B129** (1983) 273–282, doi:10.1016/0370-2693(83)90860-2.
- [61] UA2 Collaboration, “Evidence for  $Z^0 \rightarrow e^+e^-$  at the CERN  $p\bar{p}$  Collider”, *Phys. Lett.* **B129** (1983) 130–140, doi:10.1016/0370-2693(83)90744-X.
- [62] ATLAS Collaboration, “Observation of a new particle in the search for the Standard Model Higgs boson with the ATLAS detector at the LHC”, *Phys. Lett.* **B716** (2012) 1–29, doi:10.1016/j.physletb.2012.08.020, arXiv:1207.7214.
- [63] CMS Collaboration, “Observation of a new boson at a mass of 125 GeV with the CMS experiment at the LHC”, *Phys. Lett.* **B716** (2012) 30–61, doi:10.1016/j.physletb.2012.08.021, arXiv:1207.7235.
- [64] CMS Collaboration, “Combination of standard model Higgs boson searches and measurements of the properties of the new boson with a mass near 125 GeV”, (2013). CMS-PAS-HIG-13-005.
- [65] ATLAS Collaboration, “Updated coupling measurements of the Higgs boson with the ATLAS detector using up to 25 fb<sup>-1</sup> of proton-proton collision data”, (2014). ATLAS-CONF-2014-009.
- [66] Super-Kamiokande Collaboration, “Evidence for oscillation of atmospheric neutrinos”, *Phys. Rev. Lett.* **81** (1998) 1562–1567, doi:10.1103/PhysRevLett.81.1562, arXiv:hep-ex/9807003.
- [67] Super-Kamiokande Collaboration, “Constraints on neutrino oscillations using 1258 days of Super-Kamiokande solar neutrino data”, *Phys. Rev. Lett.* **86** (2001) 5656–5660, doi:10.1103/PhysRevLett.86.5656, arXiv:hep-ex/0103033.

- [68] SNO Collaboration, “Direct evidence for neutrino flavor transformation from neutral current interactions in the Sudbury Neutrino Observatory”, *Phys. Rev. Lett.* **89** (2002) 011301, doi:10.1103/PhysRevLett.89.011301, arXiv:nucl-ex/0204008.
- [69] KamLAND Collaboration, “Measurement of neutrino oscillation with KamLAND: Evidence of spectral distortion”, *Phys. Rev. Lett.* **94** (2005) 081801, doi:10.1103/PhysRevLett.94.081801, arXiv:hep-ex/0406035.
- [70] K2K Collaboration, “Evidence for muon neutrino oscillation in an accelerator-based experiment”, *Phys. Rev. Lett.* **94** (2005) 081802, doi:10.1103/PhysRevLett.94.081802, arXiv:hep-ex/0411038.
- [71] MINOS Collaboration, “Observation of muon neutrino disappearance with the MINOS detectors and the NuMI neutrino beam”, *Phys. Rev. Lett.* **97** (2006) 191801, doi:10.1103/PhysRevLett.97.191801, arXiv:hep-ex/0607088.
- [72] Particle Data Group Collaboration, “Review of Particle Physics”, *Chin. Phys.* **C38** (2014) 090001, doi:10.1088/1674-1137/38/9/090001.
- [73] F. J. Dyson, “The Radiation theories of Tomonaga, Schwinger, and Feynman”, *Phys. Rev.* **75** (1949) 486–502, doi:10.1103/PhysRev.75.486.
- [74] M. E. Peskin and D. V. Schroeder, “An Introduction to quantum field theory”. Addison-Wesley (1995) 842 p, Reading, USA, 1995.
- [75] S. Kluth, “Review of alpha(s) Measurements”, *Conf. Proc.* **C060726** (2006) 449–452, arXiv:hep-ex/0609020. [,449(2006)].
- [76] D. J. Gross and F. Wilczek, “Asymptotically Free Gauge Theories. 1”, *Phys. Rev.* **D8** (1973) 3633–3652, doi:10.1103/PhysRevD.8.3633.
- [77] D. J. Gross and F. Wilczek, “Asymptotically Free Gauge Theories. 2.”, *Phys. Rev.* **D9** (1974) 980–993, doi:10.1103/PhysRevD.9.980.
- [78] H. D. Politzer, “Asymptotic Freedom: An Approach to Strong Interactions”, *Phys. Rept.* **14** (1974) 129–180, doi:10.1016/0370-1573(74)90014-3.
- [79] M. Goldhaber, L. Grodzins, and A. W. Sunyar, “Helicity of Neutrinos”, *Phys. Rev.* **109** (1958) 1015, doi:10.1103/PhysRev.109.1015.

- [80] T. Nakano and K. Nishijima, “Charge Independence for V-particles”, *Prog. Theor. Phys.* **10** (1953) 581, doi:10.1143/PTP.10.581.
- [81] K. Nishijima and Kazuhiko, “Charge Independence Theory of V Particles”, *Prog. Theor. Phys.* **13** (1955) 285, doi:10.1143/PTP.13.285.
- [82] M. Gell-Mann, “The interpretation of the new particles as displaced charge multiplets”, *Nuovo Cim.* **4** (1956) 848, doi:10.1007/BF02748000.
- [83] A. Djouadi, “The Anatomy of electro-weak symmetry breaking. I: The Higgs boson in the standard model”, *Phys. Rept.* **457** (2008) 1, doi:10.1016/j.physrep.2007.10.004, arXiv:hep-ph/0503172.
- [84] J. C. Pati, A. Salam, and J. A. Strathdee, “Are Quarks Composite?”, *Phys. Lett.* **B59** (1975) 265, doi:10.1016/0370-2693(75)90042-8.
- [85] E. Eichten, K. D. Lane, and M. E. Peskin, “New Tests for Quark and Lepton Substructure”, *Phys. Rev. Lett.* **50** (1983) 811, doi:10.1103/PhysRevLett.50.811.
- [86] U. Baur, I. Hinchliffe, and D. Zeppenfeld, “Excited Quark Production at Hadron Colliders”, *Int.J.Mod.Phys.* **A2** (1987) 1285, doi:10.1142/S0217751X87000661.
- [87] U. Baur, M. Spira, and P. Zerwas, “Excited Quark and Lepton Production at Hadron Colliders”, *Phys.Rev.* **D42** (1990) 815, doi:10.1103/PhysRevD.42.815.
- [88] ZEUS Collaboration, “A Search for excited fermions in  $e^+p$  collisions at HERA”, *Z. Phys.* **C76** (1997) 631, doi:10.1007/s002880050585, arXiv:hep-ex/9708007.
- [89] CDF Collaboration, “Search for excited quarks in  $p\bar{p}$  collisions at  $\sqrt{s} = 1.8$  TeV”, *Phys.Rev.Lett.* **72** (1994) 3004, doi:10.1103/PhysRevLett.72.3004.
- [90] CDF Collaboration, “Search for new particles decaying to dijets at CDF”, *Phys.Rev.* **D55** (1997) 5263, doi:10.1103/PhysRevD.55.R5263, arXiv:hep-ex/9702004.
- [91] D0 Collaboration Collaboration, “Search for new particles in the two jet decay channel with the D0 detector”, *Phys.Rev.* **D69** (2004) 111101, doi:10.1103/PhysRevD.69.111101, arXiv:hep-ex/0308033.

- [92] ATLAS Collaboration, “Search for new phenomena in dijet mass and angular distributions from  $pp$  collisions at  $\sqrt{s} = 13$  TeV with the ATLAS detector”, *Phys. Lett.* **B754** (2016) 302, doi:10.1016/j.physletb.2016.01.032, arXiv:1512.01530.
- [93] ATLAS Collaboration, “Search for new phenomena with photon+jet events in proton-proton collisions at  $\sqrt{s} = 13$  TeV with the ATLAS detector”, *JHEP* **03** (2016) 041, doi:10.1007/JHEP03(2016)041, arXiv:1512.05910.
- [94] CMS Collaboration, “Search for narrow resonances decaying to dijets in proton-proton collisions at  $\sqrt{s} = 13$  TeV”, *Phys. Rev. Lett.* **116** (2016), no. 7, 071801, doi:10.1103/PhysRevLett.116.071801, arXiv:1512.01224.
- [95] ATLAS Collaboration, “Search for single  $b^*$ -quark production with the ATLAS detector at  $\sqrt{s} = 7$  TeV”, *Phys. Lett.* **B721** (2013) 171, doi:10.1016/j.physletb.2013.03.016, arXiv:1301.1583.
- [96] CMS Collaboration, “Search for the production of an excited bottom quark decaying to  $tW$  in proton-proton collisions at  $\sqrt{s} = 8$  TeV”, *JHEP* **01** (2016) 166, doi:10.1007/JHEP01(2016)166, arXiv:1509.08141.
- [97] CMS Collaboration, “Search for resonances and quantum black holes using dijet mass spectra in proton-proton collisions at  $\sqrt{s} = 8$  TeV”, *Phys. Rev.* **D91** (2015) 052009, doi:10.1103/PhysRevD.91.052009, arXiv:1501.04198.
- [98] D. S. Gorbunov and V. A. Rubakov, “Introduction to the theory of the early universe: Hot big bang theory”. World Scientific, Hackensack, 2011.
- [99] O. S. Brüning et al., “LHC Design Report”. CERN, Geneva, 2004. CERN-2004-003-V-1.
- [100] L. Evans and P. Bryant, “LHC Machine”, *JINST* **3** (2008) S08001, doi:10.1088/1748-0221/3/08/S08001.
- [101] S. Myers and E. Picasso, “The design, construction and commissioning of the CERN large Electron–Positron collider”, *Contemporary Physics* **31** (1990) 387, doi:10.1080/00107519008213789.

- [102] S. Holmes, R. S. Moore, and V. Shiltsev, “Overview of the Tevatron Collider Complex: Goals, Operations and Performance”, *JINST* **6** (2011) T08001, doi:10.1088/1748-0221/6/08/T08001, arXiv:1106.0909.
- [103] ATLAS Collaboration, A. Airapetian et al., “ATLAS detector and physics performance: Technical Design Report, 1”. TDR ATLAS. CERN, Geneva, 1999. ATLAS-TDR-014; CERN-LHCC-99-014.
- [104] CMS Collaboration, G. L. Bayatian et al., “CMS Physics: Technical Design Report Volume 1: Detector Performance and Software”. TDR CMS. CERN, Geneva, 2006. CERN-LHCC-2006-001.
- [105] ALICE Collaboration, P. Cortese et al., “ALICE physics performance: Technical Design Report”. TDR ALICE. CERN, Geneva, 2005. ALICE-TDR-13; CERN-LHCC-2005-030.
- [106] LHCb Collaboration, R. Antunes-Nobrega et al., “LHCb reoptimized detector design and performance: Technical Design Report”. TDR LHCb. CERN, Geneva, 2003. LHCb-TDR-9; CERN-LHCC-2003-030.
- [107] “CERN Experiments and Facilities”. <http://home.web.cern.ch/about>. Accessed, 2015.
- [108] CMS Collaboration, S. Chatrchyan et al., “CMS Luminosity - Public Results”. <https://twiki.cern.ch/twiki/bin/view/CMSPublic/LumiPublicResults>. Accessed: 2014-09-30.
- [109] CMS Collaboration, “The CMS experiment at the CERN LHC”, *JINST* **3** (2008) S08004, doi:10.1088/1748-0221/3/08/S08004.
- [110] CMS Collaboration, V. Karimäki et al., “The CMS tracker system project: Technical Design Report”. Technical Design Report CMS. CERN, Geneva, 1997.
- [111] CMS Collaboration, “Description and performance of track and primary-vertex reconstruction with the CMS tracker”, *JINST* **9** (2014) P10009, doi:10.1088/1748-0221/9/10/P10009, arXiv:1405.6569.
- [112] CMS Collaboration, “Studies of Tracker Material”, (2010). CMS-PAS-TRK-10-003.

- [113] R. Baur and W. H. Bertl, “The CMS pixel vertex detector”, *Nucl. Phys. Proc. Suppl.* **78** (1999) 293, doi:10.1016/S0920-5632(99)00560-5.
- [114] CMS Collaboration, M. Dominguez et al., “CMS Technical Design Report for the Pixel Detector Upgrade”. Technical Design Report CMS. CERN, Geneva, 2012.
- [115] CMS Collaboration, “Upgrade of the CMS tracker”, *JINST* **9** (2014) C03041, doi:10.1088/1748-0221/9/03/C03041.
- [116] CMS Collaboration, “The CMS electromagnetic calorimeter project: Technical Design Report”. TDR CMS. CERN, Geneva, 1997. CERN-LHCC-97-033.
- [117] CMS Collaboration, “Energy Calibration and Resolution of the CMS Electromagnetic Calorimeter in  $pp$  Collisions at  $\sqrt{s} = 7$  TeV”, *JINST* **8** (2013) P09009, doi:10.1088/1748-0221/8/09/P09009, arXiv:1306.2016.
- [118] R. Wigmans, “Advances in hadron calorimetry”, *Ann. Rev. Nucl. Part. Sci.* **41** (1991) 133, doi:10.1146/annurev.ns.41.120191.001025.
- [119] CMS Collaboration, “The CMS hadron calorimeter project: Technical Design Report”. TDR CMS. CERN, Geneva, 1997. CERN-LHCC-97-031.
- [120] CMS HCAL Collaboration, “Design, performance, and calibration of CMS hadron-barrel calorimeter wedges”, *Eur.Phys.J.* **C55** (2008) 159–171, doi:10.1140/epjc/s10052-008-0573-y.
- [121] CMS HCAL Collaboration, “Design, performance, and calibration of CMS hadron endcap calorimeters”, (2008). CERN-CMS-NOTE-2008-010.
- [122] G. Bayatian et al., “Design, performance and calibration of the CMS forward calorimeter wedges”, *Eur.Phys.J.* **C53** (2008) 139–166, doi:10.1140/epjc/s10052-007-0459-4.
- [123] CMS HCAL Collaboration, “Design, performance, and calibration of the CMS Hadron-outer calorimeter”, *Eur.Phys.J.* **C57** (2008) 653–663, doi:10.1140/epjc/s10052-008-0756-6.
- [124] CMS Collaboration, “The CMS magnet project: Technical Design Report”. Technical Design Report CMS. CERN, Geneva, 1997.

- [125] CMS Collaboration, “The CMS muon project: Technical Design Report”. TDR CMS. CERN, Geneva, 1997. CERN-LHCC-97-032.
- [126] CMS Collaboration, G. L. Bayatyan et al., “CMS TriDAS project: Technical Design Report, Volume 1: The Trigger Systems”. TDR CMS. CERN, Geneva, 2000. CMS-TDR-6-1; CERN-LHCC-2000-038.
- [127] CMS Collaboration, S. Cittolin et al., “CMS The TriDAS Project: Technical Design Report, Volume 2: Data Acquisition and High-Level Trigger. CMS trigger and data-acquisition project”. TDR CMS. CERN, Geneva, 2002. CMS-TDR-6; CERN-LHCC-2002-026.
- [128] C. Eck et al., “LHC computing Grid: Technical Design Report. Version 1.06 (20 Jun 2005)”. Technical Design Report LCG. CERN, Geneva, 2005.
- [129] M. Giffels et al., “The CMS Data Management System”, *J. Phys. Conf. Ser.* **513** (2014) 042052, doi:10.1088/1742-6596/513/4/042052.
- [130] R. Egeland, T. Wildish, and S. Metson, “Data transfer infrastructure for CMS data taking”, *Proceedings of Science* **ACAT08** (2008) 033.
- [131] R. Egeland, T. Wildish, and C.-H. Huang, “PhEDEx Data Service”, Technical Report CMS-CR-2009-071, CERN, Geneva, (2009). <https://cds.cern.ch/record/1196164>.
- [132] CMS Collaboration, “The CMS dataset bookkeeping service”, *J. Phys. Conf. Ser.* **119** (2008) 072001, doi:10.1088/1742-6596/119/7/072001.
- [133] V. Kuznetsov, D. Evans, and S. Metson, “The CMS data aggregation system”, *Procedia Computer Science* **1** (2010) 1535, doi:10.1016/j.procs.2010.04.172.
- [134] R. Brun and F. Rademakers, “ROOT: An object oriented data analysis framework”, *Nucl. Instrum. Meth.* **A389** (1997) 81, doi:10.1016/S0168-9002(97)00048-X.
- [135] CMS Collaboration, “The CMS reconstruction software”, *J. Phys. Conf. Ser.* **331** (2011) 032020, doi:10.1088/1742-6596/331/3/032020.
- [136] A. Buckley et al., “General-purpose event generators for LHC physics”, *Phys. Rept.* **504** (2011) 145–233, doi:10.1016/j.physrep.2011.03.005, arXiv:1101.2599.

- [137] M. Dobbs et al., “Les Houches guidebook to Monte Carlo generators for hadron collider physics”, `arXiv:hep-ph/0403045`.
- [138] C. P. Robert, “Monte Carlo Methods”. Wiley Online Library, 2004.
- [139] C. P. Robert, “Monte Carlo Methods”,  
`doi:10.1002/9781118445112.stat03876.pub2`.
- [140] CMS Collaboration, “Particle-flow reconstruction and global event description with the CMS detector”, *JINST* **12** (2017) P10003,  
`doi:10.1088/1748-0221/12/10/P10003`, `arXiv:1706.04965`.
- [141] CMS Collaboration, “Track Reconstruction in the CMS tracker”, Technical Report CMS-NOTE-2006-041, CERN, Geneva, (2006).  
`https://cds.cern.ch/record/934067`.
- [142] R. Fruhwirth, “Application of Kalman filtering to track and vertex fitting”, *Nucl.Instrum.Meth.* **A262** (1987) 444–450,  
`doi:10.1016/0168-9002(87)90887-4`.
- [143] P. Billoir, “Progressive track recognition with a Kalman like fitting procedure”, *Comput. Phys. Commun.* **57** (1989) 390–394,  
`doi:10.1016/0010-4655(89)90249-X`.
- [144] P. Billoir and S. Qian, “Simultaneous pattern recognition and track fitting by the Kalman filtering method”, *Nucl. Instrum. Meth.* **A294** (1990) 219,  
`doi:10.1016/0168-9002(90)91835-Y`.
- [145] CMS Collaboration, “Beam Position Determination using Tracks”, Technical Report CMS-NOTE-2007-021, CERN, Geneva, (2007).  
`https://cds.cern.ch/record/1061285`.
- [146] K. Rose, “Deterministic Annealing for Clustering, Compression, Classification, Regression, and Related Optimization Problems”, *Proceedings of the IEEE* **86** (1998) `doi:10.1109/5.726788`.
- [147] CMS Collaboration, “Performance of photon reconstruction and identification with the CMS detector in proton-proton collisions at  $\sqrt{s} = 8$  TeV”, `arXiv:1502.02702`.
- [148] CMS Collaboration, “Review of clustering algorithms and energy corrections in ECAL”, technical report, CERN, Geneva, (2010).  
`https://cds.cern.ch/record/1365024`.



- [149] E. Meschi, T. Monteiro, C. Seez, and P. Vikas, “Electron Reconstruction in the CMS Electromagnetic Calorimeter”, Technical Report CMS-NOTE-2001-034, CERN, Geneva, (2001).  
<https://cds.cern.ch/record/687345>.
- [150] S. Catani, Y. L. Dokshitzer, M. Seymour, and B. Webber, “Longitudinally invariant  $k_t$  clustering algorithms for hadron hadron collisions”, *Nucl.Phys.* **B406** (1993) 187, doi:10.1016/0550-3213(93)90166-M.
- [151] M. Cacciari, G. P. Salam, and G. Soyez, “The Anti- $k_t$  jet clustering algorithm”, *JHEP* **0804** (2008) 063,  
doi:10.1088/1126-6708/2008/04/063, arXiv:0802.1189.
- [152] CMS Collaboration, “A Cambridge-Aachen (C-A) based Jet Algorithm for boosted top-jet tagging”, Technical Report CMS-PAS-JME-09-001, CERN, Geneva, (2009). <http://cds.cern.ch/record/1194489>.
- [153] Y. L. Dokshitzer, G. Leder, S. Moretti, and B. Webber, “Better jet clustering algorithms”, *JHEP* **9708** (1997) 001,  
doi:10.1088/1126-6708/1997/08/001, arXiv:hep-ph/9707323.
- [154] CMS Collaboration, “Particle-Flow Event Reconstruction in CMS and Performance for Jets, Taus, and MET”, Technical Report CMS-PAS-PFT-09-001, CERN, Geneva, (2009).  
<https://cds.cern.ch/record/1194487>.
- [155] CMS Collaboration, “Plans for Jet Energy Corrections at CMS”, Technical Report CMS-PAS-JME-07-002, CERN, 2008. Geneva, (2008).  
<https://cds.cern.ch/record/1194485>.
- [156] M. Cacciari and G. P. Salam, “Pileup subtraction using jet areas”, *Phys.Lett.* **B659** (2008) 119, doi:10.1016/j.physletb.2007.09.077,  
arXiv:0707.1378.
- [157] CMS Collaboration, “Identification of b-quark jets with the CMS experiment”, *JINST* **8** (2013) P04013,  
doi:10.1088/1748-0221/8/04/P04013, arXiv:1211.4462.
- [158] CMS Collaboration, “Identification of heavy-flavour jets with the CMS detector in pp collisions at 13 TeV”, (2017). arXiv:1712.07158. Submitted to *JINST*.

- [159] CMS Collaboration, “Jet Identification in the CMS detector”.  
<https://twiki.cern.ch/twiki/bin/viewauth/CMS/JetID>. Accessed:  
 2016.
- [160] J. Shiers, “The Worldwide LHC Computing Grid (worldwide LCG)”,  
*Computer Physics Communications* **177** (2007) 219,  
 doi:10.1016/j.cpc.2007.02.021. Proceedings of the Conference on  
 Computational Physics 2006.
- [161] A. Martin, W. Stirling, R. Thorne, and G. Watt, “Parton distributions for  
 the LHC”, *Eur.Phys.J.* **C63** (2009) 189–285,  
 doi:10.1140/epjc/s10052-009-1072-5, arXiv:0901.0002.
- [162] T. Sjöstrand et al., “An Introduction to PYTHIA 8.2”, *Comput. Phys.*  
*Commun.* **191** (2015) 159, doi:10.1016/j.cpc.2015.01.024,  
 arXiv:1410.3012.
- [163] J. Alwall et al., “The automated computation of tree-level and  
 next-to-leading order differential cross sections, and their matching to  
 parton shower simulations”, *JHEP* **1407** (2014) 079,  
 doi:10.1007/JHEP07(2014)079, arXiv:1405.0301.
- [164] M. Bahr et al., “Herwig++ Physics and Manual”, *Eur.Phys.J.* **C58** (2008)  
 639–707, doi:10.1140/epjc/s10052-008-0798-9, arXiv:0803.0883.
- [165] M. L. Mangano et al., “ALPGEN, a generator for hard multiparton  
 processes in hadronic collisions”, *JHEP* **0307** (2003) 001,  
 doi:10.1088/1126-6708/2003/07/001, arXiv:hep-ph/0206293.
- [166] T. Gleisberg et al., “Event generation with SHERPA 1.1”, *JHEP* **0902**  
 (2009) 007, doi:10.1088/1126-6708/2009/02/007, arXiv:0811.4622.
- [167] T. Sjöstrand and M. Bengtsson, “The Lund Monte Carlo for Jet  
 Fragmentation and e+ e- Physics. Jetset Version 6.3: An Update”, *Comput.*  
*Phys. Commun.* **43** (1987) 367, doi:10.1016/0010-4655(87)90054-3.
- [168] P. de Aquino et al., “ALOHA: Automatic Libraries Of Helicity Amplitudes  
 for Feynman Diagram Computations”, *Comput. Phys. Commun.* **183**  
 (2012) 2254–2263, doi:10.1016/j.cpc.2012.05.004, arXiv:1108.2041.

- [169] J. Alwall et al., “A Standard format for Les Houches event files”, *Comput.Phys.Commun.* **176** (2007) 300–304, doi:10.1016/j.cpc.2006.11.010, arXiv:hep-ph/0609017.
- [170] F. Krauss, “Matrix elements and parton showers in hadronic interactions”, *JHEP* **0208** (2002) 015, doi:10.1088/1126-6708/2002/08/015, arXiv:hep-ph/0205283.
- [171] M. L. Mangano, M. Moretti, and R. Pittau, “Multijet matrix elements and shower evolution in hadronic collisions:  $Wb\bar{b} + n$  jets as a case study”, *Nucl.Phys.* **B632** (2002) 343–362, doi:10.1016/S0550-3213(02)00249-3, arXiv:hep-ph/0108069.
- [172] GEANT4 Collaboration, “GEANT4 — a simulation toolkit”, *Nucl. Instrum. Meth. A* **506** (2003) 250, doi:10.1016/S0168-9002(03)01368-8.
- [173] CMS Collaboration, “CRAB: Distributed analysis tool for CMS”, Technical Report CMS-CR-2009-318, CERN, Geneva, (2009). <https://cds.cern.ch/record/1358821>.
- [174] CMS Collaboration, “Event generator tunes obtained from underlying event and multiparton scattering measurements”, *Eur. Phys. J. C* **76** (2016) 155, doi:10.1140/epjc/s10052-016-3988-x, arXiv:1512.00815.
- [175] P. Skands, S. Carrazza, and J. Rojo, “Tuning PYTHIA 8.1: the Monash 2013 Tune”, *Eur. Phys. J. C* **74** (2014) 3024, doi:10.1140/epjc/s10052-014-3024-y, arXiv:1404.5630.
- [176] R. D. Ball et al., “Parton distributions with LHC data”, *Nucl. Phys. B* **867** (2013) 244, doi:10.1016/j.nuclphysb.2012.10.003, arXiv:1207.1303.
- [177] J. Alwall et al., “Comparative study of various algorithms for the merging of parton showers and matrix elements in hadronic collisions”, *Eur. Phys. J. C* **53** (2008) 473, doi:10.1140/epjc/s10052-007-0490-5, arXiv:0706.2569.
- [178] CMS Collaboration, S. Chatrchyan et al., “Pile-up scenario for Run-II”. <https://twiki.cern.ch/twiki/bin/view/CMS/PdmVPileUpDescription>, [https://twiki.cern.ch/twiki/bin/viewauth/CMS/PileupJSONFileforData#Pileup\\_JSON\\_Files\\_For\\_Run\\_II](https://twiki.cern.ch/twiki/bin/viewauth/CMS/PileupJSONFileforData#Pileup_JSON_Files_For_Run_II).

- [179] M. Cacciari, G. P. Salam, and G. Soyez, “FastJet User Manual”, *Eur. Phys. J. C* **72** (2012) 1896, doi:10.1140/epjc/s10052-012-1896-2, arXiv:1111.6097.
- [180] CMS Collaboration, S. Chatrchyan et al., “B-tag Recommendation”. <https://twiki.cern.ch/twiki/bin/viewauth/CMS/BtagRecommendation80X>.
- [181] CMS Collaboration, S. Chatrchyan et al., “B-tag Calibration”. <https://twiki.cern.ch/twiki/bin/view/CMS/BTagCalibration>.
- [182] S. D. Ellis, Z. Kunszt, and D. E. Soper, “Two jet production in hadron collisions at order  $\alpha_s^3$  in QCD”, *Phys.Rev.Lett.* **69** (1992) 1496–1499, doi:10.1103/PhysRevLett.69.1496.
- [183] W. Giele, E. N. Glover, and D. A. Kosower, “Higher order corrections to jet cross-sections in hadron colliders”, *Nucl.Phys.* **B403** (1993) 633–670, doi:10.1016/0550-3213(93)90365-V, arXiv:hep-ph/9302225.
- [184] CMS Collaboration, S. Chatrchyan et al., “Physics Analysis Oriented Event Display”. <https://twiki.cern.ch/twiki/bin/view/CMSPublic/WorkBookFireworks>. Accessed: 2015.
- [185] S. Ozturk et al., “Plans to Search for New Particles Decaying to Dijets in  $pp$  Collisions at  $\sqrt{s} = 10$  TeV”, (2009). CMS AN-2009/070.
- [186] CDF Collaboration, “Search for new particles decaying into dijets in proton-antiproton collisions at  $\sqrt{s} = 1.96$  TeV”, *Phys. Rev. D* **79** (2009) 112002, doi:10.1103/PhysRevD.79.112002, arXiv:0812.4036.
- [187] R. M. Harris and K. Kousouris, “Searches for Dijet Resonances at Hadron Colliders”, *Int. J. Mod. Phys.* **A26** (2011) 5005, doi:10.1142/S0217751X11054905, arXiv:1110.5302.
- [188] ATLAS Collaboration, “Search for production of resonant states in the photon-jet mass distribution using  $pp$  collisions at  $\sqrt{s} = 7$  TeV collected by the ATLAS detector”, *Phys. Rev. Lett.* **108** (2012) 211802, doi:10.1103/PhysRevLett.108.211802, arXiv:1112.3580.
- [189] CMS Collaboration, “Search for narrow resonances using the dijet mass spectrum in  $pp$  collisions at  $\sqrt{s} = 8$  TeV”, *Phys. Rev.* **D87** (2013) 114015, doi:10.1103/PhysRevD.87.114015, arXiv:1302.4794.

- [190] ATLAS Collaboration, “Search for new phenomena in photon+jet events collected in proton–proton collisions at  $\sqrt{s} = 8$  TeV with the ATLAS detector”, *Phys. Lett.* **B728** (2014) 562, doi:10.1016/j.physletb.2013.12.029, arXiv:1309.3230.
- [191] CMS Collaboration, “Search for excited quarks in the  $\gamma$ +jet final state in proton proton collisions at  $\sqrt{s} = 8$  TeV”, *Phys. Lett.* **B738** (2014) 274, doi:10.1016/j.physletb.2014.09.048, arXiv:1406.5171.
- [192] S. Baker and R. D. Cousins, “Clarification of the Use of Chi Square and Likelihood Functions in Fits to Histograms”, *Nucl. Instrum. Meth.* **221** (1984) 437–442, doi:10.1016/0167-5087(84)90016-4.
- [193] P. D. G. Collaboration, “Review of Particle Physics”, *Chin. Phys.* **C40** (2016) no. 10, 100001, doi:10.1088/1674-1137/40/10/100001.
- [194] CMS Collaboration, “Determination of Jet Energy Calibration and Transverse Momentum Resolution in CMS”, *JINST* **6** (2011) P11002, doi:10.1088/1748-0221/6/11/P11002, arXiv:1107.4277.
- [195] The ATLAS Collaboration, The CMS Collaboration, The LHC Higgs Combination Group Collaboration, “Procedure for the LHC Higgs boson search combination in Summer 2011”, Technical Report CMS-NOTE-2011-005. ATL-PHYS-PUB-2011-11, CERN, Geneva, (Aug, 2011). <https://cds.cern.ch/record/1379837>.
- [196] T. Junk, “Confidence level computation for combining searches with small statistics”, *Nucl. Instrum. Meth. A* **434** (1999) 435, doi:10.1016/S0168-9002(99)00498-2, arXiv:hep-ex/9902006.
- [197] A. L. Read, “Presentation of search results: The *CLs* technique”, *J. Phys. G* **28** (2002) 2693, doi:10.1088/0954-3899/28/10/313.
- [198] G. Cowan, K. Cranmer, E. Gross, and O. Vitells, “Asymptotic formulae for likelihood-based tests of new physics”, *Eur. Phys. J. C* **71** (2011) 1554, doi:10.1140/epjc/s10052-011-1554-0, arXiv:1007.1727. [Erratum: *Eur. Phys. J. C* **73** (2013) 2501, 10.1140/epjc/s10052-013-2501-z].
- [199] I. Asimov, “Isaac Asimov: The Complete Stories, Vol. 1”. Broadway Books, New York City, USA, 1990.